The Dissertation Committee for Yu Ding Certifies that this is the approved version of the following Dissertation:

Molecular Engineering and Structural Design of Electrochemically Active Organic and Organometallic Materials for Energy Storage Devices

Committee:

Guihua Yu, Supervisor

John B. Goodenough

Arumugam Manthiram

Guangbin Dong

Molecular Engineering and Structural Design of Electrochemically Active Organic and Organometallic Materials for Energy Storage Devices

by

Yu Ding

Dissertation

Presented to the Faculty of the Graduate School of

The University of Texas at Austin

in Partial Fulfillment

of the Requirements

for the Degree of

Doctor of Philosophy

The University of Texas at Austin

August 2018

Dedication

Dedicated to my parents Chenghua Ding & Ying Sun, and my sister Ying Ding

Acknowledgements

I would like to express the deepest appreciation to my supervisor Prof. Guihua Yu for his patient guidance. Being trained as an MSE graduate student, I have learned how to be a scientist from Prof. Yu's spirit of adventure in regard to science. When I felt ready to venture into research on my own and branch out into new research areas, Prof. Yu gave me the freedom to take adventures, at the same time continuing to provide valuable feedback, advice, and encouragement. I have been extremely lucky to have such a supportive supervisor throughout my doctoral study.

I would also like to express my gratitude to my committee members, Professor John B. Goodenough, Professor Arumugam Manthiram, and Professor Guangbin Dong, for kindly serving on my committee and providing valuable suggestions on my research. Especially I would love to express my sincere appreciation to Professor Goodenough for his consistent guides and inspirations throughout my PhD and his kind but rigorous revision on every detail of my dissertation.

My special thanks go to Professor John B. Goodenough (UT Austin), Professor Guangbin Dong (UT Austin and U Chicago), and Professor Yafei Li (Nanjing Normal University) for those fruitful collaborations on different projects.

I must express my sincere gratitude to my colleagues in Yu lab: Dr. Yu Zhao taught me many experimental skills in my first year and his son Eason is my best friend in kindergarten; Xuelin Guo, who is a bright first-year PhD student, also works very closely with me in my final year; Dr. Ye Shi, Dr. Lele Peng, Dr. Changkun Zhang, Dr. Fei Zhao, Dr. Jun Zhang, Dr. Pan Xiong, Dr. Yangen Zhou, Dr. Yumin Qian, Dr. Ping Wu, Dr. Yaqun Wang, Dr. Hongsen Li, Dr. Chade Lv, Dr. Chunshuang Yan, Dr. Dahong

Chen, Yue Zhu, Zhiwei Fang, Xingyi Zhou, Leyuan Zhang, Jiwoong Bae, Xiao Zhang, Youhong Guo, Panpan Li, Sangshan Peng, Chongbo Ma. I am so lucky to have so many terrific family members.

I also want to thank Dr. Richard Piner, Dr. Hugo Celio, and Dr. Abhimanyu Bhat for their kind help on experimental characterizations. Many thanks go to Dr. Leigang Xue, Dr. Linhan Lin, Dr. Jie Song, Dr. Gang Li, Dr. Guangmin Zhou, Dr. Long Qie, Dr. Zhiming Cui, Dr. Shaofei Wang, Dr. Yutao Li, Dr. Mingsong Wang and Dr. Longjun Li for sharing with me your insightful suggestions on research.

Last but not least, I want to thank my parents and my sister for their infinite love and support.

Molecular Engineering and Structural Design of Electrochemically Active Organic and Organometallic Materials for Energy Storage Devices

Yu Ding, PhD

The University of Texas at Austin, 2018

Supervisor: Guihua Yu

In modern society energy and environmental issues are regarded as two grand challenges for human beings. Researchers are trying to utilize sustainable energy more efficiently without squandering resources or polluting the environment. However, the widespread application of conventional energy storage devices is limited by the uncompetitive performance, as well as the high cost and environmental concerns associated with the use of metal-based inorganic redox species. In consideration of advantageous features such as potentially low cost, vast molecular diversity, and highly tailorable properties, organic and organometallic molecules emerge as promising alternative electroactive species. In this dissertation, two families of materials, metallocene-based organometallics and quinone-based organic compounds are investigated comprehensively to build the high-performance redox flow batteries (RFB) for large-scale energy storage.

Despite that metallocenes are also based on the redox reaction of metal centers, the cyclopentadienyl ring permits great flexibility to tune the electrochemical and

physical properties through molecular engineering. Thanks to the fast reaction kinetics, the ferrocene-based membrane-free liquid battery delivers a superior power capability. Moreover, the vast family of metallocenes provides an opportunity to build an all-metallocene-based RFB. The prototype device exploits ferrocene and cobaltocene as the redox-active cathode and anode, respectively. In light of the Hammett equation, the output voltage can be finely tuned by introduction of methyl groups on the ligand rings of cobaltocene.

We further investigated fundamental electrochemistry of quinones to enable heavy-metal-free, low-cost, environmental friendly energy storage devices. A bio-inspired, heavy-metal-free liquid battery has been built by directly using hydroquinone solution as catholyte and graphite as anode. The electrochemistry of hydroquinone is fundamentally studied in a broad pH range. By leveraging the knowledge of solubility enhancement techniques in pharmaceutical research, the solubility of hydroquinone in water is improved in the presence of urea as hydrotropic agent. Compared with arduous chemical functionalizations to improve the solubility of organic redox species, the hydrotropic solubilization method represents a sustainable and cost-effective approach to the design of grid-scale energy storage systems.

Last but not least, the application of quinone family for energy systems is extended to non-aqueous electrolytes. By rational screening of different solvents and functionalization of electrochemically active molecules, the redox potential, solubility and molecular mobility of the redox species can be tuned systematically. Theoretical modeling is conducted to examine Li-binding characteristics, electronic properties, and structural stabilities of organic redox species that govern electrochemical performance of those novel energy systems.

By integrating the function-oriented organic synthesis, detailed chemical characterizations, and advanced molecular dynamics simulations, we aim to provide a useful platform to design the next-generation of sustainable energy storage systems for grid-scale applications.

Table of Contents

List of Tables

List of Figures

Chapter 1: Introduction*

1.1 Need for Redox Flow Batteries (RFBs)

Securing a sustainable and environmentally friendly energy future is of utmost importance in the current development of human society. Among different types of energy resources, renewable sources such as solar, wind, hydroelectricity, wave, and tidal energy, provides a significant opportunity to alleviate the potential energy crisis stemming from the continuous increase in world energy consumption. According to World Bank data, fossil fuels, including natural gas, coal, and petroleum, still dominate the energy consumption and make up approximately 81% of the world's primary energy use.[1] Although fossil fuels can be regenerated through natural processes, their formation takes millions of years. Moreover, the carbon dioxide emissions from burning the remaining fossil fuels will worsen environmental issues, global warming in particular. Efforts to decrease the dependence of human society on fossil fuels eagerly await improved renewable energy harvesting and storage technologies. Given the intermittent nature of renewable sources, electrochemical energy storage devices such as batteries may play a critical role in effective round-the-clock delivery of their generated electricity.[2]

* Y. Zhao, Y. Ding, Y. Li, L. Peng, H. R. Byon, J. B. Goodenough, G. Yu, A chemistry and material perspective on lithium redox flow batteries towards high-density electrical energy storage, *Chem. Soc. Rev.*, 2015, 44, 7968.
Y. Ding, C. Zhang, L. Zhang, Y. Zhou and G. Yu, Molecular engineering of organic electroactive materials for redox flow batteries, *Chem. Soc. Rev.*, 2018, 47, 69.
Y. D. participated in the preparation of the manuscripts.

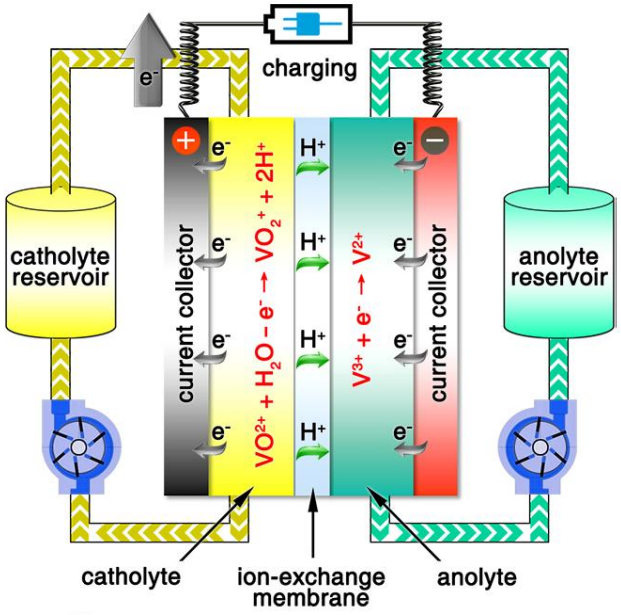

Figure 1.1: Schematic of a vanadium RFB. The active species are dissolved in a strong acid. During charge process, VO^{2+} is oxidized to VO_2^+ at the positive electrode and V^{3+} is reduced to V^{2+} at the negative electrode. The protons transport across the ion-exchange membrane to balance the charge.

RFBs, in which chemical energy is provided by electroactive materials dissolved in liquids and stored in outer tanks, show significant potential for applications in grid-scale energy storage.[3] The working mechanism of an RFB is akin to both a fuel cell and a battery. The typical structure of a RFB, vanadium-RFB for instance (Figure 1.1), has two chambers, a positive chamber and a negative chamber, separated by an ion-exchange membrane. A continuous circulation of electroactive materials is required to sustain the chemical reaction, like a fuel cell. Meanwhile, the reversible redox reaction enables charging and discharging within the same system, like a battery. Because of the special battery structure, RFBs feature a decoupled control on energy and power. The energy capacity is dictated by the amount of electrolyte stored, and the power is determined by the size of the current collectors and the number of cell stacks. More importantly, RFBs

can be almost instantly recharged by replacing the discharged electrolytes, while simultaneously recovering the exhausted electroactive materials separately, which provides beneficial flexibility for multiple energy storage applications. The first RFB-like cell was conceptualized in 1884, when Charles Renard developed a zinc-chlorine battery to power his airship "La France".[4] Research on this technology was revived in the early 1970s, and the first practical RFB was invented by Lawrence Thaller at NASA for solar photovoltaic energy storage.[3] While the investigation of RFBs has been sporadic for the past 40 years, the recent renaissance of renewable energy harvesting has prompted remarkable innovation in this field and given rise to numerous exciting advances, including tailored redox species, novel battery structures, and high-performance membranes. The majority of RFBs explored to date are still based on inorganic redox species, especially metal-based electroactive materials, and the redox reactions are primarily dependent on the change in valence state of metal centers. In some designs, precious-metal electrocatalysts are required to enhance the electrochemical kinetics. Moreover, similar to solid state batteries, the development of metal-based RFBs has encountered a bottleneck. The electrochemical performance is restricted by the intrinsic properties of inorganic redox species, making it hard to further improve energy density. As a result, the widespread implementation of conventional RFBs is hindered by the high cost, material scarcity, environmental concerns, and uncompetitive performance metrics. To overcome the challenges of metal-based redox species, there is an urgent need to find inexpensive and green electroactive alternatives for sustainable high performance RFBs.[5]

Recently, organic redox molecules have emerged as a promising class of electroactive materials for energy storage applications, including Li ion batteries, supercapacitors, and RFBs.[6,7] In contrast to metal-based redox species in which the redox reaction relies on the valence change of metal centers, the reaction of organic materials

are commonly governed by the charge state of carbon, oxygen, sulfur and nitrogen atoms. In addition to the merits of potentially low cost, scalability, efficient biodegradability, and minimal environmental footprint, organic molecules possess highly tailorable chemical and physical properties. Molecular engineering provides excellent opportunities for constructing sustainable and green energy-storage devices. Over the last few decades, tremendous progress has been made to address the limiting factors of organic molecules in solid state batteries via functional group modification. Furthermore, the working mechanism and design principle have also been systematically summarized in a number of review papers.[8] Meanwhile, the exploitation of organic molecules in RFBs has also gained increasing attention. In stark contrast to decreasing the solubility of organic electrode materials in solid state batteries, it is required to optimize the high solubility of organics in the electrolyte of RFBs. Up to now, achievements have been made in functionalizing organic molecules for RFB application, but a comprehensive summary about the rationale and underlying chemistry behind the molecular engineering method is absent.[9] In this dissertation, I provide background introduction, latest progress, my own projects in overcoming the limits, and future perspectives in this emerging research field. The concept of molecular engineering methods can be promoted as a general problem solving approach in energy storage systems, especially in RFBs. Systematic, function-oriented synthetic strategies are presented to show the highly tailorable properties of metallocenes and quinones. Although the redox reactions of metallocenes are based on the metal centers, they are included in this dissertation due to their highly tunable properties via molecular functionalization.

In spite of increasing attention, the research on organic-based RFBs is still at its early stage, and a great number of challenges remain to be addressed. We present the remaining issues and future research plan in the summary section. We hope this

dissertation will promote more interest in this interdisciplinary research field. Finally, we aim to provide general design principles and guidelines to build high-performance sustainable RFBs (Figure 1.2).

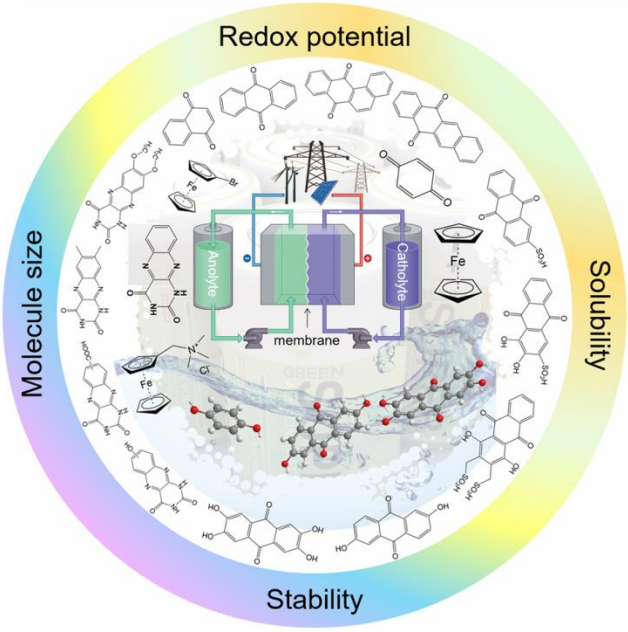

Figure 1.2: Molecular engineering of redox species for sustainable RFBs.

1.2 THE DEVELOPMENT OF AQUEOUS RFBS

The first modern RFB, also the first aqueous RFB, was invented by Lawrence Thaller at the Lewis Research Center in Cleveland.[3] After rational screening of redox species and systematic optimization of battery components, Thaller selected the iron-chromium system, in which Fe^{3+}/Fe^{2+} and Cr^{3+}/Cr^{2+} were dissolved in an acid medium as catholyte and anolyte, respectively. This device represents the most typical RFB type, in which both the cathode-active and anode-active materials are dissolved in water and separated by an ionic conductive membrane. Thaller also proposed several criteria regarding the system design, most of which are still valid today, including: (a) both the oxidized and reduced species should be soluble; (b) the solvent should remain inert during the working potential range; (c) the membrane should prevent crossover of redox species in both states of charge, and allow the diffusion of either positive or negative ions as charge carriers to maintain charge neutrality.

	Aqueous RFB	Non-aqueous RFB
Redox species	Metal ions	Metal-ligand complexes
Electrolyte	H_2SO_4 in H_2O	$TEABF_4$ in acetonitrile (ACN)
κ of electrolyte/(mS cm^{-1})	500-700	40-55
Potential window (V vs. SHE)	0-1.93	−2.6-3.5
Membrane	NAFION	Anion exchange membranes
Charge carrier of membrane	H^+	BF_4^-
σ of membrane/(mS cm^{-1})	50-200	0.1-20
Power density/(mW cm^{-2})	10-600	1-10

Table 1.1: Comparison between typical aqueous and non-aqueous RFBs based on metal ions and metal-ligand complexes.

Up to now, aqueous RFBs are the most appealing type of RFB because of their low cost, high safety, non-volatility, and facile processing. From Table 1.1, which compares typical aqueous and non-aqueous RFBs, it is obvious that the conductivity of an aqueous electrolyte is typically much higher than that of a non-aqueous electrolyte. The characteristics of electrolytes are mainly governed by the intrinsic properties of both the salts and the solvents. When comparing the basic physical properties of water and some conventional non-aqueous solvents, because of its high dielectric constant, water can dissolve conventional acids, bases, and salts as either charge carriers or redox-active materials. Equally important is its low viscosity, which can lower pumping costs and

increase ionic conductivity. The most widely used vanadium RFB commonly uses 3-4 M H_2SO_4 in water as electrolyte, which offers conductivity as high as 700 mS cm^{-1}.[10] While the battery is operating, hydronium ions diffuse back and forth to balance the total charge. Since the charge carriers are positive, Nafion (sulfonated tetrafluoroethylene based fluoropolymer-copolymer) is adopted as a proton conducting separator. Due to the high ionic conductivity of the Nafion (200 mS cm^{-1}) together with the high conductivity of aqueous electrolyte, aqueous RFBs can achieve power densities higher than 500 mW cm^{-2}.

Thus far, several types of aqueous RFBs have been commercially developed, but technical and economic challenges have prevented their world-wide implementation. Moreover, the electrochemical performance of an aqueous flow system is restricted by the intrinsic properties of water, such as the narrow potential window and limited operating temperature range. Especially when we consider organic and organometallic-based redox species, incompatibility between hydrophobic organic molecules typically requires logical molecular engineering to meet performance metrics. In this regard, non-aqueous solvents provide much more freedom for rational screening and selection given the diverse solvent alternatives.

1.3 THE DEVELOPMENT OF NON-AQUEOUS RFBS

Non-aqueous RFBs have the potential to achieve much higher energy density than aqueous ones because of their significantly wider potential windows, not to mention the extensive options for both cathode and anode-active materials.[11] The first non-aqueous RFB can be traced back to 1988, when Matsuda and co-workers utilized a ruthenium complex $[Ru(bpy)_3](BF_4)_2$ in ACN as an active material.[10] The proof-of-concept design demonstrated an open circuit voltage of 2.6 V obtained at a discharge current of 5 mA cm^{-2}. Since then, most reported non-aqueous RFBs have been anion-exchange systems with metal-ligand complexes as electroactive materials. Typical parameters of such a non-aqueous RFB are given in Table 1.1. Following the work by Matsuda, $TEABF_4$ salt in ACN is still a commonly used electrolyte with the conductivity between 40 and 55 mS cm^{-1}, which is one order of magnitude smaller than that of aqueous electrolytes. Moreover, anions usually function as charge carriers during the working process of non-aqueous RFBs, necessitating the use of anion exchange membranes as separators. In contrast to cation exchange membranes that rely on sulfonate groups anchored on tetrafluoroethylene backbones to conduct protons, anion exchange membranes are commonly based on quaternary ammonium groups and hydrocarbon polymer backbones, and they exhibit much smaller ionic conductivity. When comparing the electrolyte conductivity of aqueous and non-aqueous RFBs, it is noteworthy that the ionic conductivity of non-aqueous electrolytes is far less than aqueous electrolytes. Given the two factors mentioned above, the power densities of non-aqueous RFBs are eclipsed by those of aqueous RFBs, as indicated in Table 1.1. To address this concern, future attention can be geared towards developing advanced membranes and electrolytes to boost the ion transport. Meanwhile, a 3D porous current collector with high surface area is beneficial to promote the electrochemical kinetics.[12] Rational screening of organic

solvents should prioritize a wide operating temperature range and potential window to enable a high-voltage RFB applicable in harsh environments. Meanwhile, organic solvents with low viscosity are propitious to higher ionic conductivity of electrolytes as guided by Stokes' law. ACN is widely utilized as the solvent for non-aqueous RFBs owing to its even lower viscosity than water. Another important parameter in selecting organic solvents is relative permittivity, which determines both the solubility and dissociation of supporting salts. Generally, higher relative permittivity in organic solvents can enable high-concentration organic electrolytes with higher ionic conductivity. In light of the elevated output voltage of non-aqueous systems, such designs coupled with suitable separators are anticipated to reach power densities comparable to those of aqueous RFBs. In some novel RFBs with hybrid electrolytes, particularly those using a Li metal anode, solid state electrolyte membranes serve as separators, which effectively prevent the crossover of redox species and withstand the dendrites of alkaline metals. Though the ionic conductivity cannot compete with Nafion in aqueous electrolytes, further improvement of both the conductivity and stability of solid state electrolytes could advance this promising replacement for current polymer-based separators.

Non-aqueous RFBs have rarely been commercialized mainly due to the high cost of raw materials and complex packaging process.[13] However, the 3-factor increase in potential window indicates great promise for such emerging energy systems. When comparing the allowable chemical cost factor versus open circuit voltage of both aqueous and non-aqueous RFBs, 4-5 M electroactive materials in non-aqueous solvents can meet the cost requirements for energy storage and compete with 1-2 M aqueous electrolytes. The structural diversity and immense alterability of organic and organometallic redox species, together with an abundance of non-aqueous solvent alternatives with wide potential windows, provide a pathway for achieving such a research goal.

1.4 The Development of Novel Li-RFBs

Li-RFB is a newly-emerged battery that combines the advantage of a redox-flow battery and a Li–ion battery.[14] The structure of a Li-RFB (Figure 1.3) inherits the smart features of conventional redox-flow batteries: a soluble cathode-active redox couple dissolved in a proper solvent to form the catholyte and metallic Li as the anode or soluble anode-active redox couple dissolved in a proper solvent to form the anolyte. The catholyte and the anolyte can be stored in external reservoirs and circulated with the assistance of external circulating sub-system. Therefore, the energy capacity can be independently scaled up. The chemistry of a Li-RFB shifts from proton-mediated redox reaction to a Li^+-mediated one, which provides sufficiently high operating voltage that is comparable to the Li–ion batteries. The charge transport inside the battery is based on the transport of Li ions between anode and cathode, and certain Li-ion conducting membranes are adopted to prevent the crossover of redox couples between two electrodes.

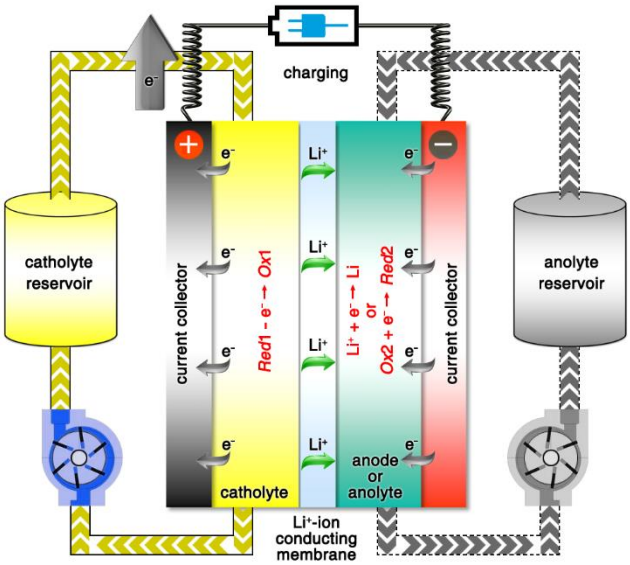

Figure 1.3: Structure and working principle of a Li-RFB.

In a typical charge process, the reduced form of one redox species (Red1) in the catholyte is oxidized to its oxidized form (Ox1) at the positive electrode, and Li^+ or the oxidized form of another redox species (Ox2) in the anolyte is reduced to metallic Li or its reduced form (Red2) at the negative electrode, respectively. Li^+ ions diffuse across the Li-ion conducting membrane to balance the charge. This process usually proceeds until the redox species are exhausted in the electrolyte. General electrochemical reactions during charge process at the electrodes are shown below:

Positive electrode: $C^{x+} - ye^- \rightarrow C^{(x+y)+}$

Negative electrode: $Li^+ + e- \rightarrow Li$

or $A^{m+} + ne^- \rightarrow A^{(m-n)+}$

Overall reaction: $C^{x+} + yLi^+ \rightarrow C^{(x+y)+} + yLi$

or $nC^{x+} + yA^{m+} \rightarrow nC^{(x+y)+} + yA^{(m-n)+}$

where $C^{(x+y)+}/C^{x+}$ and $A^{m+}/A^{(m-n)+}$ stand for the redox couple in the catholyte and the anolyte, respectively. The process is reversed on discharge.

Depending on the anode structure, Li-RFBs can be categorized into two types: full-flow Li-redox cell and semi-flow Li-redox cell. The former uses redox-active liquid or slurry as the catholyte and the anolyte. The latter, which dominates current Li-RFB research, uses a redox-active liquid or slurry as the catholyte and Li metal as the anode. Depending on the electrolyte used, Li-RFBs can be divided into two categories: one uses an aqueous/aprotic hybrid electrolyte configuration and the other uses an aprotic electrolyte configuration. The basic set-up of the prototype Li-RFB with aqueous/aprotic hybrid electrolyte is essentially similar to that of conventional RFBs (Figure 1.4). In the cathode or anode compartments, a porous conductive layer, usually made from graphitic materials, is applied as the diffusion layer and the current collector, and the catholyte or

anolyte in the external reservoir can be pumped into the flow frame and circled via an eternal circuit. The thickness of the flow frame is usually about 1−3 mm, and the electrolyte flows through the electrode is normally laminar. The Li-ion conducting glass ceramic or polymeric solid electrolyte can be used as separator to block the crossover between the catholyte and the anolyte. Particularly, metallic Li can be directly used as the anode taking advantage of its high energy density. In such a configuration, a buffer layer and conventional organic electrolyte are usually used to prevent corrosion of a solid electrolyte by metallic Li and to facilitate Li−ion transport between metallic Li and solid-electrolyte separator.

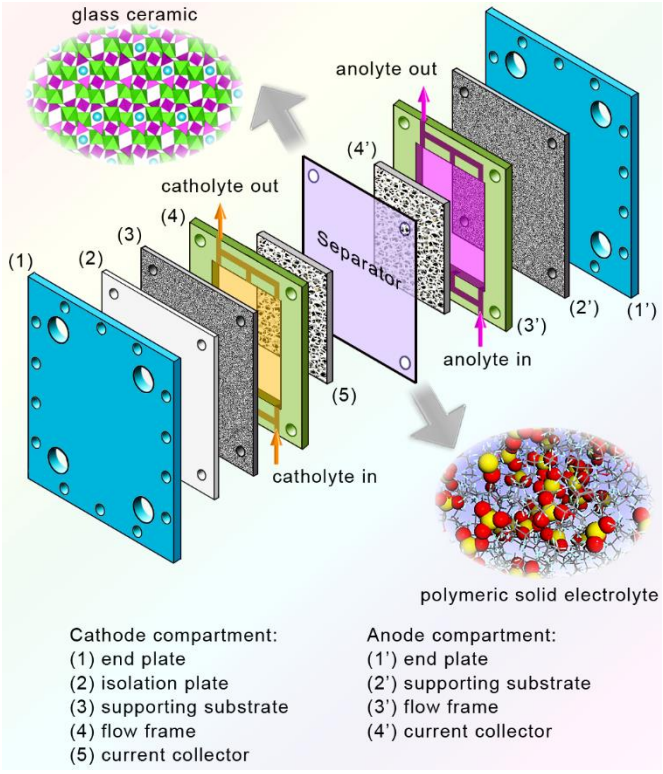

Figure 1.4: Schematic structure of a Li-RFB.

1.5 Principles of Molecular Engineering

A typical RFB is composed of two storage tanks filled with electrolytes that are pumped across a membrane held between two electrodes serving as current collectors. An ideal membrane allows fast transport of the charge carriers, but prevents crossover of redox species. The electrochemical performance of an RFB depends on several parameters and can be evaluated by the following benchmarks. Energy density is the most important performance metric for energy storage devices. The high energy density is expected as to store as much energy as possible in a given volume. In an RFB system, the energy density is dictated as below:

$$\text{Energy density} = nCFV/\mu_v$$

where n is the number of electrons transferred in the reaction, C is the lower concentration of two electrolytes, F is Faraday's constant, V is the voltage of the battery, and μ_v is the volume factor (μ_v = 1 + lower electrolyte concentration/higher electrolyte concentration). Thus, the energy density is mainly dependent on the number of electrons involved, solubility of redox species, and the potential difference between the cathode and anode-active materials. Consequently, when selecting redox couples for RFBs, the solubility should be as high as possible. This criterion is exactly the opposite in solid state batteries, in which the solubility of electrode materials should be minimized to avoid the performance degradation caused by electrode dissolution. The molecular weight of redox species should also be taken into consideration, since small molecules are more likely to achieve high gravimetric energy density. In addition to solubility, the redox potential of redox species is of equal importance. To achieve the highest possible output potential within the intrinsic range of the solvent, the anolyte and catholyte potentials should be near the extremes of the operating potential of the electrolyte.

An equally important metric for consideration is power density, which is the amount of power per unit area and can be determined using the following equation:

$$\text{Power density} = (I \times V)/S$$

where I is the discharge current, V is the output potential, and S is the surface area of membrane or electrode geometric area. It follows that the power density is governed by several parameters bundled together, including the electrolyte conductivity, ionic conductivity of the separator, diffusion coefficient and reaction kinetics of the redox species, cell potential, size of the current collector, battery structure et al. In terms of the electrochemistry of redox species, the diffusion coefficient and reaction rate constant should be high enough to sustain high power performance.

The coulombic efficiency (CE), also called current efficiency or faradaic efficiency, is another important parameter for evaluating battery performance. CE can be calculated using the same method for conventional solid state batteries, by determining the ratio between the charge output in the discharging process to the charge input in the charging process. Normally CE < 100% is attributed to either the crossover of redox species or the irreversibility of the redox reaction. Because high CE is indispensable in RFBs, cation or anion exchange membranes with high selectivity are commonly used to enable high efficiency despite their cost. In aqueous RFBs, Nafion is the most widely used separator, and it accounts for nearly 40% of the stack cost. In addition to the aforementioned performance metrics, it is also useful to analyze voltage efficiency (VE), which is the ratio between the discharging and charging voltages, energy efficiency (EE), which equals CE times VE, and cycling stability.

In conventional RFBs based on metal ions, it is difficult to tune the intrinsic properties of redox species, leaving modification of other battery components as the only means for improving electrochemical performance. Inspired by the advances in synthetic

chemistry, organic molecules emerge as promising alternatives with highly tailored properties. Solubility, redox potential, molecular size, and chemical reversibility can all be tuned by modification of the organic core component with particular functional groups to build a high-performance RFB. In the next section, a general principle is provided here regarding functionalization of organic and organometallic molecules, including the relationship between functional groups and solubilization effects, redox potentials, and the size of redox species.

1.5.1 Solubility

As introduced above, the energy density of an RFB is proportional to the concentration of redox species. The solubility of electroactive material is of vital interest in the scientific community of RFBs. Nevertheless, typical organic molecules, especially those with large molecular structures, maintain low solubility in water. Therefore, rational molecular engineering method is usually required to tailor the structures of organic molecules for applications in RFBs. The solubility of a substance fundamentally depends on both the chemical and physical properties of solute and solvents. Theoretically speaking, the solubility of a certain substance is governed by the balance of intermolecular interaction between the solute and solvent, and can be roughly estimated by the entropy change in the solvation process.[15] Generally the solute molecules are held together by certain intermolecular forces, such as dipole-dipole, induced dipole-induced dipole, and ion-ion interaction. In the dissolution process, the interactive forces between solute-solvent molecules should be large enough to overcome the adhesive forces between solute-solute molecules. Thus strong solute-solvent attractions give rise to greater solubility than weak solute-solvent attractions.

For example, in a typical dissolution process of ionic compounds, which contain periodic arrangements of charged ions bonded together via electrostatic force, the solvation energies of ions commonly need to be larger than the lattice energy.[16] Therefore, the lattice energy of an ionic compound gives a rough indication of the solubility of the substance as it reflects the energy required to separate positive and negative ions. Meanwhile it is preferred for the solvent to have large relative permittivity, which can decrease the electrostatic force between positive and negative ions.[17] When comparing the relative permittivity of various kinds of solvents, including water, alcohols, ethers, nitriles and so on, it is interesting to find that water possesses one of the highest relative permittivities, allowing salts to dissolve with ease. To achieve dissolution in organic solvents with low relative permittivity, the salts should possess large ion size and low lattice energies, for example tetraethylammonium tetrafluoroborate.

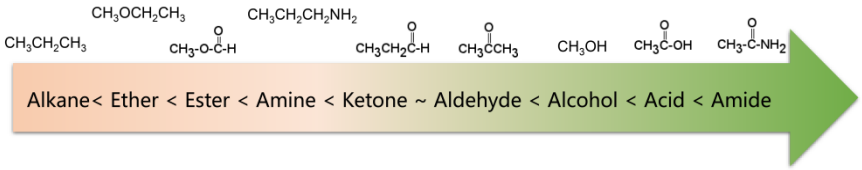

Figure 1.5: Polarity ranking of typical organic functional groups.

Another general rule for predicting solubility is “like dissolves like”, which means that a solute tends to dissolve easily in solvents with a similar chemical structure.[18] Specifically, polar solvents can dissolve ionic and other polar substances, whereas non-polar solvents tend to dissolve non-polar solutes. This principle can also predict the solubility of organic molecules in a certain solvent. Non-polar organic molecules are generally insoluble in water, but are highly soluble in non-polar solvents. The sequence of polarity of common organic functional groups is shown in Figure 1.5. To increase the solubility of non-polar solutes in polar solvents, certain polar (and therefore hydrophilic)

functional groups can be attached to the molecular chain, thus increasing the interaction between solutes and solvents. Likewise, if we want to improve the solubility of polar molecules in non-polar organic solvents, the solute molecules can be functionalized with non-polar groups. The relative permittivity of different solvents provides a rough measure of a solvent's polarity. In general, a solvent is regarded as nonpolar when it has a relative permittivity less than 15. Furthermore, the dipole moment of a solvent can be used to assess the solvent polarity as well. Many solvents with high relative permittivity also maintain high dipole moments. Nevertheless, the dipole moment sometimes underestimates the polarity of solvents with small molecules because it depends on the distance between the positive and negative charge centers in the molecule, and that's why the dipole moment of water is lower than expected.

In addition to the empirical principles introduced above, thermodynamic models provide a potentially efficient and cost-effective method for predicting a compound's solubility. Based on the Van't Hoff equation and general solubility theory, a number of models have been constructed relating solubility with changes in Gibbs free energy, enthalpy, and entropy accompanying the solvation process.[19] Compared with time-consuming and laborious experimental methods, the ability to accurately predict solubility represents a promising approach to rational design and screening of organic electroactive materials for RFBs. Notwithstanding recent progress, research is still needed to develop a reliable and fast model, capable of offering high levels of accuracy at a reasonable cost. Emerging scientific understanding with physical and chemical insight, combined with optimization of the parameters based on larger sets of experimental values may lead to breakthroughs in the computational modeling of organic electroactive materials.[20]

1.5.2 Redox Potential

Energy density is dictated by the concentration of redox species and the cell voltage. Therefore one would seek cathode and anode-active materials with the greatest potential difference within the potential window of the electrolyte. In this regard, organic and organometallic-based molecules provide high flexibility to tune the redox potentials. Firstly, the redox potential is affected by both the chemical and physical conditions of the electrolyte. If protons are involved in the redox reaction of the organic electroactive materials, the redox potential will have a linear relationship with pH, as mapped out in the Pourbaix diagram.[21] The slope of potential shift can be calculated from Nernst equation, and the general trend is that increasing pH value will decrease the redox potential for a given proton-involved reaction.

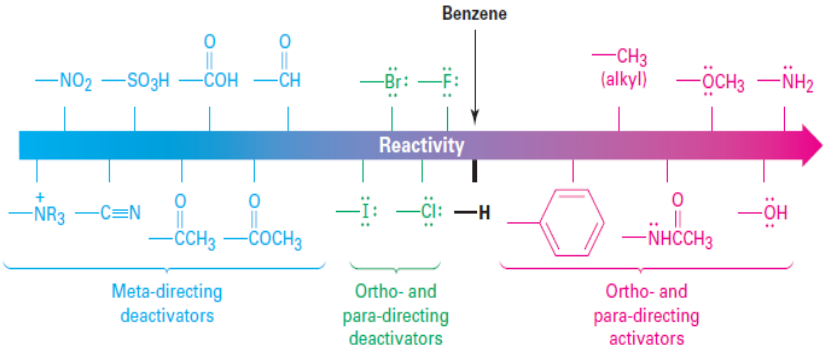

Figure 1.6: Electron donating and withdrawing groups.

Additionally, the voltage of organics can be modified by means of molecular engineering, as has been done in Li ion batteries based on organic electroactive materials.[22] The general principle behind the battery chemistry is that functionalization of electron-withdrawing groups, such as nitro and sulfonic acid, can increase the electron affinity of molecules, thus leading to increased redox potentials. In contrast, electron-donating groups, such as amino and hydroxyl, can release electrons to the redox centers

and thus result in decreased redox potentials. Figure 1.6 shows the substituent effects in sequence from deactivating to activating groups. In terms of redox potential, the electron-donating groups (activating groups) are applicable for the redox species in the anode side, while electron-withdrawing groups (deactivating groups) improve the potentials of molecules in the cathode side. The effect of functional groups has been verified by both experimental and computational results.[23] In the calculated HOMO-LUMO energy levels, it is clear that frontier orbitals shift in the same direction according to electron-donating or electron-withdrawing groups, corresponding precisely with the potential tuning.[24] Meanwhile, the redox potential derived from Gibbs free energy change also shows the same trend in accordance with the substituted groups.[25]

Furthermore, the effect of functional groups on the redox potentials of some organic redox species can be quantified by the Hammett substituent constant, which indicates the dependence of substituent effects in aromatic molecules upon rates of reaction and equilibrium constants.[26] A basic Hammett equation is shown below:

$$\log(K/K_0) = \sigma\rho$$

where K and K_0 are the equilibrium constants for the reaction of the organic species with or without functionalization, σ is the substituent constant that depends on the specific functional group, and ρ is the reaction constant.[27] It follows that the Gibbs free energy change, which also relates to the redox potential, is proportional to the substituent constant for a certain type of reaction. Table 1.2 summarizes the σ values for the oxidation reaction of phenol, and a rough but significant correlation was derived between Hammett's constant and potentials.[28]

$$E = 1.225 + 0.45\sigma$$

It is obvious that electron-donating groups normally possess negative Hammett's constant, which will lower the redox potential. But for electron-withdrawing groups, the

Hammett's constant is positive, meaning the potential will be increased due to the function of substituents. The correlation between reaction potential and changes in structure of molecules is of special interest to rational design of organic-based redox species for energy applications. It also enables the possibility to predict the electrochemical activities of tailored organic compounds in advance.

Substance	*p*-NH_2	*p*-OCH_3	*p*-CH_3	*m*-CH_3	*m*-OH
σ	-0.66	-0.13	-0.076	-0.007	-0.002
Substance	H	*m*-OCH_3	*m*-OC_2H_5	*p*-SO_3^-	*m*-CHO
σ	0	0.115	0.15	0.38	0.381
Substance	3,4-$(CH_3)_2$	3,5-$(CH_3)_2$	3-OH,5-CH_3	*p*-Cl	4-Cl,3-CH_3
σ	-0.083	-0.014	-0.009	0.227	0.22

Table 1.2: The Hammett substituent constant of phenol.

1.5.3 Molecular Size

Another important criterion for quantifying the performance of an RFB is CE, which describes the efficiency of electron transfer within an electrochemical system. Unless ceramic-based separators are used to isolate completely the catholyte and anolyte, crossover of redox species is an inevitable issue.[29] When electrochemically active species diffuse through separators, efficiency is not only lost on the charge-discharge cycle, but the cycling stability degrades due to the irreversible crossover process. A separator with high molecular selectivity is essential to alleviate the crossover issue of electrochemically active molecules. The selectivity of a membrane is commonly due to three effects, including physical blocking, electrostatic exclusion, and Donnan exclusion, which permit many engineered processes to achieve better redox species isolation. The most widely

used separator for RFBs is Nafion, which is a sulfonated tetrafluoroethylene based copolymer.[30] According to the cluster-network model, Nafion consists of uniformly distributed sulfonate ion clusters with a diameter of 4 nm in the rigid fluorocarbon framework. Meanwhile, narrower channels of 1 nm long interconnect all the clusters continuously within the fluorocarbon matrix. Therefore, Nafion plays a critical role in regulating the operation of RFBs. However, the specialized structure of Nafion requires a costly manufacturing process, which hinders its wider industrial applications.

The dimensions of common molecules range from a few angstroms to hundreds of angstroms. Thus, conventional polypropylene or polyethylene-based separators for Li ion batteries, with pores that are around 50 nanometers wide, are not suitable for RFB applications. Another promising type of separator is a dialysis membrane, which is only 5% to 10% of the cost of Nafion. Typically, the pore size ranges from ~1nm to 10 nm, and the separation effect is based on exclusion of molecules with large molecular masses. Therefore, the ion selectivity of separators can be enabled by size tuning of organic redox species, which should maintain molecular masses larger than the molecular-weight cutoffs of the membranes. Meanwhile, the separator must allow fast ion transport to ensure comparable power density.

To achieve an efficient size-exclusion effect, redox active monomers, oligomers, and polymers maintaining very wide size ranges can work as soluble nanoscopic energy storing units.[31] As shown in Figure 1.7, the tailorable size of organic-based redox species can be realized by anchoring redox active organic units into polymer backbones with different sizes. Especially for macromolecule-based species, the main chains or backbones can undergo graft co-polymerization, and the pendant chains can be tailored to meet the required molecular size and electrochemical activity. Furthermore, the redox-active organic moieties can be functionalized on polymer colloids to make cross-linked

polymer spheres with uniform diameter range and reversible redox activity in the form of flowable dispersions.[32] These methods demonstrate the diverse opportunities for tuning the sizes of organic species. It is noted that tethering redox active moieties to the polymer backbones may lead to decreased solubility of electroactive materials. Therefore, certain substituents with strong interactions with solvents are commonly functionalized to the polymer backbones as well to achieve reasonable concentration of redox-active unit.

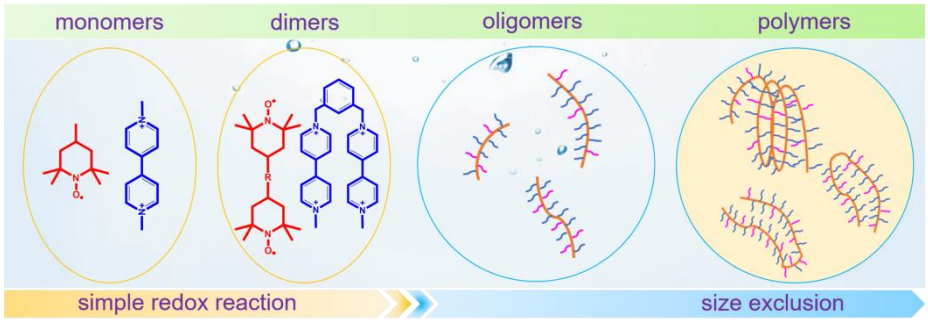

Figure 1.7: The tailored size of organic-based redox species by integrating redox active organic moieties into polymer backbones with different sizes.

In rationally designing organic electroactive materials to matching cost-effective size-exclusion membranes, size must be varied without reducing electrochemical activities of the redox moieties. Additionally, the organic molecule should remain highly soluble to meet energy density requirements. Lastly, the viscosity, rheological, and transport properties of the electrolytes should all be taken into consideration when implementing cost-effective flow systems based on inexpensive nanoporous commercial separators and size-tunable electroactive molecules.

So far the general principle to design organic and organometallic electroactive molecules following fundamental laws of physics and chemistry of RFBs has been summarized. In this dissertation, molecular engineering on two classes of electroactive

materials, metallocenes and quinones, will be introduced in detail in the following sections.

Chapter 2: General Experimental Procedures

2.1 Materials Synthesis

The detailed material synthesis procedures are provided in each individual chapter.

2.2 Materials Characterizations

The general physical and chemical characterization methods are based on the following techniques. The specific characterization procedures will be described in each individual chapter in detail.

2.2.1 X-ray Diffraction (XRD)

XRD experiments were conducted on a Rigaku Miniflex diffractometer with CuKα radiation.

2.2.2 Scanning Eelectron Microscopy (SEM) and Energy Dispersive X-ray Spectroscopy (EDS)

Morphologies and microstructures of the as-prepared samples were characterized using a SEM (Hitachi s-5500) equipped with a scanning transmission electron microscope (STEM). EDS elemental mappings were measured using the energy dispersive spectrometer.

2.2.3 Raman Spectroscopy

Raman spectrum of the prepared electrolytes were obtained using a Micro-Raman Spectrometer (Witec, Alpha 300) under 488 nm.

2.2.4 Ultraviolet–visible (UV-vis) Spectroscopy

The UV-vis spectra of samples were recorded using a UV-vis spectrometer (Evolution 300, Thermo Scientific) from 200 to 400 nm.

2.2.5 Fourier transform infrared (FTIR) Spectroscopy

The FTIR spectra were obtained using a Nicolet iS5 FT-IR spectrometer in the spectral area 400–4,000 cm^{-1}.

2.2.6 Nuclear magnetic resonance (NMR) Spectroscopy

^{1}H and ^{13}C NMR measurements were carried out with a Varian Gemini at 400 MHz. In NMR test, either D_2O or dichloromethane-d_2 were adopted as the solvent depending on the solubility of as-prepared samples.

2.3 Electrochemical Characterizations

Most of the electrochemical tests were performed on a BioLogic VMP3 potentiostat system, including the electrochemical impedance spectroscopy (EIS), cyclic voltammetry (CV), galvanostatic charge-discharge test. The rotating disk electrode (RDE) measurements were conducted on BioLogic RRDE-3A RDE and the data were recorded using a BioLogic VMP3 potentiostat system.

2.4 Computational Modeling

The density functional theory (DFT) modeling, including geometry optimizations, frequency analyses, and electronic structure computations, were performed at the B3LYP level of theory with the 6-31+G(d,p) basis set as implemented in the Gaussian 09 package. All molecular dynamics (MD) simulations were performed using the AMBER 10 suite of programs. Specifically, water was described with the SPC/E model. The

parameters of the force fields for urea were developed by Duffy et al. The AMBER99 force field force field was used to calculate van der Waals and electrostatic of organic molecules. The charge distributions on all atoms in organic molecules were obtained using the RESP-fit method based on B3LYP/cc-pVTZ DFT calculations.

Chapter 3: Molecular Engineering of Metallocenes for Non-aqueous RFBs

3.1 INTRODUCTION

As a typical type of organometallic-based redox species, metallocenes represent an important class of electroactive materials for both aqueous and non-aqueous RFBs. A metallocene is a compound consisting of two cyclopentadienyl (Cp) ligands bound to a metal center in the oxidation state of II, and the Cp rings in metallocenes provide more flexibility to tune their physical and chemical properties via rational synthetic procedures.[33] The intrinsic coordination and chemical reactivity of metallocenes are mainly regulated by the d-orbitals in the metal center and p-orbitals of the Cp rings.[34] Different electronic structures and valence electrons along with the variation of metal-carbon bonds contribute to distinct properties. The sandwich structure of metallocene is very robust with a variety of metal centers with the number of d electrons ranging from 14 to 20. The redox reactions of metallocenes are accompanied by a change in valence state of the metal centers.

Generally speaking, the electrochemical characteristics of metallocenes are dictated by the metallic coordination center and the effect of ligands. In conventional metal-ligand complexes, the complexing agents bind to the metal centers via lone pairs of electrons residing on the main group atoms of the agents. The electron-transfer processes can be either inner sphere electron transfer or outer sphere electron transfer depending on the effects between metal centers and ligands. During an inner sphere electron transfer reaction, two coordination centers are bridged by a ligand with two lone electron pairs, and electrons are transferred via the bridging ligand. Any other electron transfer processes aside from inner sphere electron can be assumed to be outer sphere. Because of the strong interaction between metal centers bridged by ligands, inner sphere electron

transfer is usually enthalpically more favorable. Nevertheless, it is entropically less favorable given the more ordered structure in inner sphere electron transfer than outer sphere electron transfer.

The tailorable properties of metallocenes promise better electrochemical performance of RFBs. For conventional metal-coordinated complexes, the transition metal usually acts as the charge transfer center, while the potential, solubility, kinetic rates, and stability can be tuned with different ligands. In complexes with redox-active ligands, charges can also be stored in complexing agents in addition to the central metals as redox moities. As for metallocene-based redox species, they share many characteristics of organic materials and undergo reactions similar to aromatic compounds, enabling the preparation of a variety of substituted derivatives. Therefore, a design principle for tailoring the properties of organic redox species is also applicable to metallocene-based electroactive molecules. On the other hand, the intrinsic properties of metallocenes mainly rely on the metal centers, and tailored properties of metallocenes can also be achieved by rational screening of the redox-active metal centers.

3.2 SUSTAINABLE ELECTRICAL ENERGY STORAGE THROUGH FERROCENE/FERROCENIUM REACTION IN APROTIC ELECTROLYTE*

3.2.1 Introduction

The rapidly expanding deployment of renewable energy sources, which supply electric power from wind and solar energy to a grid servicing a variable and increasing energy demand, requires the development of distributed electrical energy storage that may be either portable or stationary.[35] Rechargeable batteries offer such an electrical-energy storage, but all of the targets of cost, safety, service life, and energy and power density in a single existing rechargeable battery have yet to be met. Recently, rechargeable batteries with a solid oxide Li ion electrolyte separating an aprotic anolyte and an aqueous flow-through catholyte have been explored.[36] These batteries would offer a water soluble redox molecule and a metallic lithium anode, but a suitable Li ion electrolyte solid separator has yet to be developed. This cell configuration is potentially advantageous owing to the low cost of aqueous electrolytes and the extremely high capacity of a lithium anode. However, to avoid water decomposition, the H_2/O_2 evolution potential limits the cathode voltage. More importantly, the solid Li ion–electrolyte separator must be sufficiently robust mechanically to be fabricated as a thin, large-area membrane and have chemical stability in a corrosive aqueous catholyte to prevent the lithium anode from crossing into contact with the aqueous catholyte.

Alternatively, semipermeable, mechanically robust and flexible separators have been developed to block dendrites from an alkali-metal anode; they allow a flow-through catholyte containing an aprotic liquid with a large voltage window, e.g. formamide and

---

* Y. Zhao,[#] Y. Ding,[#] J. Song, G. Li, G. Dong, J. B. Goodenough, G. Yu, Sustainable electrical energy storage through the ferrocene/ferrocenium redox reaction in aprotic electrolyte, *Angew. Chem. Int. Ed.*, 2014, 53, 11036.
Y. Z and Y. D. contributed equally. Y. D. carried out most experimental work and co-wrote the manuscript.

amides, provided the redox molecule of the catholyte is soluble in the liquid electrolyte and is blocked from crossing the membrane into the anode.[37] A liquid flow-through cathode offers a fundamentally different, higher capacity and rate capability than a solid insertion-compound cathode, and use of an aprotic liquid electrolyte permits a higher voltage than is possible with a conventional aqueous flow-through battery. Herein, the use of inexpensive ferrocene dissolved in dimethylformamide is explored as the liquid cathode of a 3.6 V Li–ion cell with a solid Li ion–electrolyte separator. The liquid cathode exhibits high-rate discharging capability with high energy efficiency and stable discharge potential which are comparable to those of Li–ion batteries and superior to the conventional RFBs.

3.2.2 Experimental

The cell assembly process was carried out in a glove box. In brief, the Ti foil precasted with an acetylene black/PVDF thin layer (as current collector for the cathode) and the battery module was constructed with two quartz shells with a LATP membrane sandwiched in between, and was sealed together with Surlyn® resin. Afterwards, The dimethylformamide (DMF) solution containing 0.1 M $FeCp_2$ and 1 M $LiPF_6$ was injected into the compartment between the Ti foil and the membrane. After injection of the organic electrolyte into the other compartment, the quartz shell was sealed hermetically with the anode (composed of a piece of Li sheet pressed onto Cu foil). The DMF solution containing 0.1 M $FeCp_2$ was first dried with activated molecular sieves for two days and then $LiPF_6$ was added before use. A CV test was carried out in the potential range of 2.8−4.15 V vs. Li^+/Li with a DMF (or ethylene carbonate/diethyl carbonate (EC/DEC), tetrahydrofuran (THF) and dimethylacetamide (DMA)) solution containing 0.1 M $FeCp_2$ and 1 M $LiPF_6$. RDE measurements were carried out with a DMF solution containing 8 ×

10^{-4} M $FeCp_2$/$FeCp_2PF_6$ and 1M $LiPF_6$. Galvanostatic charge/discharge tests were carried out in the potential range of 2–4.15 V vs. Li^+/Li with a DMF solution containing 0.1 M $FeCp_2$ and 1M $LiPF_6$. EIS tests were performed on a fresh cell and the cell after cycling in the frequency range of 10^6–10^{-2} Hz. Chemical shifts of ^{1}H NMR are reported in parts per million (ppm, δ), and are referenced to residual solvent (C_6D_6, δ = 7.16 ppm (^{1}H)). DMF was distilled freshly over CaH_2 and freeze-pump-thawed before NMR tests.

Cyclic voltammetry, galvanostatic charge/discharge, EIS and polarization tests were performed on BioLogic VMP3 potentiostat equipped with impedance modules. RDE measurement was carried out on BioLogic RRDE-3A rotating ring disk electrode. XRD measurement was performed on a Philips APD 3520 X-ray diffractometer with Cu Kα radiation in steps of 0.02º with a step time of 4 s over the 2θ range. ^{1}H NMR spectra were recorded with a Varian Gemini (at 400 MHz).

3.2.3 Results and Discussion

In $FeCp_2$, two cyclopentadienyl ligand, C_5H_5, lie on top of each other with the Fe atom sandwiched in the middle. The π–orbitals of C_5H_5 rings and the Fe d-orbitals are responsible for coordination and chemical reactivity. As shown in Figure 3.1a, in the ground state, the frontier orbital of ferrocene is generally accepted as being $(e_{2g})^4(a_{1g})^2$, while for ferrocenium the orbital structure is generally accepted as being $(e_{2g})^4(a_{1g})^1$.[38] The activation energy required for the orbital electronic structure conversion is as low as ~10 kJ mol^{-1} in most organic solvents with a rate constant that is much greater than that of other redox couples used in conventional redox-flow batteries. Besides, good thermal stability, high solubility in most organic solvents, and a redox potential of 3.6 V vs. Li^+/Li make ferrocene an attractive material for the construction of a liquid cathode Li–ion battery.

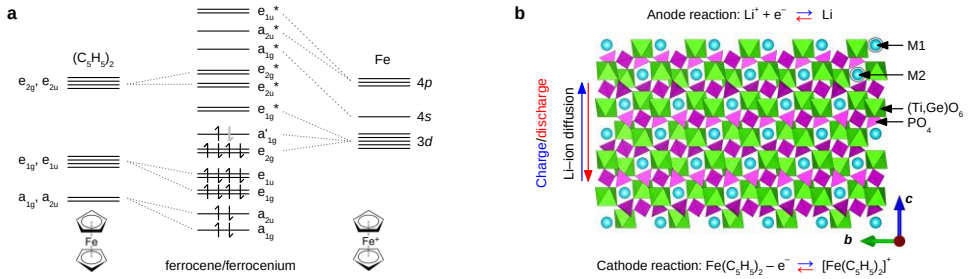

Figure 3.1: (a) Schematic of the frontier orbital electronic structure of ferrocene/ferrocenium. b) Working principle of the cell. A NASICON-type LATP membrane is used as separator which only allows Li–ions to pass through.

The working principle of such a battery is based on the reversible redox reaction between ferrocene and ferrocenium (Figure 3.1b). Upon charging, Li–ions move from the cathode to the anode through a NASICON-type $Li_{1+x+3z}Al_x(Ti,Ge)_{2-x}Si_{3z}P_{3-z}O_{12}$ (LATP) membrane in which the Li–ion diffuses via a vacancy-diffusion mechanism while electrons move from the cathode to the anode through the external circuit.[39] During charging, ferrocene is oxidized into ferrocenium in the cathode while the Li–ion is reduced into Li in the anode. Correspondingly, discharging is a reverse process relative to charging. The cell structure design is flexible following the basic rule that the cathode and anode be isolated by a Li–ion conducting ceramic membrane. Combining the concept and advantages of Li–ion batteries and RFBs, the cell can be designed with a flow-through cathode and a replaceable anode, both of which can be independently scalable. The benefit from such a configuration relies in the reduced size of individual cells to further lower the cost of the whole battery pack.

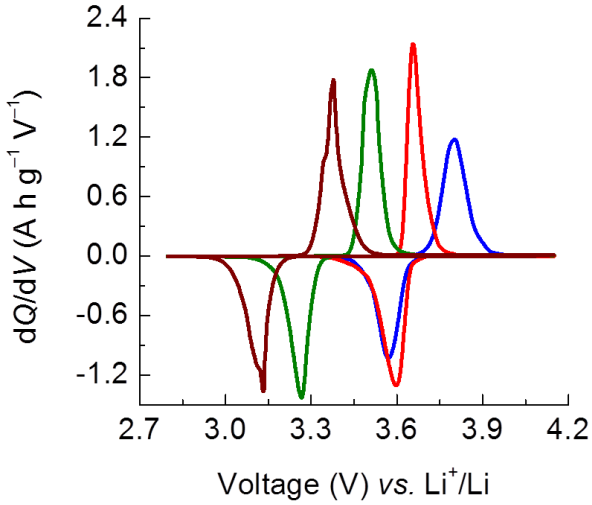

Figure 3.2: Solvent-dependent redox potential of ferrocene/ferrocenium in DMA, DMF, THF and EC/DEC solvents containing 1M $LiPF_6$ with current rate of 0.2 C.

The solvent might interact with either $FeCp_2$ or $FeCp_2^+$, leading to a significant solvent dependence of the redox reaction. Therefore, the redox behavior of $FeCp_2/FeCp_2^+$ in some representative inexpensive solvents such as DMF, DMA and THF were tested. The commercial organic electrolyte for Li−ion batteries, EC/DEC, was also tested as reference. The dQ/dV plots (Figure 3.2) of 0.1 M ferrocene in these solvents with the presence of 1M $LiPF_6$ exhibit quite different redox behavior at the same current density: DMA showed the highest redox potential followed by DMF and THF with EC/DEC being the lowest. However, the reversible capacity of ferrocene achieved in DMA was the smallest among the solvents tested. The redox potential depends on the interactions between ferrocene/ferrocenium and solvent molecules, via possible interactions between the hydrogen-bonding acid and base moieties of the solvent and the members of the ferrocene/ferrocenium couple.[40] It's found in our studies that DMF was the most suitable for ferrocene/ferrocenium redox reaction considering a smaller over potential (~70 mV) and higher reduction potential (~3.6 V vs. Li^+/Li) of ferrocenium. Moreover the cyclic

voltammetry (CV) with various sweeping rates (Figure 3.3) confirmed that the redox reaction of ferrocene/ferrocenium was reversible as the cathodic and anodic peaks were symmetric, and this redox reaction was the sole reaction taking place in DMF, suggesting the stability of both ferrocene/ferrocenium redox reaction and DMF as solvent in the measured potential range. Increasing the sweeping rate led to a linear response of peak current density and square root of sweeping rate, indicating the redox electrochemical process in the system was controlled by diffusion.

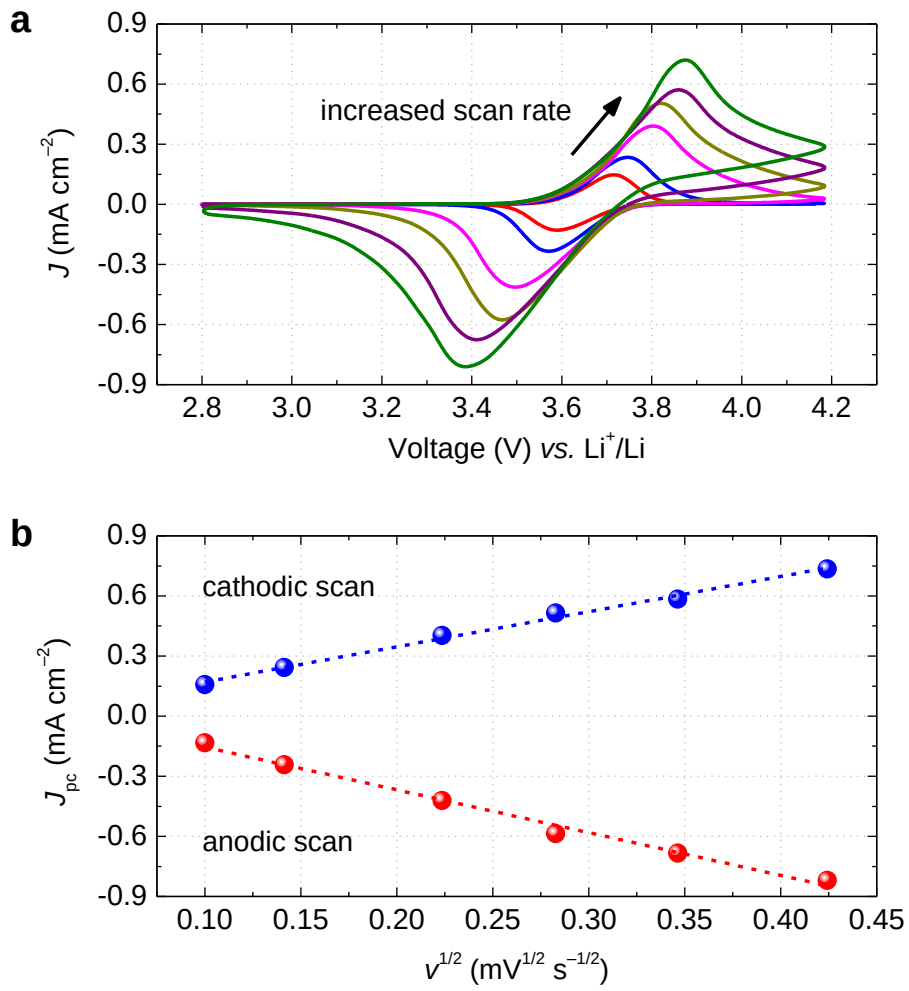

Figure 3.3: (a) CV profiles at various scan rate of 0.01, 0.02, 0.05, 0.08, 0.12 and 0.18 mV s^{-1} using 1M $LiPF_6$ in DMF as electrolyte. (b) Plot of peak current density (J_{pc}) as function of the square root of sweeping rates ($v^{1/2}$). The linear response indicates the redox reaction in the cell is diffusion-controlled.

The Li-ion solid electrolyte membrane, often the bottleneck of mass transfer, did not restrain a high power output of the cell. Polarization-curve analysis showed a maximum power output of 155 W kg^{-1} with a corresponding discharge potential of ~2.4 V could be achieved at room temperature based on the total weight of the ferrocene solution (Figure 3.4a). The cell could work briefly with the maximum power output in

order to avoid possible Ti(IV) reduction in the Li–ion conducting membrane when the voltage was below 2.8 V. The cell was able to deliver a rated power output of 120 W kg^{-1} with current density of 1150 mA g^{-1} (equals to C-rate of ~8). This power density is comparable to/exceeding that of the current battery technologies.[41] Increasing the conductivity of the Li–ion conducting membrane would significantly improve the power performance. The capacity retention at different current densities (Figure 3.4b) revealed that the cell reached a reversible capacity of 134 mA h g^{-1} with a discharge potential of ca. 3.6 V at a current density of 0.2 C with 94% of the theoretical capacity of ferrocene. Ohmic polarization resulted from the resistance of the Li–ion conducting membrane, and concentration polarization resulted from limited Li–ion transport in the solid electrolyte; ferrocenium diluent in the electrolyte became more obvious as the current density increased. Nevertheless, reversible capacities of 130, 110 and 90 mA h g^{-1} were delivered at higher current densities of 0.5, 1 and 1.5 C, respectively. It could be expected that the rate capability could be further enhanced with the development of superior Li–ion conductors, which would benefit in promoting mass transfer between the anode and cathode.[42]

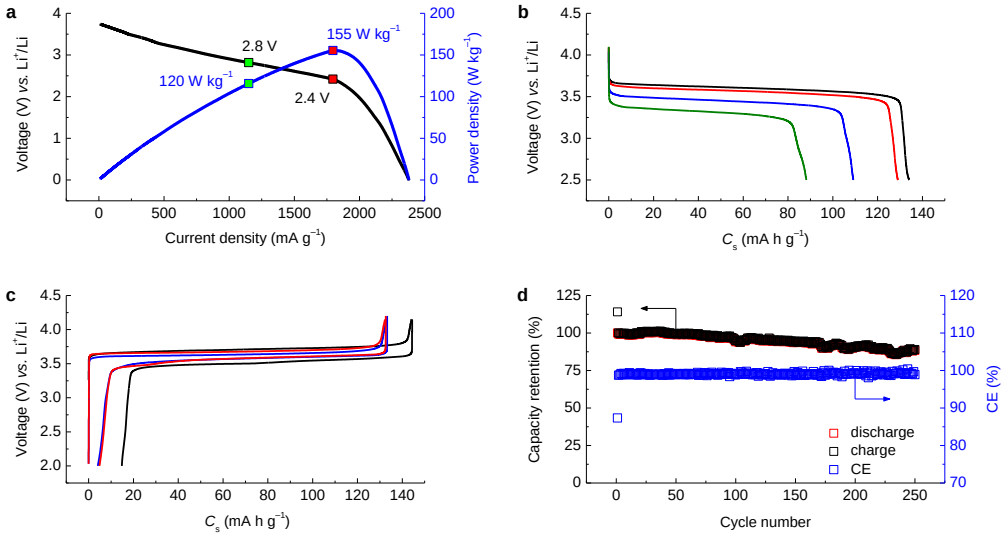

Figure 3.4: (a) Polarization curve and corresponding power density at room temperature. (b) Room temperature cell discharge behaviour at various C-rate of 0.2, 0.5, 1, and 1.5. The cell is fully charged to 4.15 V (vs. Li^+/Li) with a fixed C-rate of 0.2 prior to rate capability test. (c) Representative charge/discharge profiles of the 1st, 2nd and 50th cycles. (d) Capacity retention with corresponding Coulombic efficiency (CE) at room temperature over cycling.

Galvanostatic charge/discharge measurement further revealed a stable cycling performance of the cell. The initial charging capacity at a current density of 0.2 C reached 143 mA h g^{-1} (Figure 3.4c), almost the theoretical capacity of ferrocene (145 mA h g^{-1}). A reversible capacity of ~130 mA h g^{-1} was achieved from the second cycle. An incomplete oxidation of ferrocene around 10% was observed, which was caused by the diffusion-controlled electrochemical process. The potential was rather stable upon cycling and the average discharge potential reached 3.5 V. The overpotential was decreased from ~200 mV for the 1st cycle to ~150 mV at the 2nd cycle, and further decreased to less than 100 mV at the 50th cycle, which is probably due to a gradually decreased interfacial resistance between the solution and the current collector. The capacity retention was rather stable on cycling (Figure 3.4d), ~90% of the initial

discharge capacity could be maintained after 250 full charge/discharge cycles with capacity decay ~0.4‰ per cycle. The Coulombic efficiency immediately reached ~98% at the 2nd cycle and stabilized between 98–100% thereafter.

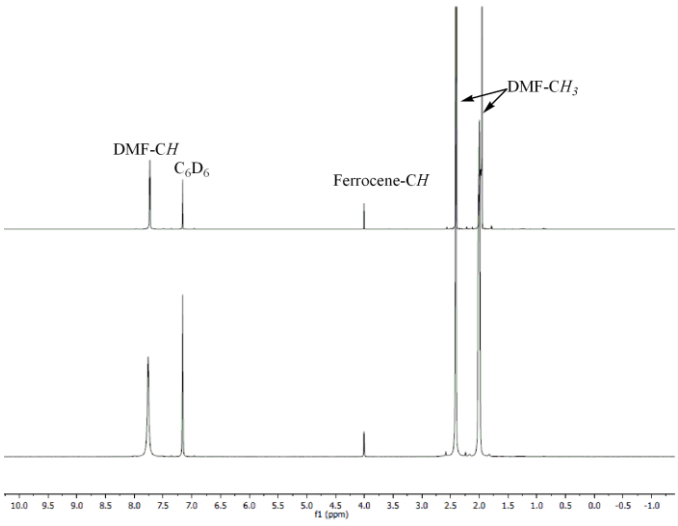

Figure 3.5: ^{1}H NMR spectra of (a) as-prepared ferrocene-EC/DEC catholyte, and (b) cycled ferrocene-EC/DEC catholyte. (C_6D_6, 400 MHz, 22^{o}C). ^{1}H NMR (C_6D_6, 400 MHz): 7.76 (s, DMF-CH), 4.01 (s, Ferrocene-CH), 2.41 (s, DMF-CH_3), 2.01 (s, DMF-CH3) ppm.

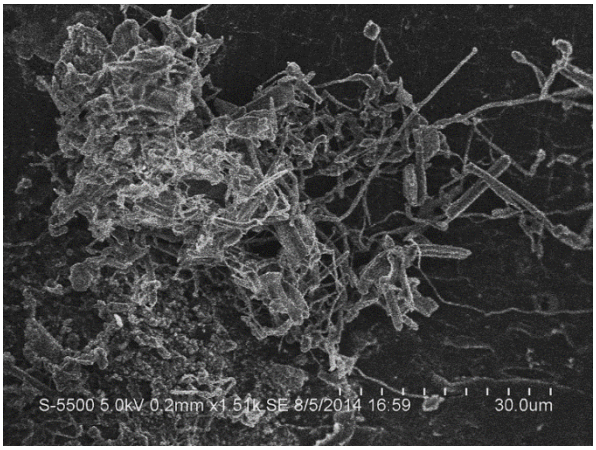

Figure 3.6: SEM image showing the formed Li dendrites upon cell cycling.

The NMR analysis (Figure 3.5) of the cells before and after cycling shows that the sharp peak of ferrocene ligand was not changed, indicating the ligands of ferrocene are stable in the DMF-based electrolyte. The gradual capacity loss should be attributed to the anode on which Li dendrites (Figure 3.6) form upon cycling and detach from the current collector. Although the observed degradation of the LATP separator by Ti (IV) reduction when in direct contact with detached Li dendrite is rather slow, as evident by the slightly increased cell resistance (Figure 3.7), the LATP membrane does not show any structural deformation (Figure 3.8).

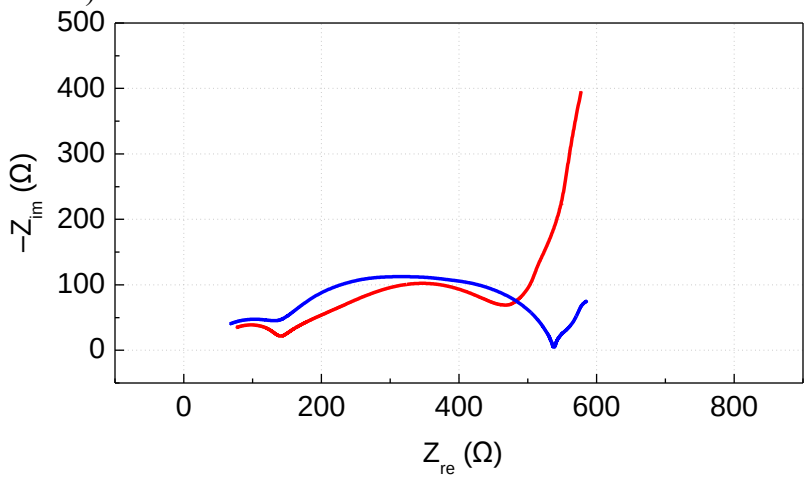

Figure 3.7: Nyquist plot of a fresh cell (red) and a cycled cell (blue) measured in frequency range of 10^6–0.01 Hz.

In summary, the ferrocene/ferrocenium redox reaction in an aprotic solvent can be applied in a liquid cathode Li–ion redox battery for efficient electrical energy storage. The electro-active ferrocene/ferrocenium redox couple exhibits rapid redox kinetics with specific capacity over 130 mA h g^{-1}. The redox reaction is highly reversible and efficient as the capacity maintains ~90% after 250 fully charge/discharge cycles and Coulombic efficiency reaches 98–100%. The cell shows a power density of 120 W kg^{-1} based on the total weight of the liquid cathode, comparable to most current battery technologies. In

addition, the liquid cathode is stable upon cycling and shows a mild reaction when short circuited with metallic Li, thus making it a sustainable and safe energy storage medium. The ferrocene/ferrocenium redox couple has also been shown to work in a Na–ion battery with a semi-permeable membrane.

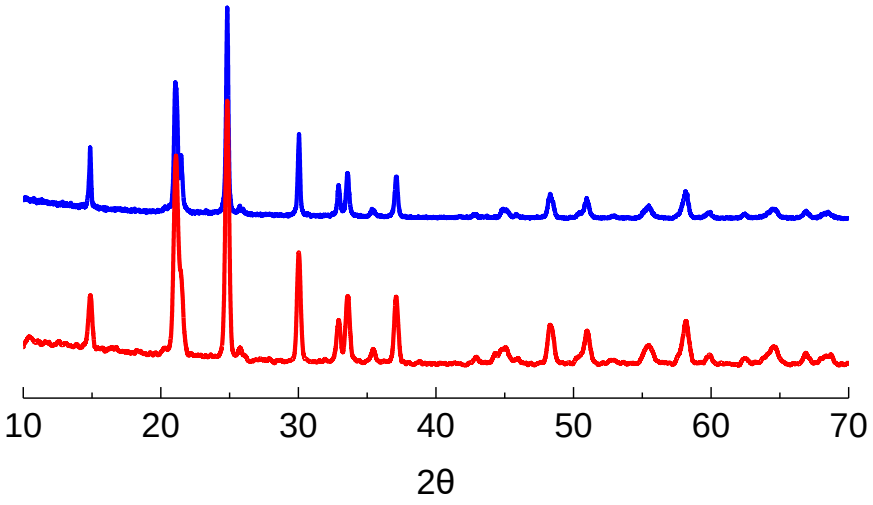

Figure 3.8: XRD patterns of the $Li_{1+x+3z}Al_x(Ti,Ge)_{2-x}Si_{3z}P_{3-z}O_{12}$ membrane before (red) and after (blue) cycling. Both membranes before and after cycling test show the same pattern composed of NASICON-type $LiTi_2(PO_4)_3$ as the main phase and $AlPO_4$ as the secondary phase.

3.3 A FERROCENE-BASED MEMBRANE-FREE HIGH-RATE SEMILIQUID BATTERY*

3.3.1 Introduction

With the rapid development of renewable energy technologies, energy storage devices play an increasingly important role in our daily lives. Li−ion batteries, though restricted by relatively low rate capability and high manufacturing cost, have been considered as one of the most dominant battery technologies for electrical energy storage owing to their high energy density and efficiency.[43] Aqueous RFBs, though providing the possibility in grid-scale electrical energy storage applications in terms of low-cost and modulated cell design, the low energy/power density and efficiency must be addressed.[3] Capacitors may provide superb power density, but their energy density is too low to widen the practical applications for electrical energy storage.[44] Recent studies suggested that capacitive-like batteries might fill the gap between batteries and capacitors.[45] However, their storage capacity still showed strong dependence on current rate, inheriting from a solid electrode configuration with limited diffusion rate in conventional electrode materials unless scaling down the electrode particle size to shorten the mass diffusion length, and/or taking advantage of a pseudocapacitance near the particles' surface. Both strategies require a large electrode surface area which decreases the volumetric energy density. Generally speaking, the rate capability is dominated by four factors: i) transference of ions in the electrolyte, ii) diffusion of ions in the electrode, iii) kinetics of the electrochemical reaction, and iv) transport of electrons in electrode and current collector. Using a liquid electrode configuration might fulfill the above requirements to achieve a decent rate capability. The mass transport in a liquid phase is significantly

* Y. Ding, Y. Zhao, G. Yu, A membrane-free ferrocene-based high-rate semiliquid battery, *Nano Lett.*, 2015, 15, 4108.
Y. D. carried out the experimental work and co-led the writing of the manuscript with Prof. Yu.

faster than that in a solid phase; the electron transfer across a liquid/solid (current collector) interface is generally facile. In addition, the redox kinetics can be enhanced by proper catalysts and design of electrode architectures. Moreover, the liquid nature of the electrode contributes to the flexibility, scalability, and modularity of the cell design.

Recently, Li−S flow batteries based on polysulfide dissolved in organic solvents as catholyte have been demonstrated.[46] The dissolved polysulfides have been proven to facilitate the electrochemical utilization of sulfur. However, these batteries can only work at a C-rate of 0.2−1 with power density less than 100 W L^{-1} due to the slow reaction kinetics of polysulfides. In addition, the cyclic performance is still hampered by the volume change and the shuttle of polysulfide to the anode. Other dissolved redox couples either in an aqueous phase or an aprotic phase as liquid electrode have also been demonstrated. However, the use of a solid electrolyte with low Li^+ conductivity greatly restricted the power performance of the cell.[47] The utilization of alternative chemistries or employing varied combinations of electrode couples as well as electrolytes is needed.

Here we report a ferrocene-based membrane-free semiliquid battery capable of providing a sufficient high rate capability while maintaining nearly constant discharge capacity. Previous studies on ferrocene and its derivatives as electroactive materials for battery applications have been mainly focused on polymeric materials in which ferrocene groups are covalently anchored to the polymeric backbones.[48] However, the high molecular weight of the polymeric backbones and low utilization ratio of decorated ferrocene groups make the energy/power density of such batteries relatively low compared with that of ferrocene-containing catholyte. In this study, a non-aqueous ferrocene catholyte with a passivated metallic Li anode was directly assembled as a membrane-free semiliquid battery.

3.3.2 Experimental

To achieve Li anode passivation, Li metal was soaked in 0.2 M $LiNO_3$/0.5 M LiTFSI in DOL/DME (volume 1:1) to form a protective layer in advance.[49] The passivated Li metal was extensively rinsed with EC/DEC electrolyte before use. In the self-discharge test, the passivated Li metal was cut into one 0.5 cm × 0.5 cm plate, and then immersed into a catholyte of 1 mM ferrocenium in EC/DEC. The reaction between passivated Li and ferrocenium catholyte was monitored by UV-vis spectroscopy in the wavelength range 300−800 nm at different time intervals.

To assemble the battery, carbon paper was punched into circular disks with diameter of 12 mm as current collector. Ferrocenium hexafluorophosphate with concentrations of 0.05, 0.1, 0.2, 0.4 and 0.6 M with 1 M $LiPF_6$ and 0.1 M $LiNO_3$ in EC/DEC (volume 1:1) was prepared as catholyte with mass loading in the range of 0.2−2.4 mg cm^{-2}. The electrochemical performance of the cell was evaluated in a 2032 coin cell. First, 10 μL catholyte was added into the carbon paper current collector, which was covered by a Celgard® 2400 separator, and 5 μL blank organic electrolyte was added between the Celgard® 2400 separator and passivated Li metal anode. The cut-off voltage was set to 2.6−3.8 V. The density of carbonate electrolyte was about 1.2 g cm^{-3}; thus the conversion coefficient from W L^{-1} to W kg^{-1} is estimated to be the reciprocal of 1.2, which is 0.83.

The galvanostatic charge/discharge measurements and polarization test were carried out on a BioLogic VMP3 potentiostat. RDE tests were performed with a BioLogic RRDE-3A rotating ring disk electrode apparatus. A glassy carbon electrode tip and a platinum wire were used as the working electrode and counter electrode, respectively. The reference electrode was Ag/AgCl (0.01 M $AgNO_3$/0.1 M TBAP in acetonitrile). UV-

vis spectra were recorded on Thermo scientific Evolution 300. SEM images were recorded using Hitachi S-5500 scanning electron microscope (S-5500).

3.3.3 Results and Discussion

The working principle of the capacitive cell involves fast, reversible one-electron transference between ferrocene and ferrocenium at a potential around 3.4 V vs. Li^+/Li upon charge/discharge at the cathode and deposition/stripping of Li at the anode, respectively. The rationality of this design relies on three aspects: first, ferrocene/ferrocenium is a Nernstian reaction having a sufficiently high rate constant in various solvents, which distinguishes it from the quasi-reversible redox reactions in most conventional RFBs;[50] second, given the sluggish reaction between ferrocenium and the passivated Li metal, the self-discharge effect is minimal with respect to the rapid charge/discharge cycles; and third, as a prototypical metallocene, ferrocene is highly soluble in most organic solvents with solubility exceeding 1.5 M in ether-based solvents, which promises a superior energy density over conventional redox-flow batteries also taking account of the high redox potential. This designed cell could be operated at the high current rate of 60 C without kinetic barriers.

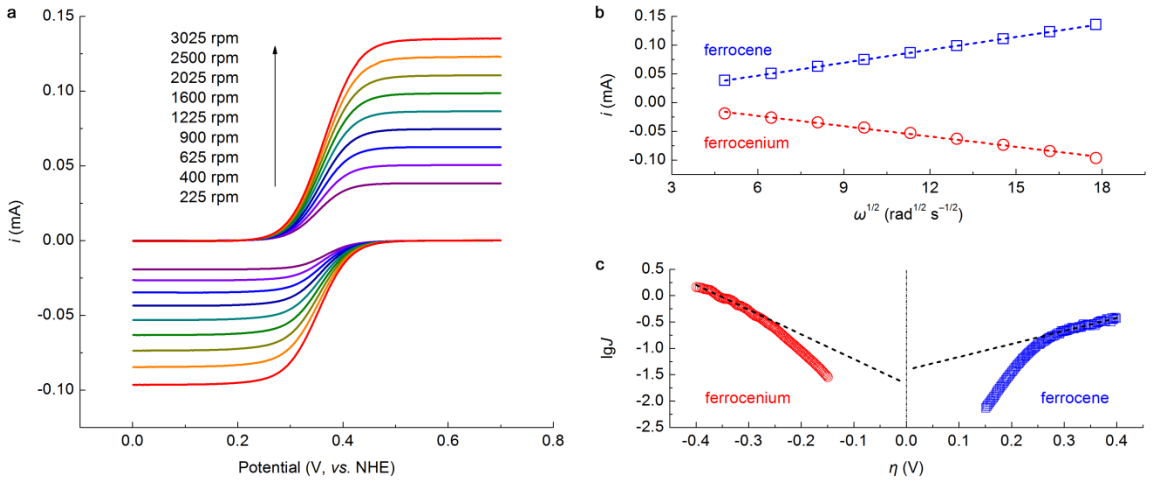

Figure 3.9: RDE measurement of ferrocene and ferrocenium catholyte. (a) RDE voltammograms of 5 mM ferrocene and 5 mM ferrocenium on glassy carbon electrode in 1 M $LiPF_6$ EC/DEC electrolyte at various rotation speeds ranging from 225 rpm to 3025 rpm at scan rate of 5 mV s^{-1}. (b) Relationship between Levich current versus square root of rotation rate for ferrocene and ferrocenium. (c) Tafel plots (the logarithm of current density, lgJ, versus overpotential, η) of ferrocene and ferrocenium at the rotation speed of 3025 rpm.

The rate capability of the ferrocene-based liquid battery is exclusively dominated by mass diffusion rate and redox reaction kinetics of ferrocene/ferrocenium redox couple since Li stripping/deposition on a Li anode usually shows little hysteresis. RDE measurement was first carried out to reveal the redox behaviour of the ferrocene/ferrocenium catholyte. Figure 3.9 shows the RDE voltammograms of ferrocene and ferrocenium catholyte, respectively. The relationship between Levich current and rotation speed under mass-transfer-limited condition is established by Levich Equation as shown below:

$$i_{lim} = 0.620 \times nFAD^{2/3}\omega^{1/2}v^{-1/6}C$$

where i_{lim} is Levich current, n is the number of electrons transferred (n = 1 for ferrocene/ferrocenium), F is Faraday constant (96485 A s mol^{-1}), A is the area of rotation

disk electrode (0.0707 cm^2), D is the diffusion coefficient, ω is rotation speed, v is the kinematic viscosity (~3.4 × 10^{-2} cm^2 s^{-1} at 298K), C is the bulk concentration of the reactants (5 × 10^{-6} mol cm^{-3}). The Levich current showed good linear response with the square root of rotation speed as shown in Figure 3.9b. The calculated diffusion coefficient for ferrocene and ferrocenium is 3.2 × 10^{-6} cm^2 s^{-1} and 2.2 × 10^{-6} cm^2 s^{-1} respectively, which are comparable to the redox couples used in conventional aqueous RFBs, but several orders of magnitudes higher than Li ions in solid electrode materials for Li−ion batteries.[51,52] According to Koutecky−Levich analysis, the reaction rate occurring on electrode surface should be limited by a combination of mass transport and reaction kinetics. The kinetic current (i_K), which is in absence of mass transport limitation, could be obtained by using Koutecky−Levich equation shown:

$$i^{-1}=i_K^{-1} + i_{lim}^{-1}$$

The relationship between i_K and overpotential (η) can be obtained by applying the Tafel equation in Equation:

$$\eta = \alpha + b\lg i_K$$

The plot of η versus $\lg i_K$ should be linear in high overpotential range accordingly. Extrapolating the Tafel plot to the equilibrium potential as shown in Figure 3.9c gave the equilibrium current (i_0), through which the heterogeneous rate constant k_0 could be determined by the equation below:

$$i_0 = nFAk_0C$$

The calculated k_0 for ferrocene oxidation was 7.7 × 10^{-2} cm s^{-1} similar to that of 5.2 × 10^{-2} cm s^{-1} for ferrocenium reduction. The rate constant of ferrocene/ferrocenium redox reaction in EC/DEC electrolyte is much greater than those commonly used in conventional RFBs (Table 3.1).[52] This high rate constant between ferrocene and ferrocenium is the result of a simple electron-transfer process involving only electron

transfer and capture without significant alternation in the molecular form. In light of Butler−Volmer model of electrode kinetics, a system with a large k_0 would achieve equilibrium on a short time scale and the output current should be proportional to the rate constant. Therefore, the liquid battery based on ferrocene/ferrocenium catholyte should be able to provide a larger power density compared to conventional RFBs. The efficiency of the ferrocene-based liquid battery is strongly dependent on the shuttle effect since Li is in direct contact with dissolved ferrocenium cations. To demonstrate that the shuttle effect could be greatly suppressed by proper passivation of a Li anode, the reaction between ferrocenium and passivated Li was monitored by UV-vis adsorption spectra (Figure 3.10). The intensity of the adsorption peak of ferrocenium barely changed in a time scale of four hours when passivated Li was soaked in ferrocenium catholyte. Even after soaking for one day, the absorbance still maintained over 80% of that of the fresh catholyte. Therefore, it's reasonable to conclude that the inconspicuous shuttle effect would not seriously lower down the overall efficiency of the cell.

Redox couple	**Standard rate constant (cm s^{-1})**	**Electrode**
Fe^{3+}/Fe^{2+}	1.2×10^{-5}	Au (111)
Cr^{3+}/Cr^{2+}	2×10^{-4}	Hg
VO_2^{+}/VO^{2+}	3×10^{-7}	Graphite
V^{3+}/V^{2+}	4×10^{-3}	Hg
Ce^{4+}/Ce^{3+}	1.6×10^{-3}	Pt
Br_2/Br^{-}	5.8×10^{-4}	Vitreous carbon

Table 3.1: Standard rate constant of redox couples in conventional RFBs

To verify the rapid redox kinetics and the reliable reversibility, evaluation on the rate capability and cycling stability have been carried out for the ferrocene-based liquid cell. A polarization test was first conducted as illustrated in Figure 3.11, which revealed

that the momentary peak power output achieved ca. 4700 W L^{-1} with discharge potential above 2 V at a current density of 40 mA cm^{-2} or a corresponding C-rate of ca. 370.

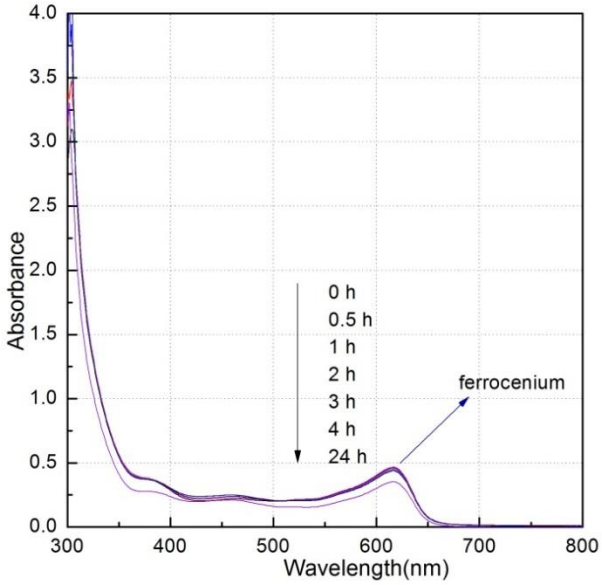

Figure 3.10: Reaction of passivated Li metal with ferrocenium investigated by UV-vis spectroscopy. Passivated Li metal was immersed into ferrocenium/EC/DEC/$LiPF_6$ solution and the spectra were recorded after some intervals.

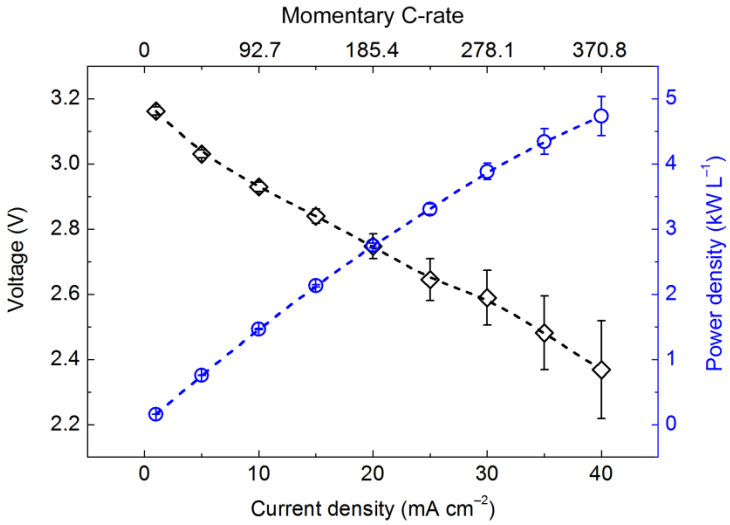

Figure 3.11: Polarization curve of the ferrocene-based liquid battery. The cell with 0.2 M ferrocenium catholyte was discharged at constant current densities of 1−40 mA cm^{-2}. The cell was fully charged after each discharge.

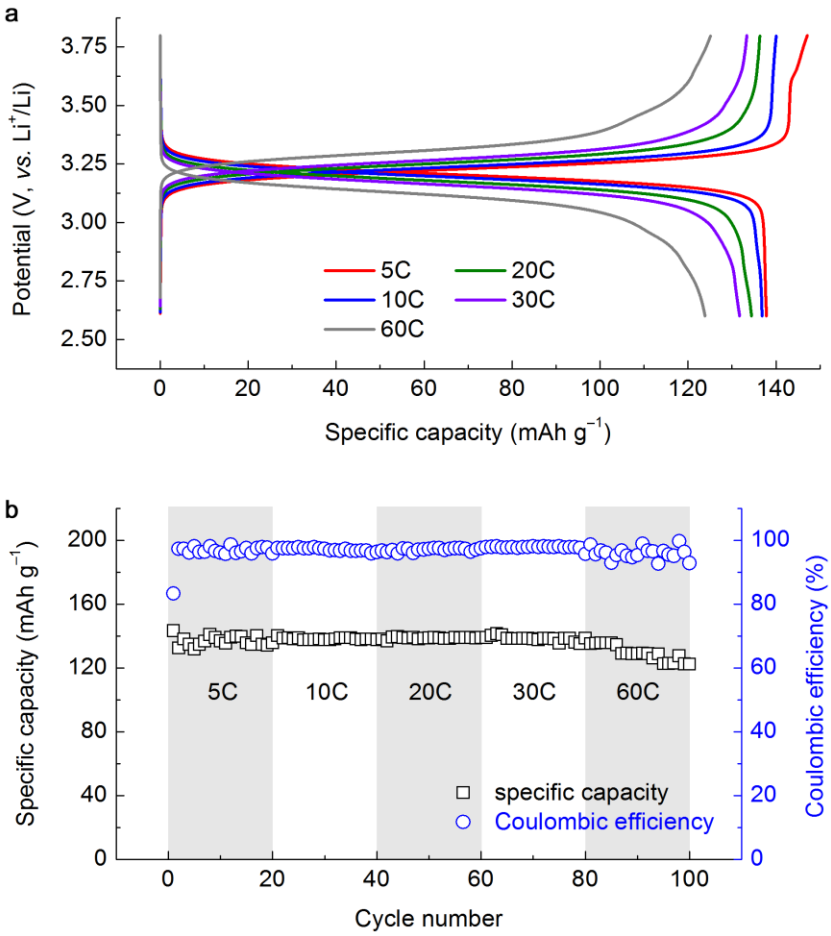

Figure 3.12: Rate capability of the ferrocene-based liquid battery. (a) Typical charge/discharge curves and (b) Discharge capacity retention and corresponding Coulombic efficiency under different current rates of 5 – 60 C.

The full charge/discharge behaviour of the battery cell was further characterized by galvanostatic cycling at different rates as summarized in Figure 3.12. The cell exhibited small polarization and capacity loss when the current rate was below 30C as shown in Figure 3.12a. The specific capacity reached 137 mAh g^{-1} (~94% of the theoretical capacity) at 5 C, and slightly decreased to 132 mAh g^{-1} at 30 C (still ~91% of the theoretical capacity). In comparison, the polarization became more obvious when the current rate was increased to 60 C, and the corresponding specific capacity was 125 mAh

g^{-1} (~86% of the theoretical capacity). The battery cell showed stable capacity retention and high Coulombic efficiency (stabilized between 95−100%) in a wide range of current rates as summarized in Figure 3.12b. The capacity loss was only 10% when the current rate increased from 5C to 60C, indicating an advantageous kinetic process in such a liquid battery compared with those with solid-state electrodes. The performance bottleneck of the former is controlled by redox kinetics since the diffusion of electroactive species is not the barrier. At low to moderate rates, both the diffusion and redox kinetics are sufficiently high that the capacity loss or polarization is mainly dependent on the applied current, especially when taking account of the internal resistance of the cell. At high C-rate, the redox kinetics cannot sufficiently support large applied currents; therefore, the capacity loss and polarization become more obvious. In contrast, the capacity of a solid-state electrode is strongly dependent on the applied current since most of the electrochemical processes in a solid-state electrode are typically diffusion-controlled.[53] The decent rate capability of the designed battery should be attributed to three key factors: first, thanks to the fast mass diffusion in the liquid phase and the large reaction constant of the ferrocene/ferrocenium redox reaction, both the concentration polarization and electrochemical polarization are effectively minimized;[54] second, the highly conductive porous matrix of carbon paper contributes to efficient electron exchange between the catholyte and the current collector, thus alleviating ohmic polarization; and finally, the passivation of Li metal significantly slows down the shuttle effect, so that the ideal Coulombic efficiency could be achieved. SEM images of fresh Li anode and the passivated Li anode before and after cycling show clearly a layer of protective film on the surface of Li metal (Figure 3.13), which plays a key role in maintaining such good cycling performance.

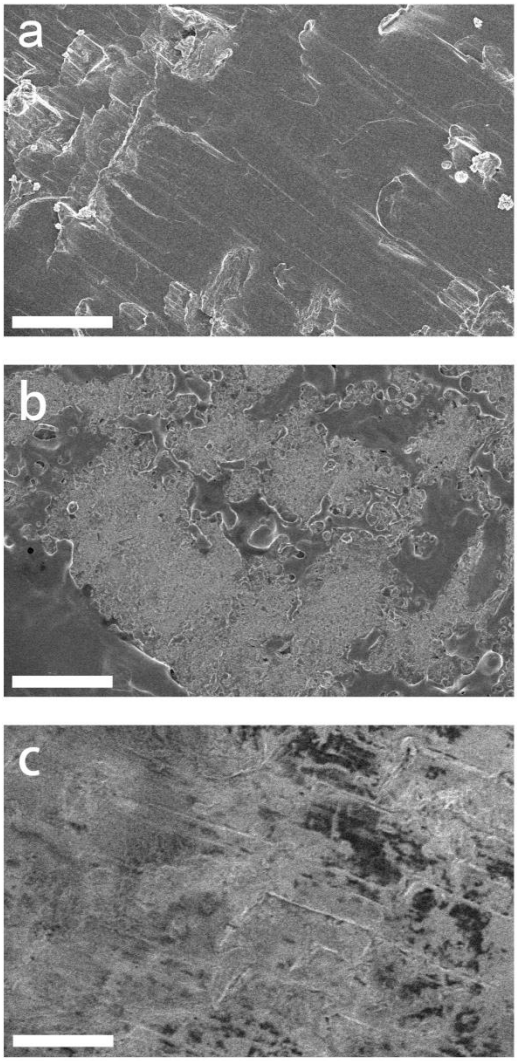

Figure 3.13: SEM images of (a) fresh Li electrode, scale bar is 200 μm; (b) passivated Li electrode, scale bar is 200 μm; (c) passivated Li electrode after cycling test, scale bar is 200 μm.

In summary, a 3 V membrane-free semiliquid battery composed of a ferrocene-based catholyte and a passivated Li anode is demonstrated to exhibit excellent capacity retention with negligible capacity loss during fast charge/discharge up to a current rate of 60 C. The cell delivers a power density and an energy density in excess of 1400 W L^{-1} and 40 Wh L^{-1}, respectively, and shows stable cycling performance with an average

capacity retention of 99.96% per cycle, and high Coulombic efficiency as well as energy/voltage efficiencies. The overall performance of the demonstrated cost-effective liquid battery is comparable to present Li−ion batteries and supercapacitors while offering a significant improvement over most state-of-the-art aqueous or non-aqueous RFBs reported thus far. The rapid redox kinetics together with other attractive features such as reliable stability, structural diversity for performance enhancement, and elemental abundance make the ferrocene-based capacitive cell a promising sustainable energy storage device with high rate capability and safety.

3.4 A HIGH-PERFORMANCE ALL-METALLOCENE-BASED, NON-AQUEOUS RFB*

3.4.1 Introduction

A RFB is akin to a fuel cell in that they both require a continuous source of redox-active materials to sustain the chemical reaction. Fuel cells based on hydrogen or synthetic fuels, however, are commonly considered as energy conversion devices and cannot be electrically reversed efficiently. Therefore, fuels cells are more promising in electric vehicle application considering their merits of high energy density, zero-emission and higher efficiency than diesel or gas engines.[55] As for flow batteries, these devices are of great importance as secondary or rechargeable batteries, especially for grid-scale electrical energy storage applications. The general criteria for an ideal RFB include: i) high solubility of the active materials so as to minimize the storage volume/mass and achieve high energy densities; ii) suitable formal potentials of the redox couples in order to maximize the cell voltage; iii) fast heterogeneous reaction rate which limits the power density; iv) stability of the active materials which is related to the cycle life; and v) safety, cost and abundance of the active materials considering commercial applications. A number of redox couples have been proposed for such systems in conventional RFBs.[56] A difficulty in these energy storage devices is the inevitable crossover of the components between the two half-cells because of imperfect separators or membranes, which leads not only to loss of capacity and efficiency but more seriously to the contamination of electroactive species.[57]

Recently, Li-RFBs using Li ions as charge carriers were proposed and intensively investigated.[4] The potential window is broadened in aprotic electrolyte, but the main

* Y. Ding, Y. Zhao, Y. Li, J. B. Goodenough, G. Yu, A high-performance all-metallocene-based, non-aqueous redox flow battery, *Energy Environ. Sci.*, 2017, 10, 491.
Y. D. carried out the experimental work and co-led the writing of the manuscript with Prof. Yu.

challenges of these Li-RFBs arise from the lack of proper anode-active materials with desired redox potential and reversibility.[14] Presently, metallic lithium is usually used as the anode. Despite its great electropositivity, the major disadvantage lies in safety issues resulted from dendritic and mossy lithium growth and low Coulombic efficiency due to electrolyte decomposition under such low potential of Li^+/Li.[58] Though some organic-based anode materials have been proposed, the redox potential is relatively high, usually > 2.5V vs. Li^+/Li, thus restricting the working potential of full battery (< 2V).[59] Recent investigations suggest that organometallic compounds such as metallocenes might be good alternatives to displace those inorganic-based redox couples used in conventional RFBs.[60] Typically metallocene is a compound consisting of two cyclopentadienyl (Cp) ligands, C_5H_5, bound to a metal center (M) in the oxidation state of II on opposite sides. It's known that the π-orbitals of the Cp rings and the d-orbitals in the metal center are mainly in charge of the coordination and chemical reactivity. Different electronic structures, together with the variation of the M-C bonds and the valence electron count, gives rise to different properties.

Metallocenes and their derivatives were investigated as catalysts in the early stage. Together with a co-catalyst, metallocene has been adopted as a homogeneous Ziegler-Natta catalyst in olefin polymerization.[61] Moreover, the use of metallocenes in electron-transfer processes, as anticancer reagents, as fuel additives, in bioorganometallic chemistry, has contributed greatly to the rapid growth and rapidly moving frontiers of these compounds.[62] Despite the wide prospect of metallocene-based materials, insight into their applications in energy storage has just recently been proposed. Generally speaking, the redox reaction between metallocene and its onium is a standard reversible process with broad potential range, which should be associated with the particularly simple electron-transfer process involving only electron transference without significant

alternations in the molecular form. What's more, the solvent dependence of metallocenes affects both physical and chemical properties as well, making rational design of Li-RFBs possible by screening proper metal centers and corresponding solvents.

3.4.2 Experimental

The cell assembly process was similar to that given in previously chapters. Briefly, Ti foil coated with acetylene black/PVDF works as current collector for both cathode and anode, and the battery module was built with LATP as separator sandwiched between two quartz shells. All the joints were sealed together with Surlyn® resin. Then the module will be transferred to a glove box to inject electrolyte using a syringe. The flow mode battery assembly process is almost the same; the difference is that two modified cathode quartz shells with two hose barbs were used. Schematics of battery components, static mode battery and flow mode battery are shown in Figure 3.14. In dQ/dV curves, the $FeCp_2$ based catholtye contains 0.1 M $FeCp_2$, 0.5 M $LiPF_6$ in N,N-dimethylacetamide (DMA) or DMF; or 0.1 M $FeCp_2$, 0.5 M LiTFSI in dioxolane (DOL) or tetrahydrofuran (THF). The $CoCp_2$ based anolyte contains 0.1 M $CoCp_2$, 0.5 M $LiPF_6$ in DMA or DMF; or 0.1 M $CoCp_2$, 0.5 M LiTFSI in DOL or THF. The $CoCp'_2$ based anolyte contains 0.1 M bis(pentamethylcyclopentadienyl) cobalt ($CoCp'_2$), 0.5 M LiTFSI in DOL. In half-cell test of $FeCp_2PF_6$, the catholyte is composed of 0.1 M $FeCp_2PF_6$, 0.5 M $LiPF_6$ in DMF; For $CoCp_2$, it is composed of 0.1 M $CoCp_2$, 0.5 M LiTFSI in DOL. In full-cell test, the catholyte is composed of 0.1 M $FeCp_2$, 0.1 M $FeCp_2PF_6$, 0.5 M $LiPF_6$ in DMF and the anolyte is composed of 0.1 M $CoCp_2$, 0.5 M LiTFSI in DOL. Different concentrations of catholyte and anolyte were also prepared for comparison. The $CoCp'_2$ based anolyte contains 0.1 M $CoCp'_2$, 0.5 M LiTFSI in DOL. For RDE tests, 3 mM

$FeCp_2$, 0.5 M $LiPF_6$ in DMF, 2.5 mM $CoCp_2$, 2.5 mM $CoCp_2PF_6$, 0.5 M LiTFSI in DOL/DME (volume ratio 1:1) were prepared separately.

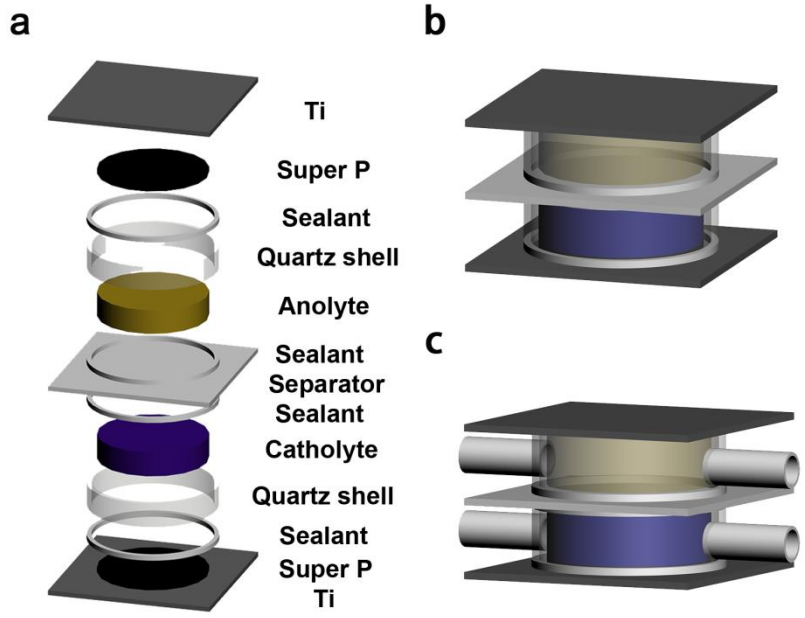

Figure 3.14: (a) Cell components of static mode battery. (b) Schematic of a static mode liquid battery. (c) Schematic of a flow mode battery.

Galvanostatic charge/discharge tests were conducted on a BioLogic VMP3 potentiostat system. RDE measurements were performed on a BioLogic RRDE-3A rotating ring disk electrode with a glassy carbon disk electrode. Specifically, the reference electrode is 0.01 M $AgNO_3$/0.1 M TBAP/CH_3CN, and the counter electrode is platinum electrode. Before all the RDE tests, the solutions were prepared in a glove box and then sealed well. The scan rate was set at 5 mV s^{-1}, and the electrode was rotated at 100, 400, 900, 1600, 2500 and 3600 r.p.m. The limiting current versus the square root of the rotation rate is plotted, from which a diffusion coefficient can be obtained. To fit the Koutecky-Levich equation, the reciprocal of the current at different overpotentials was

plotted, and the intercept at the y axis gives the reciprocal of i_K at different overpotentials. By fitting Butler-Volmer equation, a linear plot of lgi_K versus overpotential can be obtained, and the yielded x-intercept is the log of the exchange current i_0. The rate constant of the redox reaction is proportional to i_0 according to the equation, $i_0=nFAk_0C$, from which we can get the reaction rate constant of 2.0×10^{-3} cm s^{-1} of $FeCp_2$, 5.3×10^{-4} cm s^{-1} of $CoCp_2$, and 1.7×10^{-3} cm s^{-1} of $NiCp_2$.

3.4.3 Results and Discussion

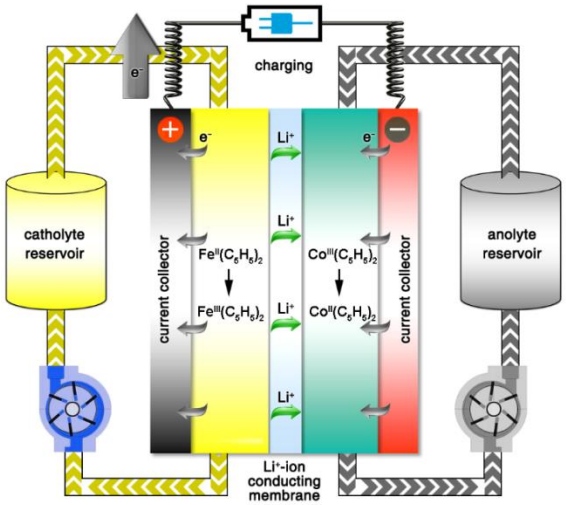

Figure 3.15: Schematic illustration of the working principle of the proposed all-metallocene-based lithium RFB during charging process.

In this research, we propose a prototype all-metallocene based Li-RFB by exploiting proper metallocenes to serve as both cathode-active and anode-active materials as schematically demonstrated in Figure 3.15. A key property of metallocenes is their ability to exist in the form of various oxidation states with a variable number of d-electrons between 14 and 20, which is usually not the case for the other families of inorganic or organometallic complexes. These various oxidation states are characterized by cyclic voltammetry, with each wave corresponding to a change of oxidation state as

summarized in Table 3.2. As a prototype of metallocene, the molecular structure of $FeCp_2$ has been fully explored. It was found that in this sandwich structure the energy barrier separating the staggered (D_{5d} point group) and eclipsed (D_{5h} point group) rotational orientations of the bounded Cp ligands was very small.[63] In idealized D_{5d} symmetry, interaction between two Cp ligands splits the 10 π orbitals into combinations of a_{1g}, a_{2u}, e_{1g}, e_{1u}, e_{2g} and e_{2u}. Similarly, the metal valence orbitals in the ligand field are generated qualitatively into a_{1g}, e_{1g}, e_{2g}, a_{1g}, a_{2u} and e_{1u}. Thereupon the overall molecular orbital is given by the interaction of the ligand orbitals with the center metal orbitals.[33] Molecular orbitals of $CoCp_2$ and its corresponding onium and analogs also follow this order, which was corroborated by subsequent electron spin resonance (ESR) and magnetic susceptibility studies. Similarly the ground-state electron configuration of VCp_2, $NiCp_2$ and other metallocenes can be obtained by tuning the number of electrons to the configuration of $FeCp_2$ respectively.

Compounds	Electronic structure	Unpaired electrons	Redox reaction	Redox potential	Reversibility
Vanadocene	$(e_{2g})^2(a_{1g})^1$	3	$V^{III} + e^- \leftrightarrow V^{II}$	*ca.* −0.7V *vs.* Pt electrode	Reversible
Chromocene	$(e_{2g})^3(a_{1g})^1$	2	$Cr^{II} + e^- \leftrightarrow Cr^{I}$	*ca.* −2.3V *vs.* Pt electrode	Reversible
			$Cr^{III} + e^- \leftrightarrow Cr^{II}$	*ca.* −0.5V *vs.* Pt electrode	Reversible
Decamethylmanganocene	$(e_{2g})^2(a_{1g})^1(e_{1g})^2$	5	$Mn^{II} + e^- \leftrightarrow Mn^{I}$	*ca.* −2.5V *vs.* SCE	Reversible
			$Mn^{III} + e^- \leftrightarrow Mn^{II}$	*ca.* −0.5V *vs.* SCE	Reversible
Ferrocene	$(e_{2g})^4(a_{1g})^2$	0	$Fe^{III} + e^- \leftrightarrow Fe^{II}$	*ca.* 0.5V *vs.* Ag^+/Ag	Reversible
Cobaltocene	$(e_{2g})^4(a_{1g})^2(e_{1g})^1$	1	$Co^{II} + e^- \leftrightarrow Co^{I}$	*ca.* −1.9V *vs.* SCE	Reversible
			$Co^{III} + e^- \leftrightarrow Co^{II}$	*ca.* −0.9V *vs.* SCE	Reversible
Nickelocene	$(e_{2g})^4(a_{1g})^2(e_{1g})^2$	2	$Ni^{III} + e^- \leftrightarrow Ni^{II}$	*ca.* −0.5V *vs.* $FeCp_2^{+/0}$	Reversible
			$Ni^{IV} + e^- \leftrightarrow Ni^{III}$	*ca.* 0.5V *vs.* $FeCp_2^{+/0}$	Reversible

Table 3.2: Electronic structures and redox behaviors of certain metallocenes.

After a systematic study of a series of metallocene, namely, $FeCp_2$, $CoCp_2$ and $NiCp_2$, the electrochemical characteristics of this family of redox species were elucidated. In spite of the fact that $NiCp_2$ maintains both high diffusion coefficient and reaction rate constant, $FeCp_2$ and $CoCp_2$ were selected to construct the all-metallocene flow battery considering the highest potential difference. $FeCp_2$ maintaining a redox potential at as high as 3.7 V vs Li^+/Li in DMF, is selected as the cathode-active species. While $CoCp_2$, which typically shows a redox potential around 1.9 V vs Li^+/Li, serves as anode-active species. Considering the voltage discrepancy, the proposed all-metallocene Li-RFB system should output an operating potential of 1.8 V, higher than conventional flow batteries (< 1.6 V) based on redox species in aqueous medium restricted by the potential window of water. Compared with those semi-liquid batteries directly using Li metal as anode, this Li-metal-free battery can circumvent the potential dangers related to Li anode.[64] In addition, the solubility of metallocenes can be manipulated simply by solvent screening. For instance, the solubility can reach as high as 1.5 M in ethers like tetrahydrofuran or dioxolane. Last but not least, metallocenes maintain highly tailorable properties, and molecular design on Cp rings can tune both the redox potential and solubility furthermore. Therefore, a comprehensive study integrating structural analysis, electrochemical characterization, and battery design is still needed to better elucidate the redox characteristics of metallocene family, especially for organic RFB applications.

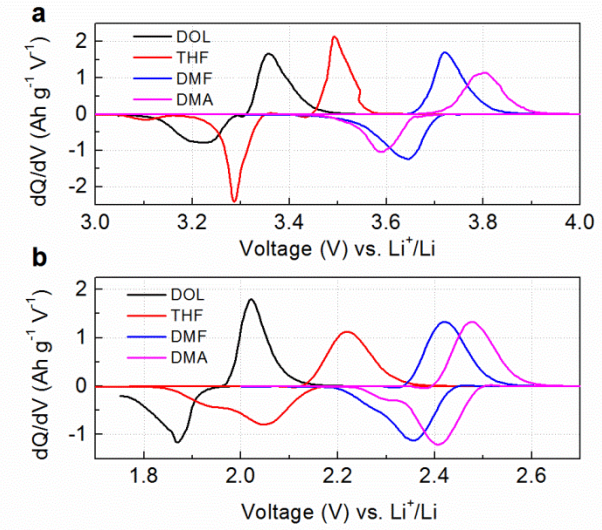

Figure 3.16: Solvent dependence of the redox potential of $FeCp_2$ (a) and $CoCp_2$ (b) in DOL, THF, DMF and DMA. All the current rates are at 0.4 C.

To gain a better understanding of the half-reaction of metallocene, $FeCp_2$ and $CoCp_2$ were subjected to half-cell electrochemical measurements using metallic lithium as anode, respectively. In this study, a home-made cell was adopted to demonstrate the performance, which is composed of a current collector of activated carbon, metallocene in a certain common organic solvent as catholyte, a NASICON-type LATP membrane as separator, and Li metal as anode. The redox behaviors of both $FeCp_2$ and $CoCp_2$ show strong solvent-dependence as the solvent might interact with metallocenes as presented in Figure 3.16. The dQ/dV profiles of 0.1 M $FeCp_2$ and 0.1 M $CoCp_2$ at 0.4 C in DOL, THF, DMF, and DMA indicate that the highest redox potential for both $FeCp_2$ and $CoCp_2$ was achieved in DMA, followed by DMF and THF with DOL being the lowest. One empirical model is constructed to relate any physicochemical quantity to well-known solvent parameters, leading to the expression between the formal redox potential E_f and four contributions:

$$E_f = E_f^0 + \Delta E_p + \Delta E_H + \Delta E_s$$

in which E_f^0 is the formal redox potential without any solvent interactions, ΔE_p is the term associated with the electrostatic interactions between the solvent dipoles and the charges of the redox species, ΔE_H is an interaction related to the changes in internal solvent order contributed by the two oxidation states, ΔE_s indicates the specific solvent effects, such as the hydrogen bonding between solvent and solute, the π-π interaction between solvent and solute and Lewis acid/base interaction.[40] Accordingly the potential shift in different solvents should be contributed to all the four factors. It's found that DMF should be the most suitable for catholyte considering the higher redox potential than DOL/THF and better round-trip efficiency than DMA. Meanwhile, DOL is more suitable than others as the solvent for anolyte since $CoCp_2$ exhibits the lowest redox potential and good round-trip efficiency.

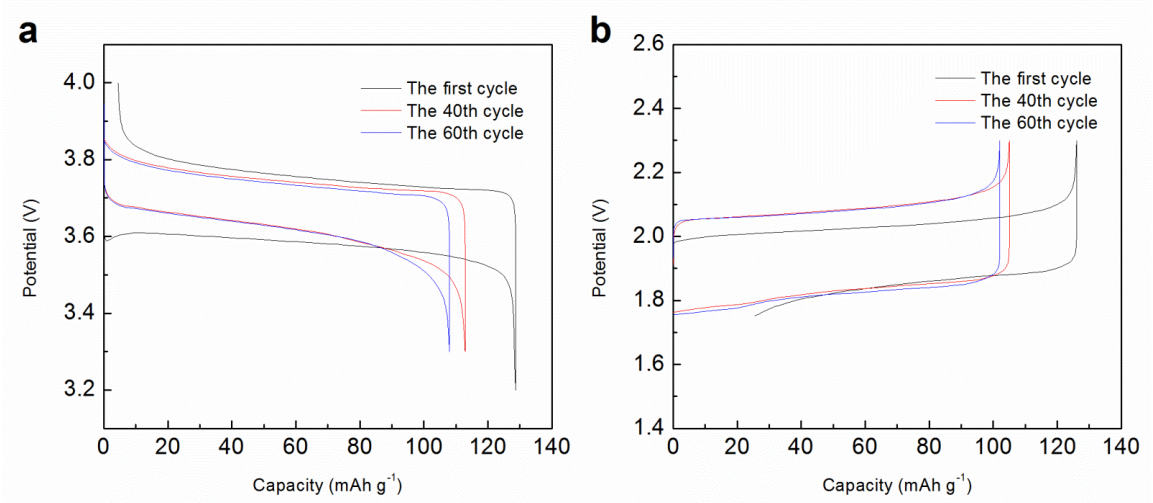

Figure 3.17: Potential vs. specific capacity plot of the half battery at 0.4 C. (a) 0.1 M $FeCp_2PF_6$, 0.5 M $LiPF_6$ in DMF and (b) 0.1 M $CoCp_2$, 0.5 M LiTFSI in DOL.

Figure 3.17 demonstrated the galvanostatic charge/discharge profiles of $FeCp_2PF_6$ and $CoCp_2$ half cells respectively. The initial capacity reached 129 and 127 mAh g^{-1} for $FeCp_2$ and $CoCp_2$, respectively, corresponding with ca. 88% of the theoretical capacity.

Given the fast reaction kinetics and high diffusion coefficient, the untapped capacity should be due to limited Li ion conductivity of the Li ion membrane (~ 10^{-4} S cm^{-1} at room temperature).[65] The charge/discharge capacity was stable with decay about 0.2 % per cycle, and the CE was stabilized to nearly 100 %. It should be pointed out that the alleviated polarization for $FeCp_2$ half-cell upon cycling should be due to the wettability of the carbon current collector and the interface between separator and electrolyte. As for the $CoCp_2$ half-cell, the deteriorative polarization after cycling should result from the passivation of solid electrolyte when the potential reached below −2 V vs. NHE.

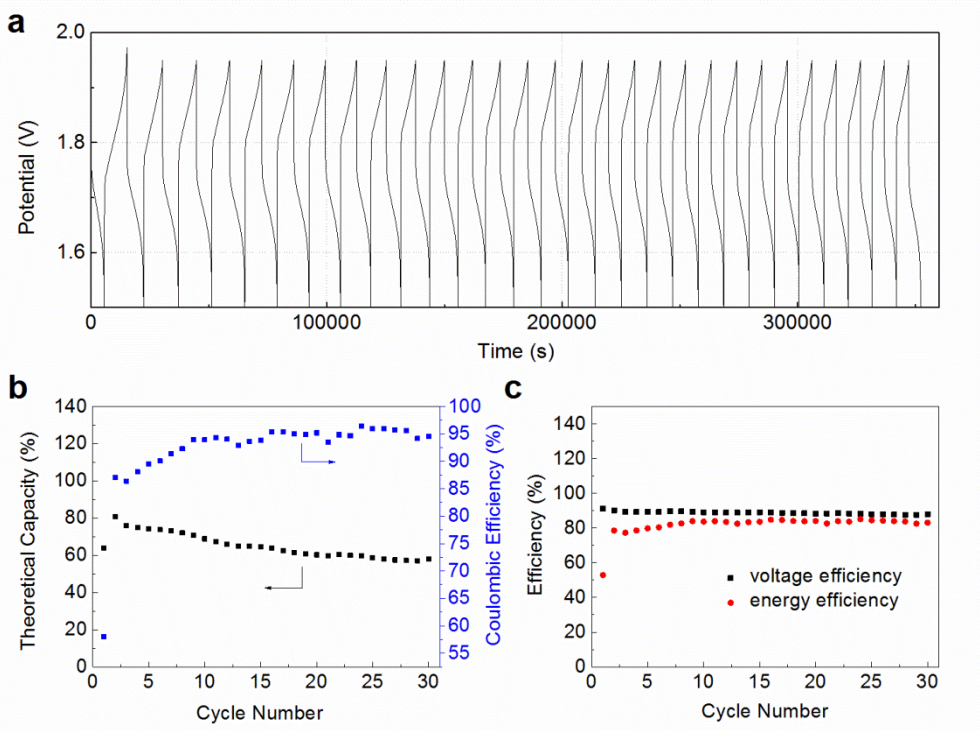

Figure 3.18: Cyclic performance of the full battery using $FeCp_2$, $FeCp_2PF_6$ in DMF based catholyte and $CoCp_2$ in DOL based anolyte at 0.4 C. (a) Potential vs. time plot. (b) Capacity, CE vs. cycle number. (c) Voltage and energy efficiency plot.

Based on these results, an all-metallocene based full cell can be built using $FeCp_2PF_6$ and $CoCp_2$ as the high and low potential active species respectively. As a proof-of-concept system, a similar cell structure was designed, with activated carbon as current collector for both catholyte and anolyte, and LATP membrane as separator sandwiched in between. The anolyte contains 0.05 M $CoCp_2$, 0.5 M LiTFSI in DOL and the catholtye contains 0.05 M $FeCp_2$, 0.05 M $FeCp_2PF_6$, 0.5 M $LiPF_6$ in DMF. The potential-time profile shows that the as-prepared full cell maintains potential at 1.65 V during discharge and 1.75 V during charging, as presented in Fig. 3.18a. This result also correlates well with half cell tests, in which the discharge potential of $FeCp_2PF_6$ reaches about 3.6 V vs. Li^+/Li in DMF and the charge potential of $CoCp_2$ is about 2.0 V in DOL. The steady voltage profile over time demonstrates the reversibility and stability of the metallocene redox species during the electrochemical process. Owing to the LATP membrane separator, the crossover of active species can be limited to the minimum extent considering the stabilized Coulombic efficiency (CE) over 95%. In cycling test the stabilized capacity can reach 81% of the theoretical value in the second cycle, and the capacity retention shows over 99% per cycle with voltage efficiency (VE) over 90% and energy efficiency (EE) about 85%, both of which exceeding most of the current state-of-the-art non-aqueous flow batteries greatly (EE~ 20−50 %).[11] The capacity fading should be due to the imperfect Coulombic efficiency (Figure 3.18b) without unlimited Li sources. Additionally, Figure 3.17 also illustrates capacity degradation of $FeCp_2PF_6$- and $CoCp_2$-based half cell using Li anode. The imperfect Coulombic efficiency might be caused by undesirable side reactions, degradation of LATP membrane, or reaction irreversibility of metallocenes. Given the difference between half cell and full cell, it should be reasonable to see more obvious capacity fading in full cell. It has been reported that a stable resistive solid-liquid electrolyte interphase will be formed on the membrane,

which leads to the increased Coulombic efficiency after cycling in Figure 3.18b. Increasing the concentration of active materials led to higher utilization of the active materials, though the stabilized CE, EE and VE remained almost unchanged (Figure 3.19). Even when the concentration of $CoCp_2$ was lifted to 1 M, the demonstrated volumetric capacity can reach 13.4 Ah L^{-1} (Figure 3.20), which is higher than most of reported non-aqueous RFBs.[66]

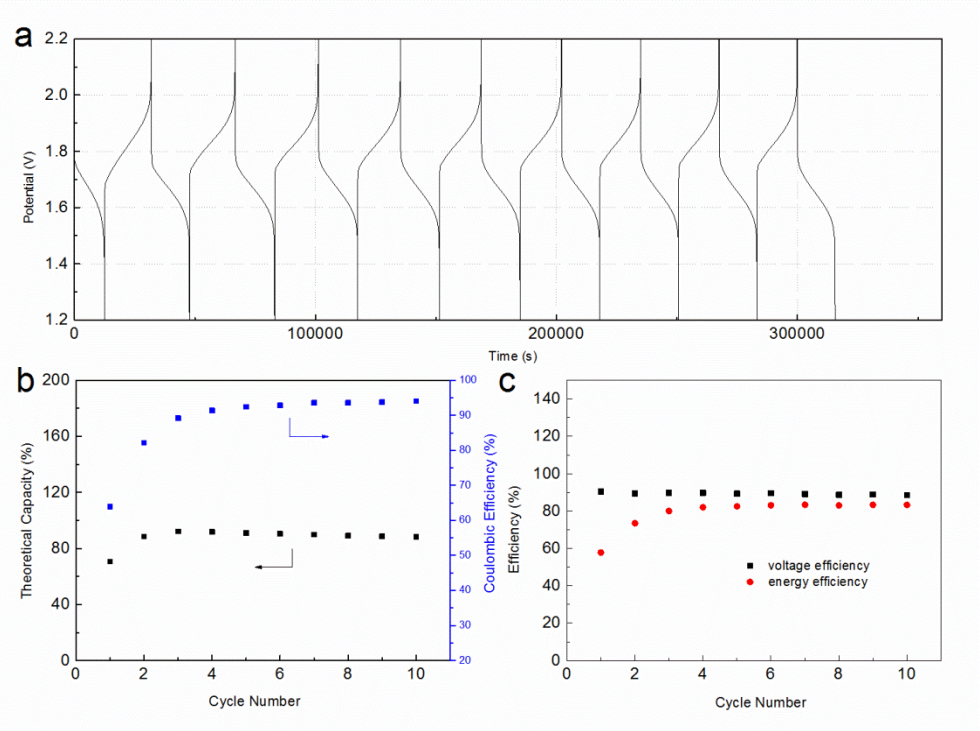

Figure 3.19: Cyclic performance of the full battery using 0.1 M $FeCp_2$, 0.1 M $FeCp_2PF_6$, 0.5 M $LiPF_6$ in DMF on the positive side and 0.1 M $CoCp_2$, 0.5 M LiTFSI in DOL on the negative side at 0.4 C. (a) Potential vs. time plot. (b) Capacity, CE vs. cycle number. (c) Voltage and energy efficiency plot.

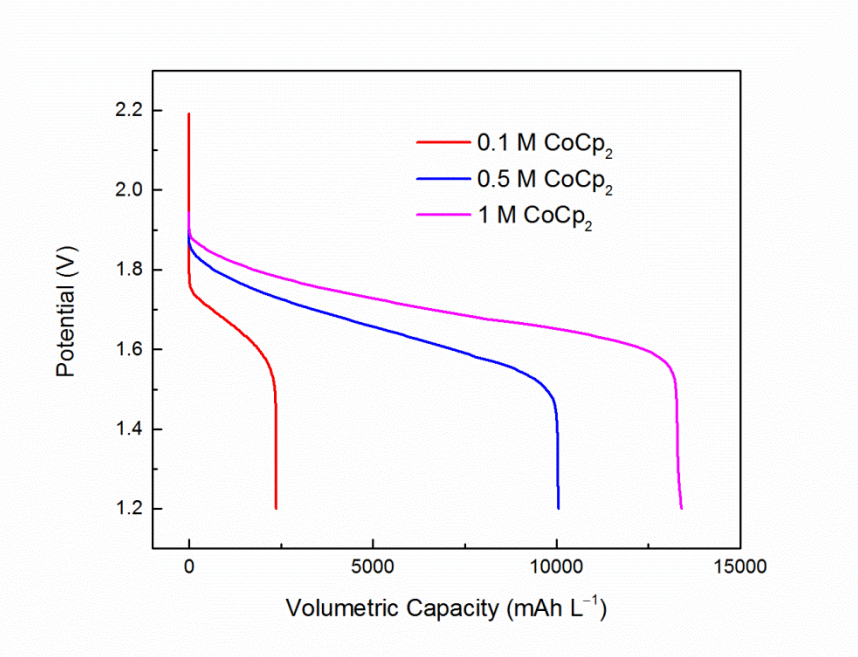

Figure 3.20: Volumetric capacity of the full battery at 0.4 C for 0.1 M $CoCp_2$, 0.1 C for 0.5 M $CoCp_2$, and 0.05 C for 1 M $CoCp_2$.

Furthermore, the performance of a flow-mode battery was also demonstrated. Figure 3.21 shows the polarization curve of the flow mode battery at a flow rate of 4 mL min^{-1}, in which the power density of 1.8 mW cm^{-2} can be achieved at current density of 1.5 mA cm^{-2}. The power density is comparable with reported non-aqueous flow batteries but lower than aqueous flow batteries. Improvement in the battery design or utilization of advanced membranes should lead to enhanced performance.[67]

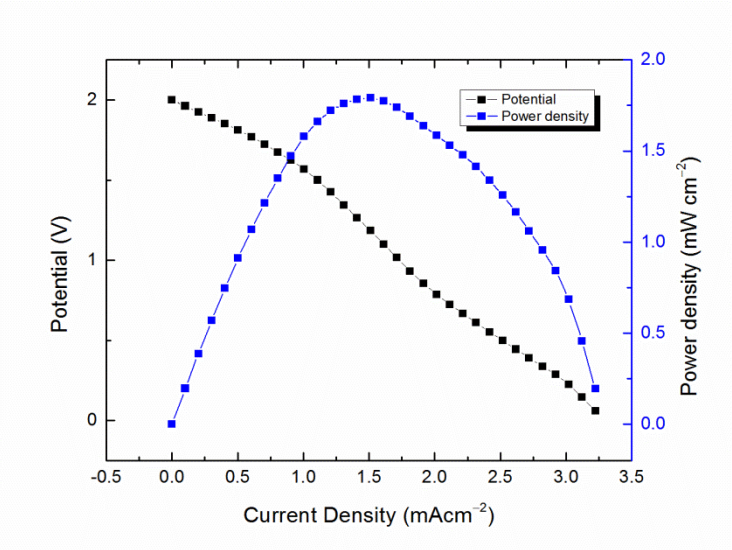

Figure 3.21: Polarization curve for a flow mode battery using 0.1 M $FeCp_2$, 0.1 M $FeCp_2PF_6$, 0.5 M $LiPF_6$ in DMF on the positive side and 0.1 M $CoCp_2$, 0.5 M LiTFSI in DOL on the negative side.

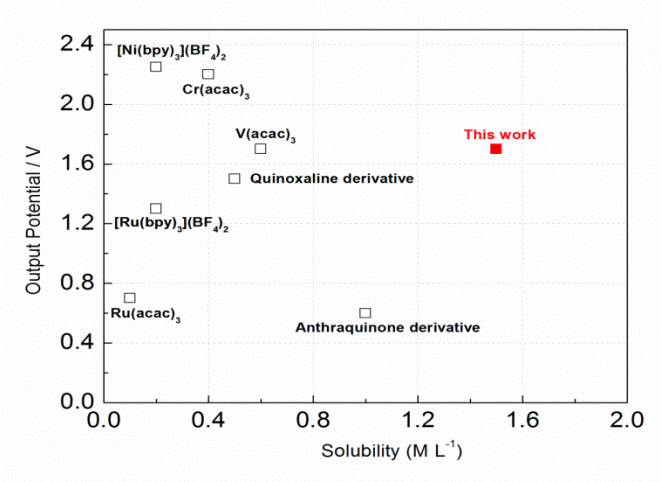

Figure 3.22: Working potential versus solubility of anode-active material of recently developed RFBs.

Compared with recently developed RFBs (Figure 3.22), the all-metallocene based full cell can provide potential comparable with non-aqueous RFBs. Besides, the solubility of the anode-active material can also reach very high (~ 1.5 M), which is usually the

limiting factor for non-aqueous RFBs and Li-RFBs. To further prove the stability of the solid electrolyte when exposed to reductive $CoCp_2$ anolyte, the half cell based on $CoCp_2$ was tested in the potential range of 0.05 V and 2 V (Figure 3.23), and it appears that the reduction of solid electrolyte mostly takes place below 1 V, and this reaction is not reversible. Therefore, the reduction of solid electrolyte will not be an issue, nor contribute to the reversible capacity of the full cell.

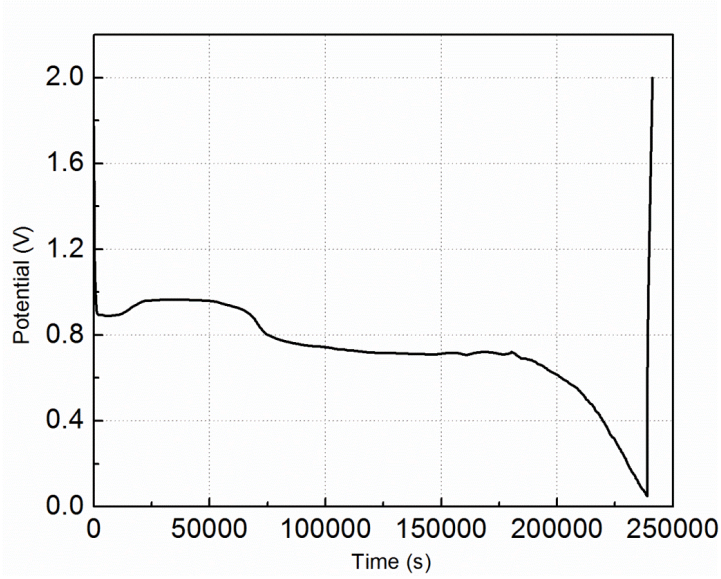

Figure 3.23: Galvanostatic discharge-charge test of 0.1 M $CoCp_2$, 0.5 LiTFSI in DOL vs Li^+/Li between 0.05 V and 2 V at current density of 0.1 mA cm^{-2}.

Different from conventional RFBs based on metal chelates, the Cp rings in metallocenes provide more convenience to tune the physical and chemical properties using molecular engineering method. The oxidation potentials of metallocene derivatives referenced to that of metallocenes should correlate linearly with the HOMO of metallocene derivatives with respect to that of metallocene. Therefore the introduction of electron-donating groups should increase the energy level and then lower the redox potential of metallocenes.[10] Herein bis(pentamethylcyclopentadienyl) cobalt ($CoCp'_2$)

was adopted in the anolyte instead. As illustrated in Figure 3.24a, the oxidation potential of $CoCp'_2$ is decreased to ~1.5 V compared with ~2 V of $CoCp_2$. Thus the working potential of the corresponding full cell is increased to 2.1 V, which is high enough to power up a yellow LED bulb with on-set potential of 2 V (Figure 3.24b). Similarly, functionalization of $FeCp_2$ with electron-withdrawing groups, such as nitro group and cyano group, will also lead to lifted working potential of full cell.[68] However, the utilization of $CoCp'_2$ and the cycling performance is not satisfactory probably due to the poor compatibility of $CoCp'_2$ solution with the LATP solid electrolyte at such low potential. This issue is expected to be circumvented by designing more advanced Li ion conducting membrane with broadened potential window.[69] For example, the Li_3PS_4-based solid electrolyte holds great promise with broadened working potential range of 0.22-5 V, and the $Li_{10}GeP_2S_{12}$ has both a high ionic conductivity and a high decomposition potential as Li ion conducting solid electrolyte.[70,71]

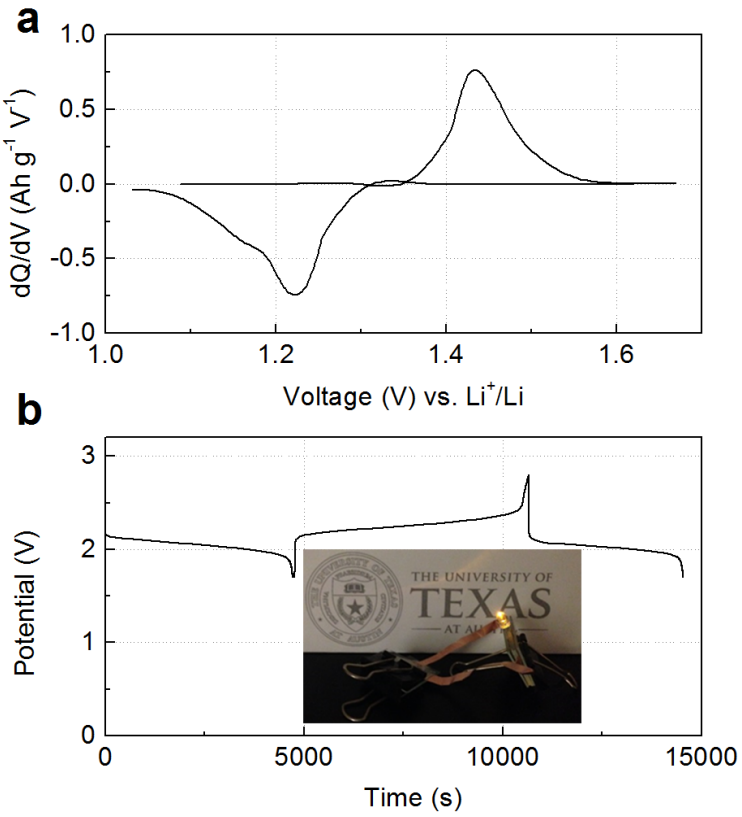

Figure 3.24: (a) dQ/dv vs. potential of $CoCp'_2$ in DOL at 0.4 C. (b) Voltage profile of the full battery using $FeCp_2$, $FeCp_2PF_6$ in DMF based catholyte and $CoCp'_2$ in DOL based anolyte at 0.4 C. at 0.4 C. The inset photograph shows that this modified full battery can provide potential high enough to power yellow LEB bulb.

In summary, using metalorganic compounds, metallocenes, for instance, would enable non-aqueous Li-RFBs to operate at higher cell potentials and to achieve higher energy density and energy efficiency if the structure of metallorganic compounds could be properly modified and functionalized. Here, we investigate a promising non-aqueous Li-RFB which employs $FeCp_2$ and $CoCp_2$ as the cathode-active and anode-active species respectively. $FeCp_2$ demonstrates highly reversible single electron transfer at 3.6 V vs. Li^+/Li whereas $CoCp_2$ shows a relatively low redox potential at 1.9 V vs. Li^+/Li. By

introducing electron withdrawing/donating functional groups on the Cp rings, the redox potential could be potentially further increased/decreased so as to maximize the overall operating potential of the full cell. Moreover, enhanced solubility of redox species in polar organic solvents can be achieved via introduction of long chain ethers, which is beneficial to realize high energy density of flow battery. In this demonstrated proof-of-concept cell, the electrochemical couple of $FeCp_2$ and $CoCp_2$ discharge and charge from 1.6–1.7 V and 1.8–1.9 V, respectively, with capacity decay less than 1% per cycle, and Coulombic and energy efficiencies of ~95 % and ~85 %, respectively. Furthermore, molecular engineering on the anode species boosts the potential of the full cell by 0.5 V, which is high enough to enlighten a yellow LED bulb. Compared with other Li-RFBs based on metallic Li anode, the substitution of the anodes by low-potential redox species can circumvent the safety issues related to the high reactivity and dendrite formation of Li. All these results demonstrate a generic design route towards high performance non-aqueous Li-RFBs by using electroactive organometallic species, which offer the opportunities for the design and synthesis of novel organometallic molecule with tailorable redox potential, solubility, and activity.

Chapter 4: Molecular Engineering of Quinones for Sustainable RFBs

4.1 INTRODUCTION

Carbonyl compounds are the most promising type of organic electroactive material. They feature fast reaction kinetics, great structural diversity, tailorability, and benefit from cost-effective synthesis processes.[72] The first exploration of carbonyls for battery applications can be traced back to 1969, when Williams et al. built a primary battery with a dichloroisocyanuric acid cathode and lithium anode in a non-aqueous electrolyte.[73] Since then, continuous works have been done to broaden the applications of carbonyl compounds for either solid state batteries or RFBs with liquid form electrolytes.[74]

Compound	Formaldehyde	Aldehyde	Ketone	Carboxylic acid	Ester	Amide	Enone	Acyl halide	Acid anhydride
Structure							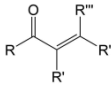		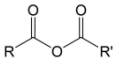
General formula	CH_2O	RCHO	RCOR’	RCOOH	RCOOR’	RCONR’R’’	RCOCR’CR’’R’’’	RCOX	$(RCO)_2O$

Table 4.1: Different types of carbonyl compounds.

A carbonyl group is an organic functional group composed of a carbon atom double-bonded to an oxygen atom.[75] A compound containing such a carbon-oxygen double bond is called a carbonyl compound. Aldehydes and ketones are the simplest forms of carbonyl group, and these entities are commonly attached to larger carbon skeletons to make up a large group of organic molecules. Typical types of carbonyl compounds are presented in Table 4.1. Distinguished from the non-polar double bonds in alkenes, the difference between the electronegativity of carbon and oxygen induces the

bond's polarity, in which the electronegative oxygen draws electron density away from carbon. As a result, the carbonyl compounds are much more reactive than alkenes. The partially negative oxygen can react with electrophiles, including positive ions as Lewis acids, and the positively charged carbon can be attacked by nucleophiles as Lewis bases. The properties of carbonyls are closely tied to their electronic structures and geometric positioning. In the atomic orbitals of a carbonyl group, one pair of the oxygen lone pairs occupy the 2s orbital, while the other is located in the 2p orbital, both of which contribute to the polarity of the carbon-oxygen double bond.[76,77] Compared with alkenes, the double bond in carbonyls is shorter and the bond energy is higher.[78] Therefore, the reactivity of carbonyls should be ascribed to the induced polarity, and shorter bond length usually correlates to even larger polarity.[79]

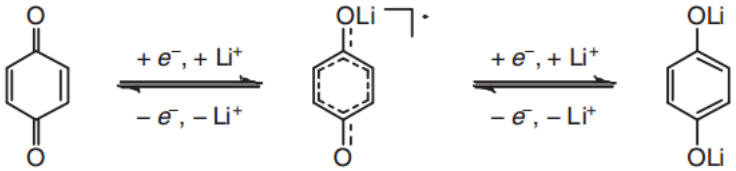

Figure 4.1: Reaction mechanism of a typical and quinone molecule with Li ions as the charge carriers.

Among different kinds of carbonyls, quinones are considered to be one of the most classes of organic redox species for energy storage systems. Specifically, quinones represent a family of organic molecules derived from aromatic compounds, and a typical molecular structure is shown in Figure 4.1. As the principal redox-active moieties within natural organic molecules, quinones play a key role in biological electron-transfer processes, such as photosynthesis and ATP synthesis.[80,81] As one of the most appealing types of organic redox species, their uses in the field of energy storage have been extensively researched. It has been found that the electron-transfer procedures of

quinones are strongly dependent on the solvent.[82] When the proton concentration is larger than the quinone concentration in protic electrolytes, the reduction of quinones proceeds in a single step involving a two-electron and two-proton process. If the proton concentration is not comparable with that of the quinone, however, the reaction is mainly interpreted as a two-electron reduction that generates a mixture of quinone anions with different protonated states. In this case, two reaction peaks can always be observed in the voltammetry curves. In the case of aprotic solvents, a quinone undergoes two successive one-electron reductions, forming the radical anion first and then the dianion.

Quinones in RFBs have received significant attention in the past decade.[83-85] The redox reactivity of carbonyls is based on the enolization process, in which positive charge carriers, such as H^+ or Li^+, bind to negatively charged oxygen. Therefore, quinones can be categorized into n-type electroactive organic molecules, accepting one or more electrons to form anions during the reduction process. In order to compete with the performance of conventional metal-based aqueous RFBs, rational functionalization is normally required to modify these electrochemically active molecules.[86] The design route and experimental approach vary based on requirements for solubility, redox potential, chemical stability, etc. In this section, I will introduce my works on tuning the properties of quinone compounds for both aqueous and non-aqueous RFBs.

4.2 A BIO-INSPIRED, HEAVY-METAL-FREE, DUAL-ELECTROLYTE LIQUID BATTERY BASED ON HYDROQUINONE*

4.2.1 Introduction

Flow batteries using species in fluid forms, which allows an independent control on power and energy, can play a critical role in efficient storage of sustainable energy from often intermittent sources. However, conventional flow batteries depend on redox-active metals and sometimes even precious-metal catalysts, which may inhibit wide-scale utilization limited by the material abundance and environmental issues. On the other hand, those redox reactions mainly take place in water, of which the potential window is limited to 1.23 V. To break the glass ceiling of output potential, some groups turn their attention to a new energy storage system called Li-RFB.[4,87] The flowable catholyte makes it possible to scale up power and energy, and Li anode can promote the working potential. Nevertheless, most of current researches adopt either metal complexes or halogens as redox-active species, both of which are faced with cost and environmental concerns. The direct use of Li anode also poses safety concerns.

Quinones are well-represented organic molecules in bio-logical electron transfer processes, such as photosynthesis and ATP synthesis. As one of the most important families of organic redox couples, their uses in the field of energy storage have been researched. Despite that quinone based solid state battery using aprotic electrolyte is limited in long term stability due to dissolution of active materials, the redox reaction of quinone in water has been proved to be highly stable in flow battery applications. Some groups already exploited quinones as electro-active species in flow batteries showing expected performance. Nevertheless, wider utilization of quinones is still faced with

* Y. Ding, G. Yu, A bio-inspired, heavy-metal-free, dual-electrolyte liquid battery towards sustainable energy storage, *Angew. Chem. Int. Ed.*, 2016, 128, 4850.
Y. D. carried out the experimental work and co-led the writing of the manuscript with Prof. Yu.

limitations. It is anticipated to build the battery with performance comparable with current technologies. In the meantime small molecules without complex synthesis method are preferred so as to increase specific capacity and lower the cost. To meet those requirements, we turned our attention to biomass-derived quinone molecules, and we designed the battery with Li^+ as mediators to break the potential ceiling of 1.23 V in water using proton mediator.

With the help of RDE and CV measurements, the redox chemistry of H_2BQ is investigated in a broad pH range. By tuning the concentration of protons, both the reaction process and the redox potential can be manipulated. In slightly basic environment, the solubility of H_2BQ can reach more than 1 M in water, which corresponds to 2 Faraday of charge per liter in the two-electron-involved reaction. The demonstrated energy density can reach 60 Wh L^{-1}, which is comparable or better than recent reports about liquid batteries. Distinguished from other complex quinone structures investigated before, the natural occurrences feature and mature production in industry as small molecule make H_2BQ appealing in commercial applications. On the other hand, as a discharged state of cathode-active species, H_2BQ can be coupled with graphite to build a full battery. Therefore, limitations including high cost of production, low output potential and dendrites issues faced in previous researches can be circumvented. All these features promise one novel type of green energy storage system for next generation.

4.2.2 Experimental

The battery assembly process has been introduced in previous chapters. For the chemical characterizations and battery test, galvanostatic charge/discharge test and CV test were performed on BioLogic VMP3 potentiostat system. The pH value was tested

using Oakton Ion 700. RDE measurements were conducted on BioLogic RRDE-3A rotating ring disk electrode. Both CV and RDE test use glassy carbon disk as working electrode, Ag/AgCl/3M NaCl as reference electrode and platinum as counter electrode. CV test was conducted at 25 mV s^{-1} in 1 mM H_2BQ and 0.2 M Li_2SO_4 water solution, and H_2SO_4 was added in advance to make the initial pH value of 1. Then 1 M LiOH solution was added drop by drop to tune the pH value. In RDE test, 1 mM H_2BQ and 0.2 M Li_2SO_4 in water was prepared with scan rate of 5 mV s^{-1} and rotation rate at 100, 225, 400, 625, 900, 1225, 1600 rpm respectively. In the Levich equation to get diffusion coefficient of redox species, i_{lim} is limiting current, n is the number of electrons transferred, F is Faraday constant (96485 C mol^{-1}), A is the surface area of electrode (0.07 cm^2), ω is angular rotation rate, ν is the kinetic viscosity (1.17×10^{-2} cm^2 s^{-1}), C is the bulk concentration (1×10^{-6} mol cm^{-3}). The reciprocal of current was plotted versus the reciprocal of the square root of the angular rotation rate at different overpotentials of 10, 15, 20, 25, 30, 35, 45 and 55 mV. The y intercept gives the reciprocal of i_k, which indicates the kinetic current at rotation rate of infinity. The plot of lgi_k versus overpotential was linearly fitted, and the x-intercept gives the log of exchange current i_0. Finally the reaction constant k_0 was calculated according to the equation $i_0=nFACk_0$. XRD patterns were recorded using Rigaku MiniFlex 600 and SEM images were taken using Hitachi S-5500 scanning electron microscope.

4.2.3 Results and Discussion

Here we propose directly using (H_2BQ) in water as catholyte for liquid battery. The chemical structure of H_2BQ features two hydroxyl groups bonded to a benzene ring in the para position. Different from its ortho isomer of catechol, in which the neighboring

hydroxyl groups will lead to the coupling of anionic forms, H_2BQ possesses a reversible two-electron-transfer reaction in water.

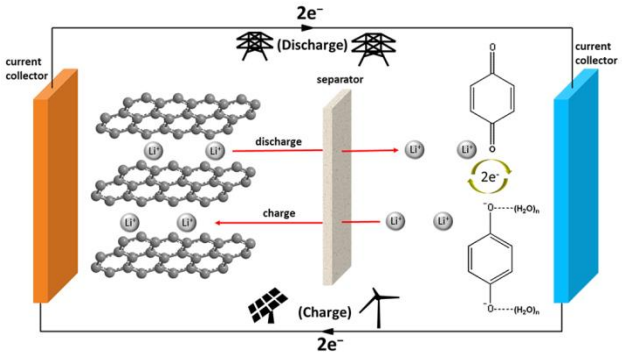

Figure 4.2: Working principle of the designed liquid battery with H_2BQ aqueous solution as catholyte and graphite in aprotic electrolyte as anode.

The working principle of this liquid battery is illustrated in Figure 4.2, in which the anode reaction is based on the intercalation and de-intercalation process of Li ions in graphite, and the cathode part is based on the redox reaction of H_2BQ with the transference of Li ions to balance the charge. As for the separator, a NASICON type Li-ion conducting solid membrane LATP functions to transfer Li ions and restrict crossover of redox species and electrolyte. Given two hydroxyl groups in H_2BQ are bonded to the aromatic ring in a para position, the feasibility of the redox reaction should be related to the reorganization of the conjugated double bond.

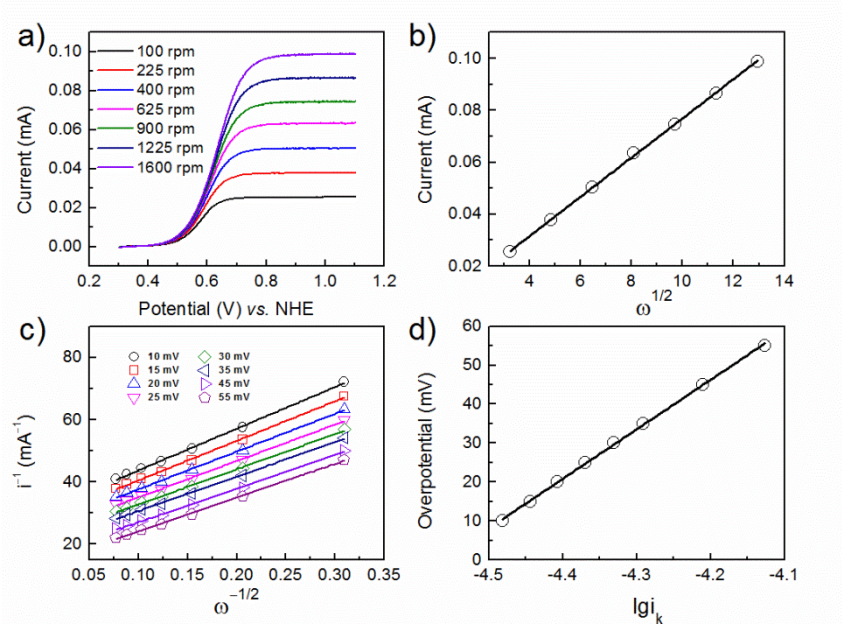

Figure 4.3: (a) RDE measurements of 1 mM H_2BQ in 0.2 M Li_2SO_4 solution at rotation rates from 100 rpm to 1600 rpm with a scan rate of 5 mV s^{-1} on a glassy carbon electrode. (b) Levich plot of limiting current vs. square root of rotation rates ($\omega^{1/2}$). (c) Koutecky-Levich plots derived from different overpotentials. (d) Fit of Butler-volmer equation derived from (c) at different overpotentials.

RDE test was firstly carried out to explore the electrochemistry of H_2BQ (Figure 4.3). In the potential range between 0.2 V and 1.1 V (vs. SHE), a flat limiting current plateau corresponds to a one-step two-electron-transfer reaction, which correlates well with published literature. The redox potential of H_2BQ can also be estimated from the half-wave potential, which is ~ 0.6 V and this value is comparable with iodine/iodide, but the abundance and environmental-friendliness of H_2BQ are more prominent. RDE measurement at different rates yields limiting current controlled by mass transport, from which the diffusion coefficient (D) of H_2BQ can be obtained using Levich equation:

$$i_{lim}=0.62\times nFAD^{2/3}\,\omega^{1/2}\,\nu^{-1/6}\,C$$

in which i_{lim} is limiting current, n is the number of electrons transferred, F is Faraday constant, A is the surface area of electrode, ω is angular rotation rate, ν is the kinetic viscosity, C is the bulk concentration. The calculated D (8.8×10^{-6} cm^2 s^{-1}) is similar to those of redox couples in aqueous flow batteries, but several orders of magnitude larger than that of Li ion in solid state Li-ion batteries. Koutecky-Levich analysis indicates that the redox reaction is controlled by both diffusion and kinetic effect, and the kinetic current i_k without mass transport limitation can be obtained by extrapolating rotation rate to infinity according to Koutecky-Levich equation (Figure 4.3c).

$$1/i=1/i_k +1/(0.62\times nFAD^{2/3}\ \omega^{1/2}\ \nu^{-1/6}C$$

The exchange current (i_0) can be obtained by fitting Butler-Volmer equation at overpotential of zero (Figure 4.3d), and the reaction rate constant (k_0) was calculated to be 2.0×10^{-3} cm s^{-1} according to the equation:

$$i_0=nFACk_0$$

This rate constant is larger than most of the redox species in commercial RFBs, such as VO_2^+/VO^{2+}, Fe^{3+}/Fe^{2+} and Br_2/Br^-, implying that voltage loss due to activation polarization of H_2BQ-based liquid battery is mitigated greatly. In light of the structure of H_2BQ molecule, the high rate should be attributed to the outer sphere electron transfer process, with small energy needed to reorganize the aromatic π orbital system.

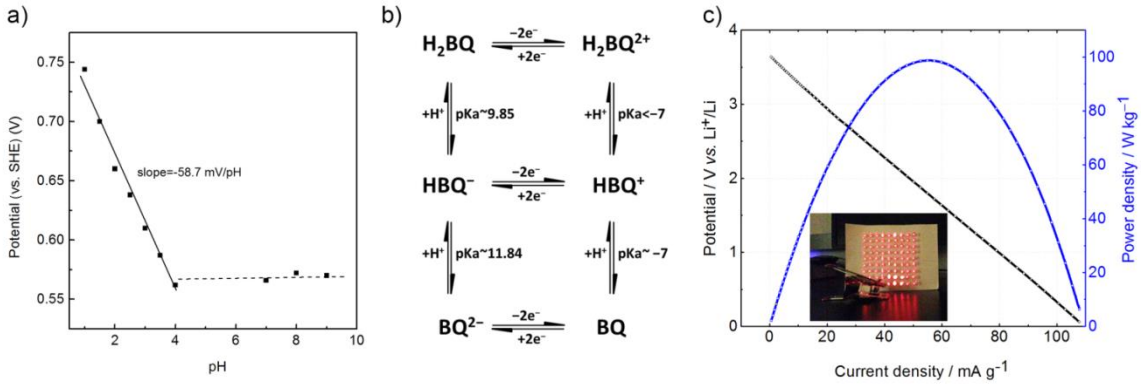

Figure 4.4: (a) Potential ($E_{1/2}$) vs. pH value for 1 mM H_2BQ in 0.2 M Li_2SO_4 solution at scan rate of 25 mV s^{-1}. (b) Redox reaction and proton-transfer reactions of H2BQ. (c) Polarization curve of the full liquid cell and the inserted picture shows the demo to power 81 LED bulbs.

To gain a better understanding of the electrochemistry of H_2BQ, CV tests were conducted in a broad pH range between 1 and 9. The pH-dependence of CV curves is shown in Figure 4.4a and increasing pH can shift the potential of the proton-involved reaction to more negative values. But when the concentration of proton is reduced greatly, the redox potential becomes pH-independent. This trend can be explained clearly by manipulating Nernst equation of the redox reaction.[88]

$$BQ + mH^+ + ne^- \rightarrow H_mBQ^{m-n}$$

$$E=E^o-(RT/nF)\ln([H_mBQ^{m-n}]/([BQ][H^+]^m)$$

The redox potential for an m H^+, n e^- involved reaction should change –(m/n)59 mV/pH at temperature of 25 °C. In the pH range of 1−4, the reduced species is in the fully protonated state, thus it undergoes a 2 H^+, 2 e^- process and the theoretical slope should be −59 mV/pH, corresponding well with the experimentally fitted value of −58.7 mV/pH in Figure 4.4a. When the concentration of protons decreases greatly, the reduced species may exist in the form of deprotonated state, and the redox potential will be pH independent, as illustrated in the region of pH above 7 (Figure 4.4a). This result agrees

with published reports, and we can further summarize the possible redox reaction and proton-transfer process of H_2BQ in Figure 4.4b.[89] It is clear that this is a two-electron-transfer reaction, but the reduced species may be a mixture of BQ^{2-}, protonated anion HBQ^{-} and hydroquinone H_2BQ with different distributions at different pH values. In acidic environment, most of the distribution will be fully protonated H_2BQ, thus breaking of O-H bond in the redox reaction process should require more activation energy. While in basic condition, the constituent will mainly contain anion BQ^{2-}, of which the redox reaction is less complex and the redox potential is pH-independent. As a result, to maximize the solubility of redox species, decrease the complexity of the redox reaction, and maintain the stability of solid electrolyte, we tune the pH value to 9 by adding LiOH solution. With H_2BQ in weak basic environment as catholyte, the reduced state can couple with graphite anode to construct a full cell. Polarization curve in Figure 4.4c exhibits the potential−current and power−current response. The maximum power density of the full cell can reach ~100 W kg^{-1} based on the total weight of catholyte solution at current density of 58 mA g^{-1} at room temperature. This power density is comparable to that of other reported RFBs and can be improved further by exploiting advanced solid electrolyte in view of the fast kinetics and diffusion coefficient of H_2BQ.

To further test the feasibility of H_2BQ based liquid battery, the catholyte was subjected to electrochemical measurements in a cell format using graphite anode. In this study, a home-made cell was adopted to demonstrate the performance, which is composed of a cathode part with titanium foil coated with activated carbon as current collector, H_2BQ and Li salt in water as catholyte, a NASICON-type LATP membrane as separator, and graphite suspension casted on copper mesh as anode.

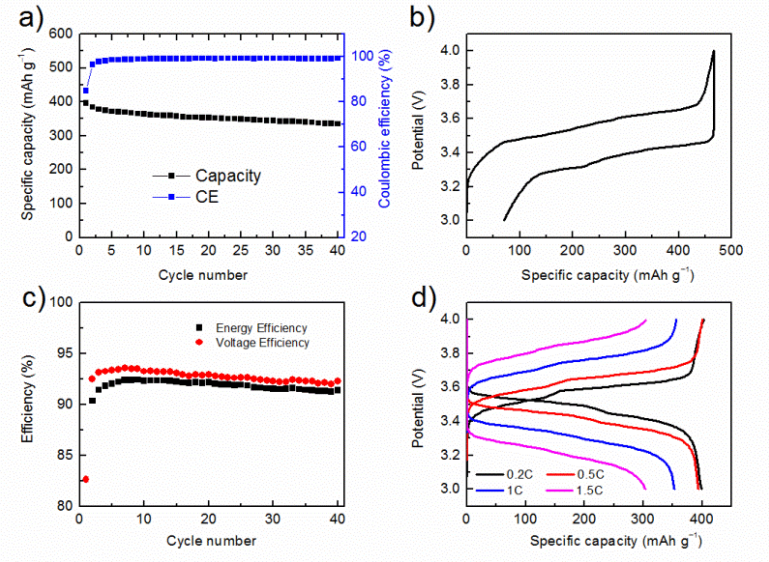

Figure 4.5: (a) Cycling performance of the full cell at 0.4 C. (b) Charge-discharge curve for the first cycle. (c) Corresponding energy and voltage efficiency. (d) Rate performance of the full cell.

The discharge potential of the full cell maintains at 3.4 V, as shown in the voltage profile (Figure 4.5b), which is much larger than conventional aqueous flow batteries restricted by the electrolysis of water (1.23 V). This result also correlates well with half-cell data, in which the discharge potential of H_2BQ maintains ~3.5 V and the charge potential of graphite is ~0.1 V. In such a full cell, crossover of active species can be limited to the minimum extent confirmed by the stabilized CE of over 99%. In the cycling test, the stabilized VE is ~ 93% and EE is ~92%, both of which greatly exceed those of the reported non-aqueous flow batteries (EE~ 20−50%).[90] Cycling performance in Figure 4.5a shows ~99.7% retention per cycle. Rate performance in Figure 4.5d indicates that 98.7%, 88.6% and 76.1% of the capacity can be retained when the tested current rates changed from 0.2 C to 0.5 C, 1C and 1.5 C with CE at all rates maintaining ~100%. The untapped capacity at high rates is attributed to the ohmic polarization of solid electrolyte, and the rate capability can be further enhanced with development of

advanced Li-ion conductors. The excellent rate performance is in accordance with the high power density shown in polarization curve. Long-term stability of this full cell was also examined. XRD patterns and SEM images of pristine separator and the one after 40 cycles show almost the same crystalline structure and porous morphology (Figure 4.6, 4.7), indicating the good stability of LATP in the weak basic environment.

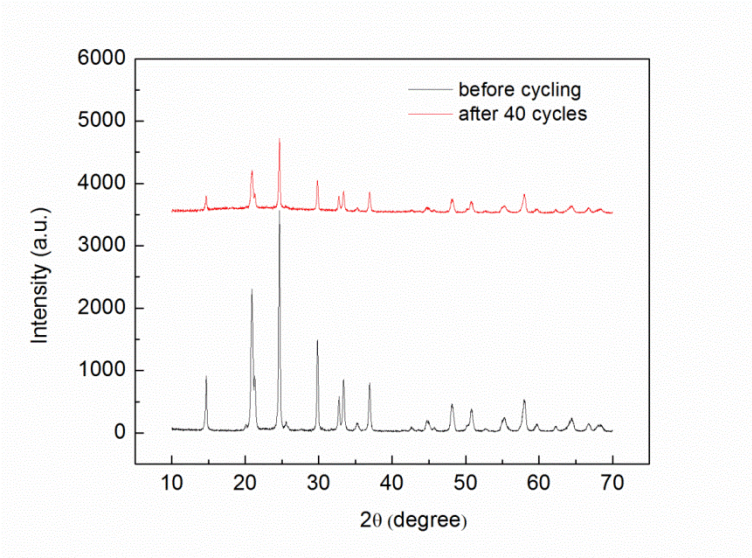

Figure 4.6: XRD patterns of fresh separator and the separator after 40 cycles of the full cell.

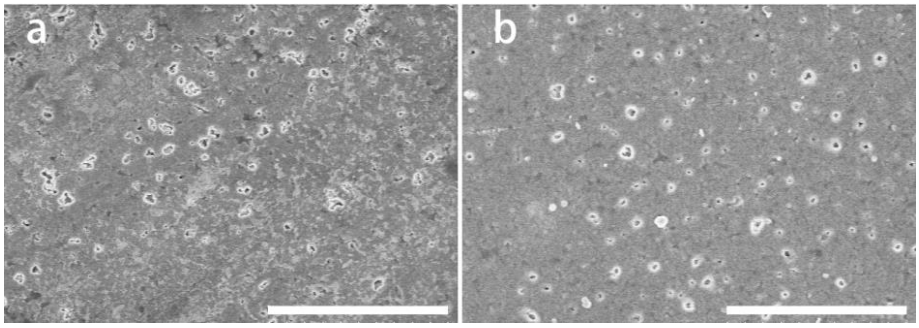

Figure 4.7: SEM images of fresh separator (a) and the separator after 40 cycles (b) of the full cell. Scale bar is 5 μm.

Inspired by the pivotal role of quinones in nature, a heavy-metal-free, dual electrolyte liquid battery is designed. By directly using H_2BQ in water as catholyte and graphite as anode, specific discharge capacity of 395 mAh g^{-1} is obtained with the working potential of 3.4 V. As one of the simplest forms of organic redox species, H_2BQ can be extracted directly from living organisms, and the outer sphere electron transfer reaction with small activation energy to reorganize the aromatic π bond contributes to high reaction rate constant, therefore all these features promise a cost-effective energy storage system that may output superior performance without environmental disturbance. As the development of flow batteries relies on the development of redox-active materials, quinone-represented organic redox species provide much more freedom to design metal-free batteries toward sustainable energy storage. The tunable properties can be realized by electrolyte solvent selection. Additionally the structure diversity of organic materials allows the tailoring of solubility, electrochemical activity and redox potential by functionalization with certain groups. For example, when the concentration of H_2BQ reaches more than 0.5 M, CE for the first cycle drops obviously due to low solubility of BQ, and this concern can be alleviated by functionalizing H_2BQ with hydrophilic groups such as sulfonic group to improve solubility, so as to expect higher energy density. Nowadays the performance of metal-free flow battery is limited in the anode part, and selection of organic based anode-active materials with low potential can lead to the construction of high-performance all-organic flow batteries.[91] Moreover, the graphite anode can even be replaced with anode suspensions like Si, which may stretch the research boundaries of different kinds of batteries, and broaden the extent of novel energy storage devices with new chemistry.[92] Generally speaking, by designing such a battery mainly using C, H and O as building blocks to fabricate redox species, the rapid growth and moving frontiers of atom economy in green chemistry can be extended to the field of

energy storage. Thus this new-concept battery is promising to meet the system capital cost target of $150 per kW h set by US Department of Energy.[93]

4.3 Hydrotropic Solubilization of Quinone for High-Energy Hybrid Ion RFBs*

4.3.1 Introduction

Energy is the essential factor in the development of modern society. Modern economies eagerly await a solution for meeting the rapidly growing demand for energy in a sustainable, cost-effective, and environmentally friendly manner.[94] Considering the intermittent nature of renewable energy, batteries play a critical role in effective round-the-clock delivery of the electricity generated from such sources. Amid different kinds of energy storage systems, RFBs, which store chemical components in liquids and allow a decoupled control on energy and power, represent a promising technology toward stationary energy storage. It is noted that the widespread implementation of traditional RFBs is mainly hindered by the use of electro-active metals with low abundance and environmental concerns. Recently, organic redox species have emerged as novel electrode materials for RFB applications. In addition to the advantages of potentially low cost and ease of scalability, the structural diversity of organic molecules allows for tailoring of their chemical and physical properties. Nevertheless, current organic RFBs fall short of meeting the energy density requirements due to insufficient solubility of redox molecules. Furthermore, the working voltage is not high enough since anode-active molecules with low redox potential are rare and currently remain limited to insoluble lithium salts. Therefore, realizing the vision of constructing a high performance organic RFB necessitates the selection and modification of both a catholyte and an anolyte with high concentration and suitable redox potentials.

---

* Y. Ding, C. Zhang, L. Zhang, H. Wei, Y. Li, J. B. Goodenough, G. Yu, Hydrotropic solubilization enabled high-energy hybrid ion redox flow battery, in revision.
Y. D. carried out the experimental work and participated in the preparation of the manuscript.

Similar to RFB applications, solubility is also a critical parameter in pharmaceutical research.[95] Since oral ingestion is the most commonly employed route of drug delivery, solubility plays an important role in ensuring dosages meet bioavailability requirements. To get a desired pharmacological response, a specific concentration of drugs in the body's internal circulation systems must be achieved. Thus, low aqueous solubility is the primary barrier during formulation development of new chemical entities and generic product development. Currently, various techniques are used to improve the solubility of drugs in water, including chemical modification, solid dispersion, micronization, micellar solubilization and so on.[96] Achieving practical formulations requires rational selection of solubility enhancement methods depending on the characteristics of the drugs.

Inspired by the fruitful results from pharmaceutical research, a high-concentration quinone-based RFB using hydrotropic solubilization effect is investigated. As the principal redox-active moieties in bioelectrochemical systems, quinones represent an appealing class of biomimetic electro-active materials for RFB applications. Historically, chemical functionalization with hydrophilic groups is normally required, especially for hydrophobic polycyclic quinones, given their insufficient solubility in water. In this chapter, the solubility of hydroquinone (H_2BQ) in water can be improved from about 0.5 M to 1.4 M when 4 M urea was added as a hydrotropic agent. Compared with complex molecular engineering methods, this hydrotropic method is facile and cost-effective, and the added agents can be recycled in the long term even after the battery dies. In view of the high solubility and two-electron-transfer reaction of H_2BQ, the theoretical volumetric capacity can reach 50 Ah L^{-1}, which rivals most previously reported aqueous organic RFBs.[97] Despite the mass of the hydrotropic agent, twice the gravimetric capacity of the pristine catholyte can be achieved. Furthermore a combined experimental and

computational study was conducted to elucidate the nature and mechanisms of the hydrotropic process. In addition to concentration enhancement, the working voltage should also be broadened to increase the energy density of the RFB. Herein, several deep eutectic solvents (DESs) with low redox potentials were prepared as anolytes. Compared to conventional anode-active redox species, Al or Zn-based DESs possess a lower voltage, much higher concentration, and a multi-electron transfer process, all of which are beneficial to increasing the energy density of flow battery systems.[98-100] More importantly, the dendrite issue faced in previous works using an alkaline metal anode can be circumvented.[101] The above-mentioned advantages show the promise of this next generation of environmentally benign and cost-effective RFBs with high safety and large energy density.

4.3.2 Experimental

Preparation of Al-based DES: LiCl and $AlCl_3$ were dried at 100 ^oC in vacuum oven for 3 days, and urea was dried at 60 ^oC in vacuum oven for 1 day. The Al-based DES was prepared by mixing $AlCl_3$ with urea ($AlCl_3$:urea=1.3:1 (mole ratio)) in a vial under stirring at 60 ^oC in a glove box filled with argon. Then 1,2-dichloroethane (DCE) was added to the as-prepared Al-based DES (DCE:Al-based DES=1:2 (volume ratio)) to decrease the viscosity. The concentration of Al-based DES based on the content of Al can reach 5.6 M. In battery test, LiCl will be added into the prepared Al-based DES/DCE as charge carrier with the concentration of 0.5 M.

Preparation of Zn-based DES: Similarly, the Zn-based DES was prepared by mixing $ZnCl_2$ with choline chloride (ChCl) ($ZnCl_2$:ChCl=2:1 (mole ratio)) in a vial under stirring at 60 ^oC for 12 hours in air. Then ethylene glycol (EG) was added to the as-prepared Zn-based DES ($ZnCl_2$:ChCl:EG=2:1:9 (mole ratio)) to decrease the viscosity.

The concentration of Zn-based DES based on the content of Zn can reach 4.0 M. In battery test, LiCl will be added into the prepared Zn-based DES/DCE as charge carrier with the concentration of 0.5 M.

The assembly of the home-made battery using LATP membranes has been introduced in previous chapters. Electrochemical tests were performed on a BioLogic VMP3 potentiostat system. The CV measurements of deep eutectic solvents were conducted using Al or Zn foil as the reference electrode, platinum wire as the counter electrode and glassy carbon as the working electrode. In CV tests of H_2BQ solution with and without hydrotropic agent, Ag/AgCl/1.0 mol/kg KCl was adopted as the reference electrode, platinum wire as the counter electrode, and glassy carbon as the working electrode. In the EIS measurement on BioLogic VMP3 potentiostat system, two-electrode cell was built using glassy carbon electrodes immersed into the electrolyte. RDE measurements were conducted on BioLogic RRDE-3A rotating ring disk electrode with Ag/AgCl/1.0 mol/kg KCl as the reference electrode, platinum wire as the counter electrode, and glassy carbon as the working electrode.

The UV-vis spectra of samples were recorded using a UV-vis spectrometer (Evolution 300, Thermo Scientific) from 200 to 400 nm. The FTIR spectra were obtained using a Nicolet iS5 FT-IR spectrometer in the spectral area 400–4,000 cm^{-1}. ^{1}H and ^{13}C NMR measurements were carried out with a Varian Gemini at 400 MHz. In NMR test, all the organic samples were dissolved in D_2O solvent, and the Al-DES was dissolved in dichloromethane-d_2. The conductivity measurement was based on the EIS test using two platinum foil electrodes immersed in 1M KOH solution with different concentrations of urea and H_2BQ. The Raman spectra were recorded on a Micro-Raman Spectrometer (Witec, Alpha 300) under 488 nm. The viscosity was tested using a rheometer (AR-2000EX, TA instrument) attached to a 25 mm parallel upper plate and a peltier bottom

plate at an angular velocity of 35 rad s^{-1}. SEM (scanning electron microscope) images were taken using Hitachi S-5500.

Simulation details: All MD simulations were performed using the AMBER 10 suite of programs. Water was described with the SPC/E model. The parameters of the force fields for urea were developed by Duffy et al. The AMBER99 force field force field was used to calculate van der Waals and electrostatic of H_2BQ. The charge distributions on all atoms in H_2BQ were obtained using the RESP-fit method based on B3LYP/cc-pVTZ density functional theory (DFT) calculations. To study the effects of urea on the solution of H_2BQ, we have carried out classical MD simulations in three solvent systems: H_2BQ (0.53M) system consisted of 50 H_2BQ and 5002 water molecules; H_2BQ (0.75M) and urea (0.5M) system consisted of 70 H_2BQ, 50 urea and 5017 water molecules; H_2BQ (1.4M) and urea (4M) system consisted of 125 H_2BQ, 375 urea and 5071 water molecules. Cuboid boxes were created with water and solute molecules evenly distributed in the initial configuration. The resulting final cuboid boxes for three systems are approximately 60 × 59 × 58, 58 × 69 × 58, 62 × 72 × 71 $Å^3$, respectively. All of these systems were further extended by using the periodic boundary condition. The SHAKE algorithm was used to constrain all bonds involving hydrogens. A cutoff of 10.0 Å was applied for nonbonding interactions. The Particle Mesh Ewald method was applied to treat long-range electrostatic interactions. To obtain a reasonable initial structure, an NPT (number, pressure, temperature) ensemble calculation was performed first. In this process, a 20 ps MD simulation was first conducted to heat the system from 0 to 360 K, followed by a 200 ps equilibration at 360 K and 1 atm. Next, the system was cooled to 300 K by another 20 ps MD simulation followed by a 1 ns equilibration at 300 K and 1 atm. Finally, 10 ns production runs were performed at 300 K and then used for the data analysis, with the data being collected every 0.5 ps.

4.3.3 Results and Discussion

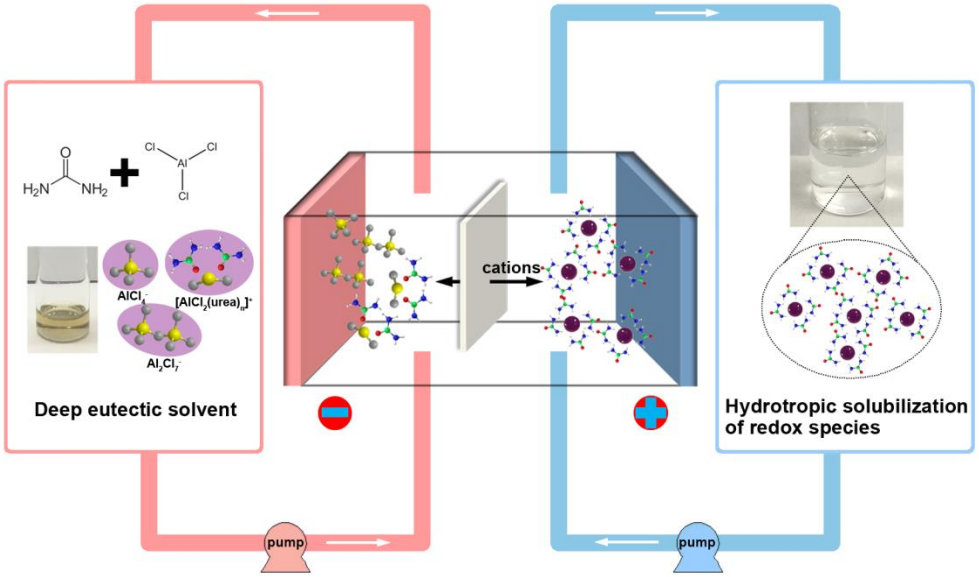

Figure 4.8: Working principle of the hydrotropic solubilization enabled hybrid ion RFB.

Figure 4.8 presents the hybrid ion RFB design employing Al-based DES as anolyte and hydrotropic solubilization-enhanced quinone-based catholyte. DES is a kind of eutectic mixture of Lewis acids and bases incor-porating several ionic components.[102] Typically, a DES contains asymmetric ions with delocalized charge, which results in reduced lattice energy and hence depression of freezing points. Although Fe-based DES has been report-ed for RFBs, the high redox potential of Fe^{2+}/Fe^{3+} is not suitable for anolyte.[103] Given the key features such as high concentration, low cost, potential bio-degradability, minimal environmental footprint, low redox potential, and multi-electron transfer processes, Al- and Zn-based DESs were selected as anolytes for the RFB. DESs can be specifically classified depending on the nature of their complexing agents. In our study, the Al-based eutectic is formed using a dispropor-tionation process between $AlCl_3$ and the hydrogen bond donor of urea.[104] In comparison, the Zn-based DES is pre-pared

by mixing choline chloride, in which a quaternary ammonium cation functions as the cationic component and chloride as a Lewis base, with $ZnCl_2$ as a Lewis acid. The obtained DESs are presented in Figure 4.9, and the concentration of Al- and Zn-based DES can reach 5.6 M and 4.0 M, respectively, both of which exceed that of most reported electrode materials for anolytes.

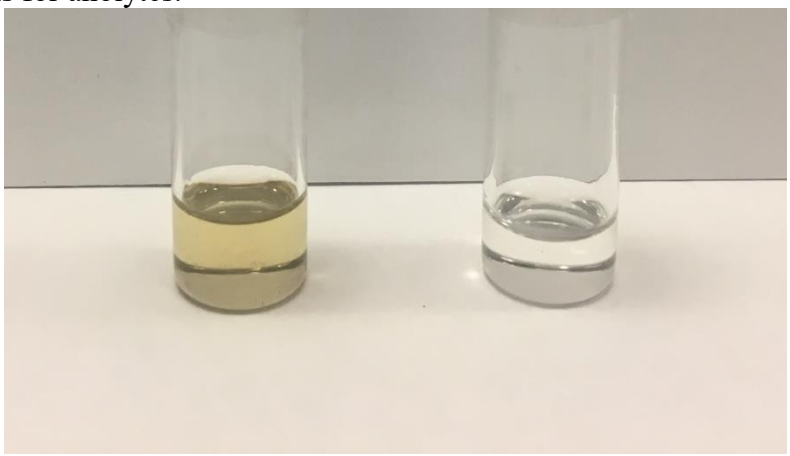

Figure 4.9: Photograph of as-prepared Al-based DES (left) and Zn-based DES (right).

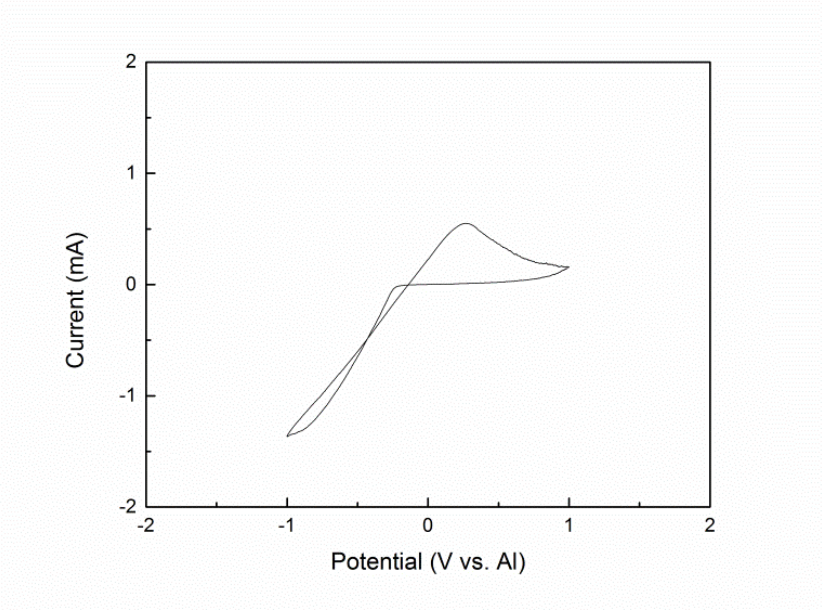

Figure 4.10: CV curve of Al-based DES at a scan rate of 50 mV/s.

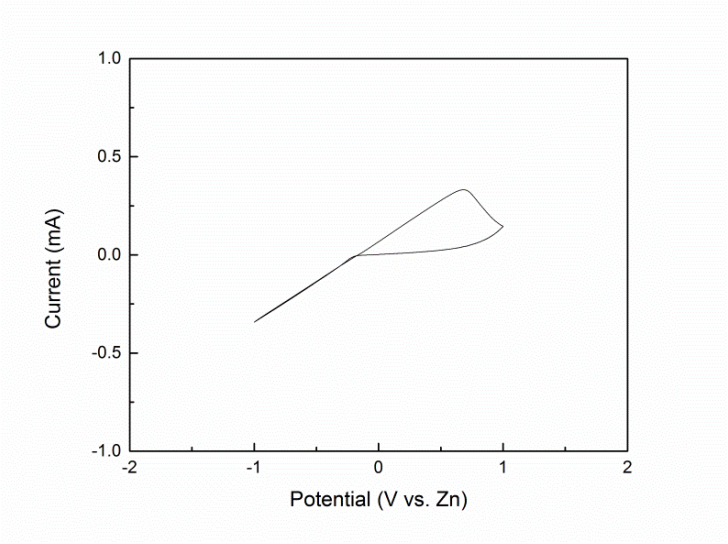

Figure 4.11: CV curve of Zn-based DES at a scan rate of 50 mV/s.

To demonstrate the reversibility of DES-based anolytes, CV measurements were conducted in a three-electrode system with glassy carbon as the working electrode, Al or Zn metal as the reference electrode and platinum wire as the counter electrode, as shown in Figure 4.10 and 4.11. In general, the deposition and stripping of metals can be clearly delineated, which corresponds to the reversible redox reaction of both Al- and Zn-based anolyte. Notably, the current intensity of Al-based DES is larger and the polarization is less compared to Zn-based anolyte, which should be attributed to the effect of concentration, reaction kinetics, and viscosity. As discussed above, the speciation mechanism of Al-based DES has been investigated, and it consists of cations and anions via a disproportionation process:

$$2AlCl_3 + 2(urea) \rightarrow [AlCl_2 \cdot (urea)_2]^+ + [AlCl_4]^-$$

where both anodic and cathodic metal complexes are produced to ensure conservation of mass and charge. Upon adding more $AlCl_3$, $[Al_2Cl_7]^-$ would be formed from bonding to $[AlCl_4]^-$. Therefore, there are mainly two pathways in aluminum deposition:

$$4[Al_2Cl_7]^- + 3e^- \rightarrow Al + 7[AlCl_4]^-$$

$$2[AlCl_2 \cdot (urea)_2]^+ + 3e^- \rightarrow Al + [AlCl_4]^- + 4(urea)$$

The mass transport is primarily governed by electromigration in the deposition process, during which cationic species migrate through the electrolyte to the working electrode. Meanwhile, anodic species migrate in the opposite direction. Consequently, the latter reaction is considered to be dominant in aluminum deposition. As for the speciation of the Zn-based anolyte, a series of complex zinc anions are generated, including $[ZnCl_3]^-$, $[Zn_2Cl_5]^-$, $[Zn_3Cl_7]^-$ as well as a number of higher clusters at very low intensities. The content of anion complexes depends on the ratio of Lewis acids and bases, and stripping/deposition of Zn involves production and consumption of certain anodic species.

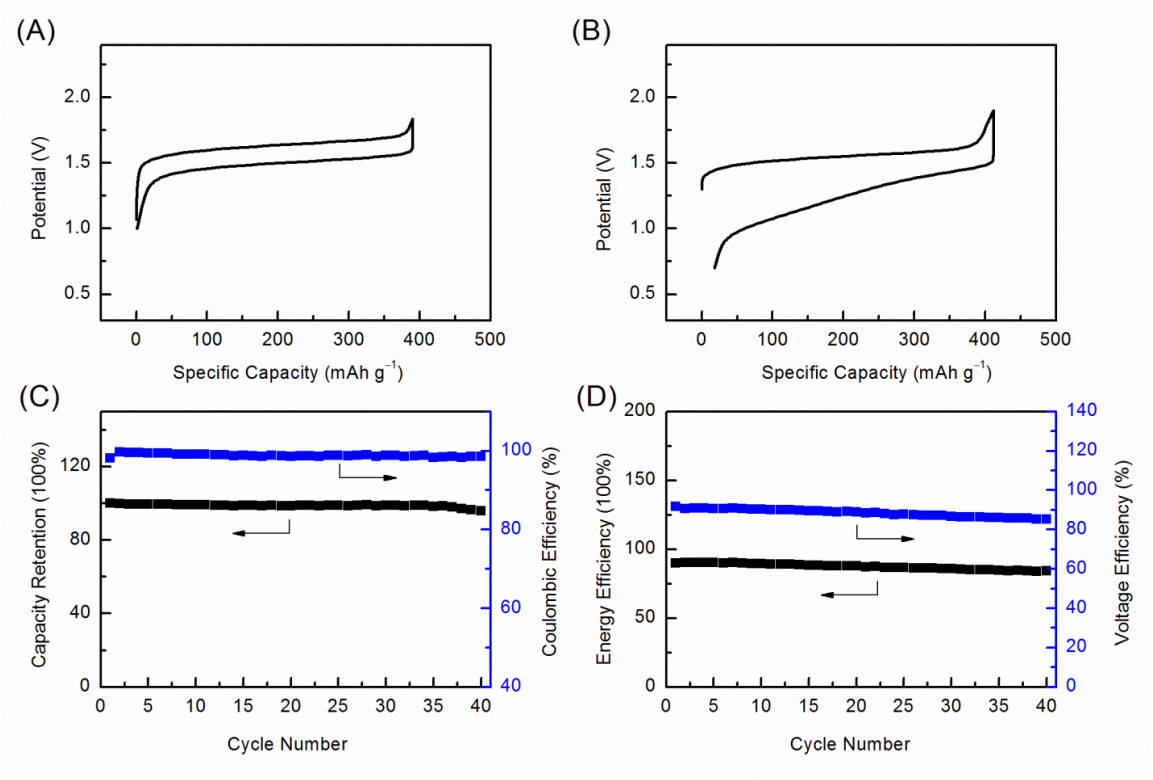

Figure 4.12: Performance of the hybrid ion RFB. (A) Charge-discharge profile of the flow battery at 100 μA cm^{-2} with Al-based DES as anolyte, and the catholyte containing 0.1 M H_2BQ. (B) Charge-discharge profile of the flow battery at 60 μA cm^{-2} with Zn-based DES as anolyte, and the catholyte containing 0.1 M H_2BQ. (C and D) Cycling stability and efficiency of the flow battery at 100 μA cm^{-2} with Al-based DES as anolyte, and the catholyte contains 0.1 M H_2BQ.

To further test the feasibility of DES-based anolytes, a home-made RFB was built using H_2BQ solution as the catholyte and a NASICON-type solid state electrolyte as the separator. Figure 4.12 shows the electrochemical performance of the H_2BQ-based RFB paired with a deep eutectic anolyte. The working voltage maintains around 1.5 V with Al-based anolyte, and it can still reach 1.3 V using a Zn-based DES, both of which are higher than conventional aqueous RFBs. It is noted that more obvious polarization occurs when using a Zn-based anolyte, most likely as a result of high viscosity and slow reaction

kinetics, and this also correlates with the CV curves. As displayed in Figure 4.12C and Figure 4.12D, the cycling stability of the Al-based hybrid ion battery is outstanding, with capacity retention of 99.90% per cycle. Moreover, the stabilized Coulombic efficiency is ~ 99% and the energy efficiency is ca. 89%, both of which remarkably outperform the reported organic RFBs. Although the current density is not comparable with aqueous RFBs limited by the high viscosity of DESs and the low conductivity of membranes, it can still compete with non-aqueous RFBs, and further improvement can be expected with the development of advanced membranes. Moreover, the Al-based anolyte after battery cycling shows almost the same ^{1}H NMR signals as that before battery cycling without any water signals detected (Figure 4.13), which further attests the reliability of such a hybrid aqueous/non-aqueous design based on NASICON-type membranes. To prove the broad applicability of the deep eutectic system, a galvanostatic charge-discharge measurement was also conducted using a Zn-based anolyte (Figure 4.14), but the demonstrated stability and power density has yet to be improved. In light of Stokes' law, lower solvent viscosity can give rise to higher ionic conductivity in electrolytes given the same supporting salt, hence improved battery performance can be expected by further rational screening of hydrogen bond donors in the formation of less viscous DESs.[105]

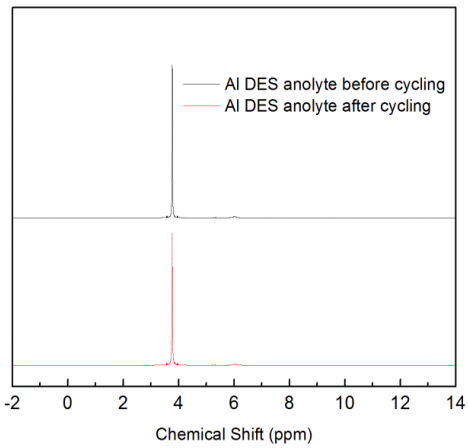

Figure 4.13: ^{1}H NMR spectra of the Al-based DES before and after battery cycling.

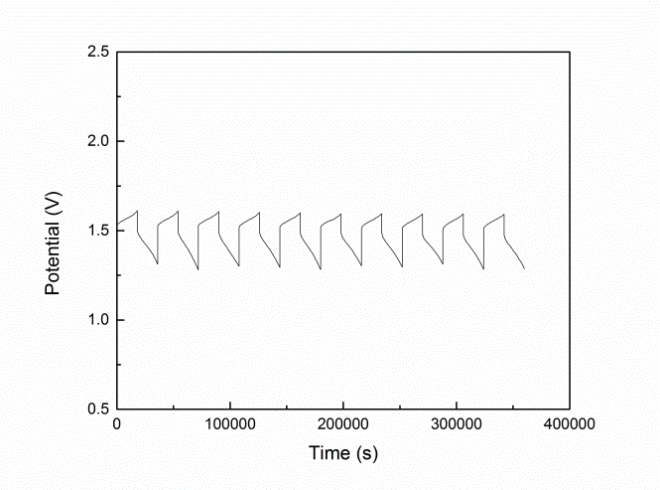

Figure 4.14: Charge-discharge profiles of the Zn-based RFB. The battery was cycled at 40 μA cm^{-2} with Zn-based DES as anolyte, and the catholyte contains 0.1 M H_2BQ.

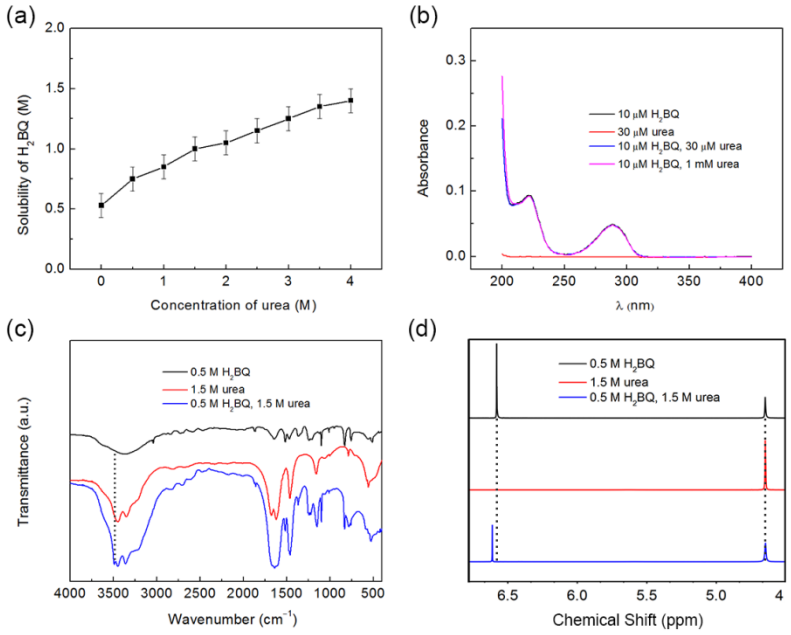

Figure 4.15: Characterization of hydrotrope-enhanced H_2BQ solution. (A) Solubility of H_2BQ in different concentrations of urea. (B) UV-vis spectra of H_2BQ, urea and the H_2BQ solution with various concentrations of urea. (C) FTIR spectra of H_2BQ, urea and urea-enhanced H_2BQ solution. (D) ^1H NMR spectra of H_2BQ, urea and urea-enhanced H_2BQ solution.

Since the energy density of RFBs is dictated by the concentration of redox-active substances, the solubility of H_2BQ in the cathode part is the bottleneck considering the highly concentrated eutectic anolyte. Drawing inspiration from the solubility enhancement techniques explored in the pharmaceutical industry, notably increased solubility of H_2BQ is achieved via hydrotropic solubilization. The term "hydrotropy" was coined to describe a molecule possessing the ability to augment the solubility of sparingly soluble organic compounds in water.[106] The mechanism of solubilization still remains elusive, and a typical hydrotropic agent may interact with a less soluble molecule via π-π stacking or dipole-dipole attraction.[107] Distinguished from surfactants, hydrotropes contain very small hydrophobic moieties, and a variety of molecules have been used as hydrotropic agents to improve the solubility of drugs. In selecting the suitable hydrotrope,

cost, mass, and electrochemical stability should be taken into account. After rational screening, urea was selected as the hydrotropic agent considering its low cost, small molecular weight and high stability compared with other agents, such as caffeine and nicotinamide.

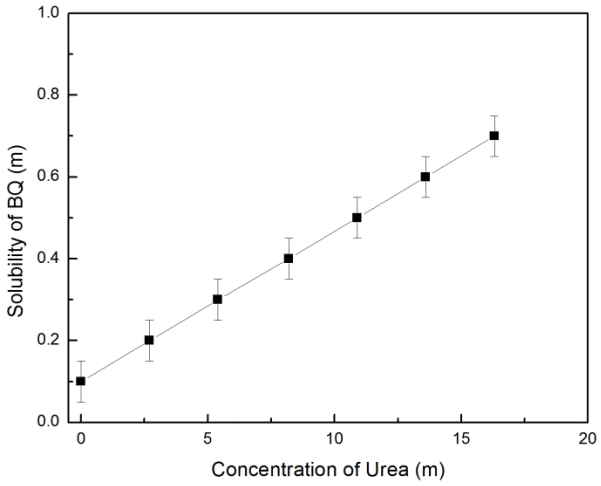

Figure 4.16: Solubility of BQ under different concentrations of urea.

Figure 4.15a shows the progressively increased solubility of H_2BQ in the presence of the hydrotropic agent, and 4 M urea can lead to a nearly three-fold increase in solubility. Even taking into account the total mass, this solubility enhancement can still give rise to more than doubled gravimetric capacity. Meanwhile, the hydrotropic effect of urea on benzoquinone (BQ) is investigated as well (Figure 4.16). The solubility of BQ in water can be enhanced as well with the help of urea. The bifunctional effect of urea on both H_2BQ and BQ makes it possible to build a higher energy RFB. Notably, it is interesting to find that the hydrotropic effect of urea can be further extended to a variety of organic redox species, including anthraquinone-2-sulfonic acid sodium salt monohydrate (AQS), 1,2-dihydroxybenzene (1,2-DHB), and riboflavin 5'-

monophosphate sodium salt hydrate (RFMP) (Figure 4.17, 4.18, 4.19). All these merits promise the next-generation of high energy organic RFBs enabled by the hydrotropic method.

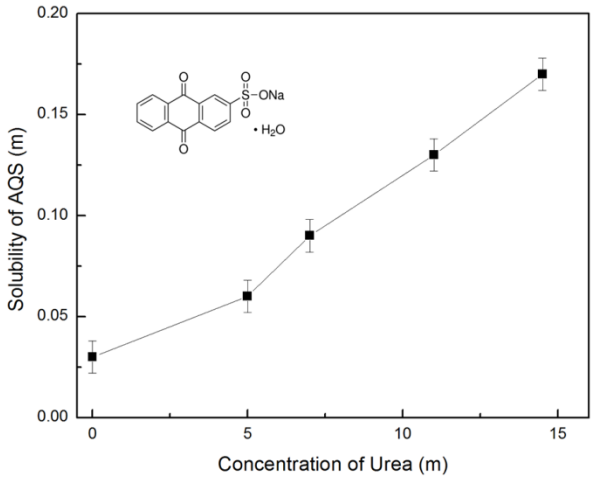

Figure 4.17: Solubility of AQS under different concentrations of urea.

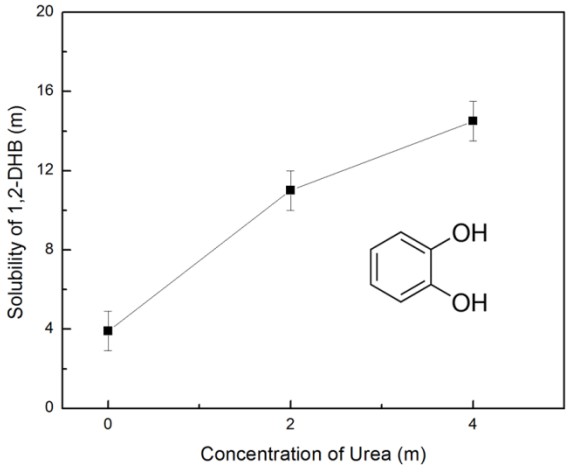

Figure 4.18: Solubility of 1,2-DHB under different concentrations of urea.

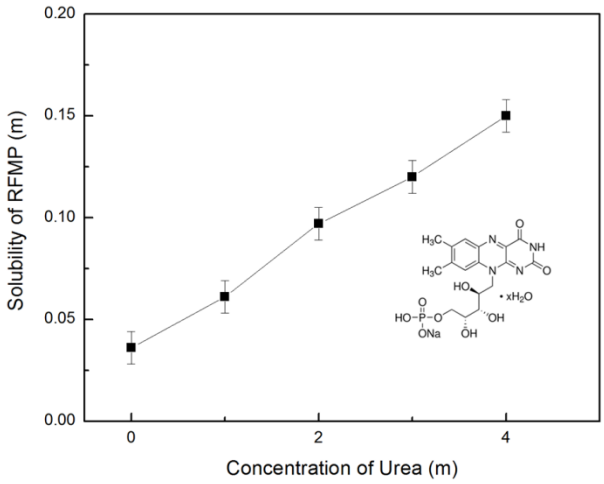

Figure 4.19: Solubility of RFMP under different concentrations of urea.

To gain a deeper understanding of the hydrotropic mechanism, a comprehensive study encompassing detailed chemical characterization and advanced computational modeling was conducted. UV-vis measurements were first performed to study the possible spectroscopic changes of H_2BQ in the presence of urea. As shown in Figure 4.15b, the UV-vis absorptions at 288 nm and 245.5 nm correspond to H_2BQ and dissociated H_2BQ separately, but urea exhibits no light absorptions in this range of wave-lengths. In UV-vis spectra, any complex formation, indicated by the generation of new chromophores, would lead to the appearance or mergence of peaks. When comparing the absorptions of H_2BQ in various hydrotrope concentrations, no variation of spectral band position was observed, suggesting that no strong interactions between H_2BQ and urea exist to form complexes in this system. Moreover, the almost overlapped spectra indicate that no parasitic side reactions took place to change the activity of H_2BQ. Similar conclusions can also be derived on the hydrotropic solution of BQ (Figure 4.20), and no variations of BQ absorptions can be detected even in the presence of urea.

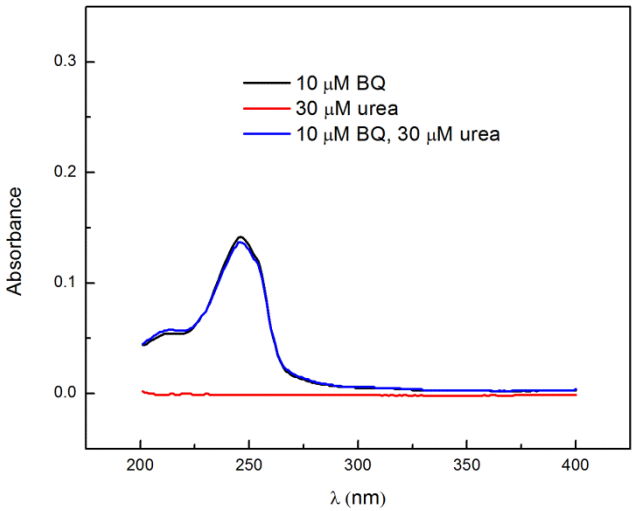

Figure 4.20: UV-vis spectra of BQ, urea, and urea-enhanced BQ solution.

FTIR was then conducted to further interpret the mechanism of solubilization. Figure 4.15c compares the spectra of H_2BQ, urea and urea enhanced H_2BQ solution, and obvious band variations in the region between 3000 and 4000 cm^{-1} were detected. The pure H_2BQ solution shows a broad band at 3373 cm^{-1}, which is ascribed to the hydrogen-bonded OH stretching vibration, and the wavenumber between 3300 and 3500 cm^{-1} of urea points out the presence of NH stretching mode.[108] As indicated by the dotted line, the emergence of another minor peak at 3490 cm^{-1} in H_2BQ and urea mixed solution suggests the environmental change of the H_2BQ molecules. The band variation should arise from a manifestation of intermolecular interactions, including van der Waals interaction, hydrogen bond and cooperative effect.[109] In this region corresponding to stretching vibration of O-H groups, it is believed that hydrogen bonding is mainly responsible for the emergence of this minor band.

The NMR measurements were conducted to elucidate the hydrotropic chemistry, and ^{1}H NMR spectroscopy was performed in D_2O for all three samples (Figure 4.15d). Due to the rapid exchange of protons with deuterons, no spectra corresponding to the hydroxyl or amine groups were seen, and the chemical shift at 4.65 ppm of all three solutions corresponds to water. It should be noted that the obvious signal shift of ^{1}H-atoms on the aromatic ring, as labeled by the dotted line at about 6.6 ppm, further demonstrates the environmental variation around H_2BQ molecules, which is consistent with the FTIR results. To give a full picture of the hydrotropic effect, the ^{1}H NMR spectroscopy was also conducted on the BQ solution (Figure 4.21), and the environmental variation enabled by urea is also evidenced by the signal shift of ^{1}H-atoms on BQ. We also conducted ^{13}C NMR measurements to probe into the environmental change around quinone molecules. Nevertheless, almost no chemical shift variations can be observed for all the samples (Figure 4.22). According to related literatures, generally H atoms are located on the end of a molecule, thus the chemical shift of ^{1}H NMR is greatly affected by the neighboring molecules. On the other hand, carbon atoms are located at the backbone of a molecule, thus the chemical shift of ^{13}C NMR is more sensitive to intramolecular forces. Because the hydrotropic effect is attributed to the intermolecular interactions between solute, solvent and hydrotrope molecules, it is reasonable to see more obvious chemical shift changes from ^{1}H NMR. Considering that the interaction between H_2BQ and urea is not dominant, as proven by UV-vis spectroscopy, the environmental change should be ascribed to the attraction and association of solvent with solute molecules.

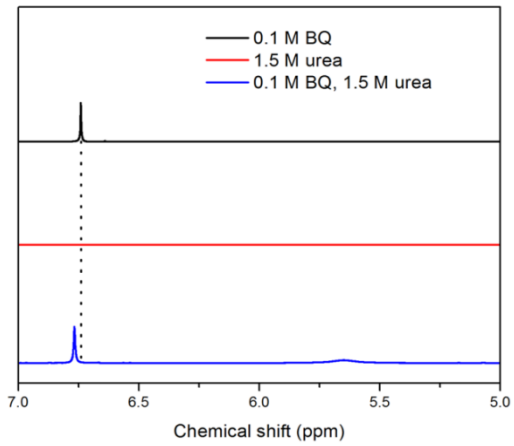

Figure 4.21: ^{1}H NMR spectra of BQ, urea, and urea-enhanced BQ solution.

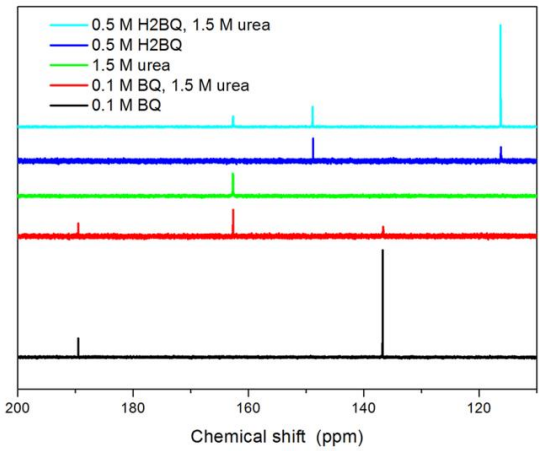

Figure 4.22: ^{13}C NMR spectra of urea-enhanced H_2BQ, H_2BQ, urea, urea-enhanced BQ, and BQ solution.

For further insight into the origin of the solubilization mechanism, molecular dynamics (MD) simulation was employed to probe into solute interactions in a hydrotropic solution model system. The solubility of H_2BQ in water is 0.53 M, but is enhanced to 0.75 M and 1.4 M in 0.5 M and 4 M urea aqueous solution, respectively. Based on these molecular ratios, the model system was built consisting of H_2BQ, urea, and water

molecules dispersed randomly using the Amber software package. In a typical solvation process, the solute molecules prefer to spread out and become surrounded by water molecules. In contrast, insoluble substances tend to maintain interactions between solute molecules instead of breaking apart.[110] Herein, the radial distribution function is provided to clarify the structural evolvement and molecular interactions. The radial distribution functions between H_2BQ and water molecules in Figure 4.23 show sharp peaks at around 3 Å. By comparing the intensity of the peaks in the inset, it is inferred that adding urea can reinforce the intermolecular interactions between solute and solvent. The radial distribution functions between the solute and the hydrotropic agent were also calculated as present in Figure 4.24, and we can observe attenuated interactions when adding more urea into the system, affirming that the enhanced solubility is not contributed by the formation of molecular aggregation between H_2BQ and urea molecules. The radial distribution functions, in consistent with the afore-mentioned chemical characterization, not only reveal the change in solvation structures, but also shed light on the nature and mechanisms of the hydrotropic process.

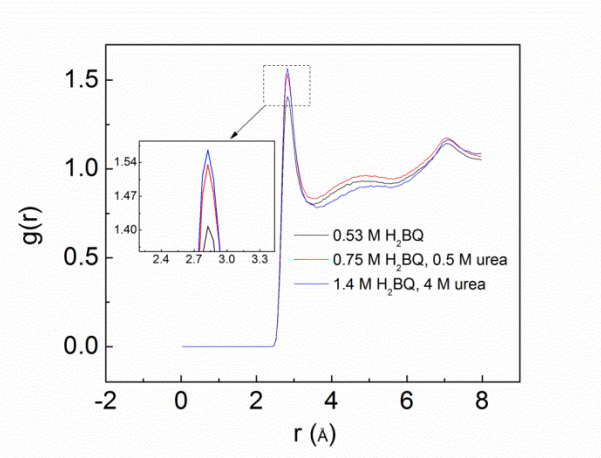

Figure 4.23: Radial distribution functions g(r) with respect to distance between H_2BQ-water.

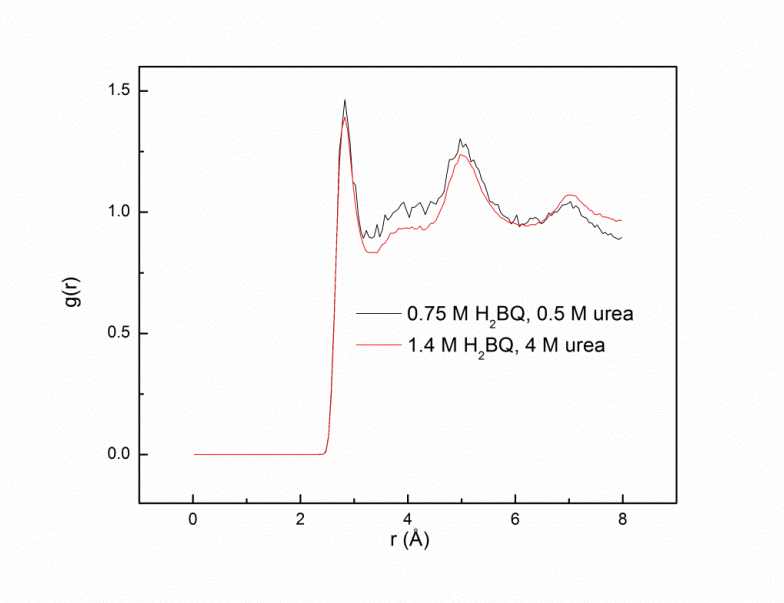

Figure 4.24: Radial distribution functions g(r) with respect to distance between H_2BQ-urea.

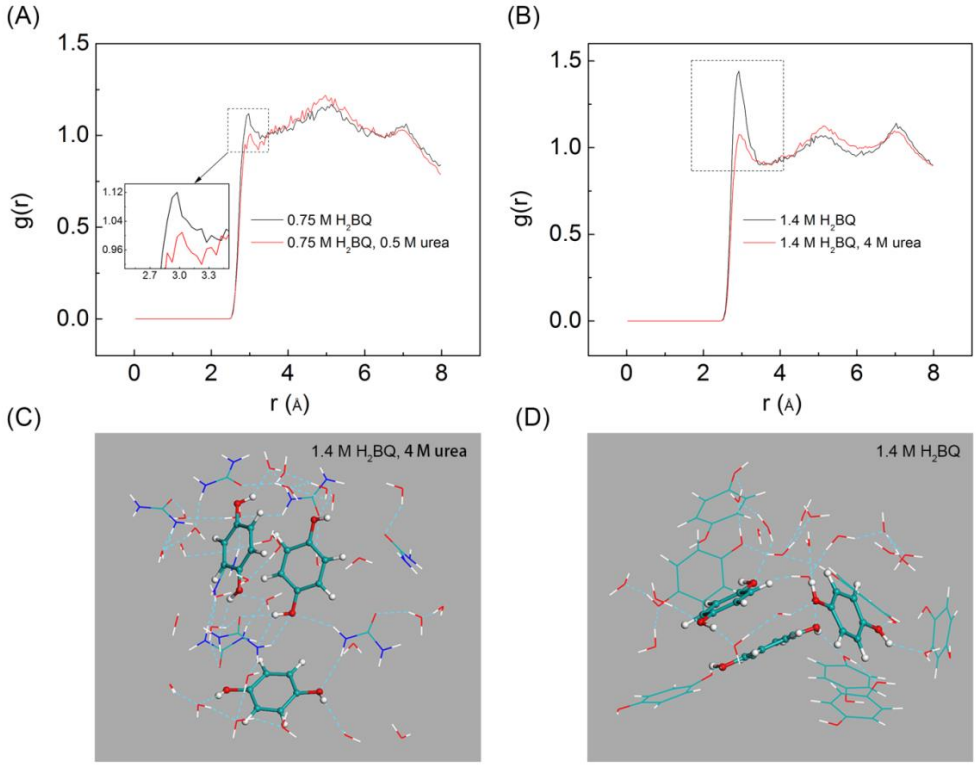

Figure 4.25: MD simulations of H_2BQ solutions with and without urea. (A and B) Radial distribution functions g(r) with respect to distance between H_2BQ-H_2BQ in 0.75 M H_2BQ solution, 0.75 M H_2BQ and 0.5 M urea solution, 1.4 M H_2BQ solution, 1.4 M H_2BQ and 4 M urea solution, respectively. (C and D) Molecular graphics represent the spatial distribution and hydrogen bonds (cyan dashed lines) around three adjacent H_2BQ molecules (ball-and-stick models) within 5 Å in 1.4 M H_2BQ and 4 M urea solution, 1.4 M H_2BQ solution, respectively.

To confirm the effect of the hydrotropic agent, the radial distribution functions between H_2BQ molecules were calculated before and after adding urea (Figure 4.25A and 4.25B), and it is evident that urea molecules play a critical role in reorganizing the H_2BQ and water molecules. By comparing the first peaks in radial distribution functions, the general trend shows that the contact between H_2BQ molecules becomes looser when hydrotropic agent of urea was added. When the concentration of H_2BQ was increased

from 0.53 M to 1.4 M in the presence of 4 M urea (Figure 4.25B), we can see distinctly the subdued interaction between H_2BQ molecules as highlighted in the dashed rectangle. Furthermore, we simulated the molecule distribution and hydrogen bonds around H_2BQ molecules within 5 Å in 1.4 M H_2BQ solution with or without urea, as shown in Figure 4.25C and 4.25D. It is observed that the randomly selected three adjacent H_2BQ molecules are surrounded only by water and urea molecules in the urea-enhanced solution (Figure 4.25C). Nevertheless, seven H_2BQ molecules are detected around the randomly selected three H_2BQ molecules within the same distance of 5 Å without urea as hydrotropic agent (Figure 4.25D). This result also confirms the weakened contact between H_2BQ molecules and the uniform distribution of solute molecules in the presence of hydrotrope agents. Meanwhile, more hydrogen bonds can be observed when urea was added, which should play a key role in reorganizing the solute and solvent molecules.

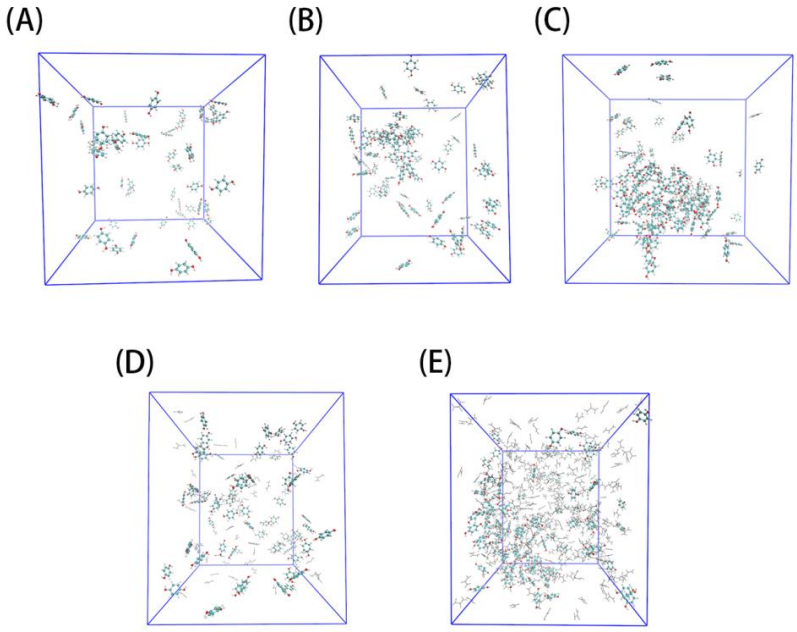

Figure 4.26: Snapshots of MD simulations of H_2BQ solutions with and without urea. H_2BQ molecules are represented by colorful ball-and-stick models. Urea molecules are represented by black skeletal structures, and water molecules are not shown. (A) Snapshot of 0.53 M H_2BQ in water at MD time 100 ns. (B) Snapshot of 0.75 M H_2BQ in water at MD time 100 ns. (C) Snapshot of 1.4 M H_2BQ in water at MD time 100 ns. (D) Snapshot of 0.75 M H_2BQ and 0.5 M urea in water at MD time 100 ns. (E) Snapshot of 1.4 M H_2BQ and 4 M urea in water at MD time 100 ns.

More intuitive evidence can be acquired from the snapshots of simulated systems. Without urea as a hydrotropic agent, minor stacking of H_2BQ molecules can be detected in Figure 4.26A. The aggregation becomes more serious when increasing the concentration of H_2BQ (Figure 4.26B and 4.26C), indicating phase separation and precipitation due to partitioning of the solute and water. In comparison, uniformly distributed H_2BQ molecules can be observed in the presence of urea as a hydrotrope (Figure 4.26D and 4.26E), thus leading to enhanced solubility. The number of hydrogen bonds at different times in the hydrotropic solution (1ps corresponds to the initial state

and 100,000 ps corresponds to the equilibrium state), displayed in Table 4.2, shows the notably reinforced hydrogen bonding between the solute and solvent molecules and the inhibited association between solute molecules in the solvation process, which correlates well with experimental and computational results. Given the facts above, we conclude that hydrogen bonding between the solute and solvent molecules facilitated by hydrotropes should be the driving force of the hydrotropic solubilization.

	t (ps)	H_2BQ-H_2O	H_2BQ-H_2BQ	Urea-Urea	H_2BQ-Urea
0.75 M H_2BQ, 0.50 M Urea	1	35	5	1	10
	10^5	134	2	1	3
1.4 M H_2BQ, 4.0 M Urea	1	24	10	23	57
	10^5	184	8	57	35

Table 4.2: Calculated hydrogen bonds in two hydrotropic solutions of H_2BQ and urea at 1 ps and 100,000 ps.

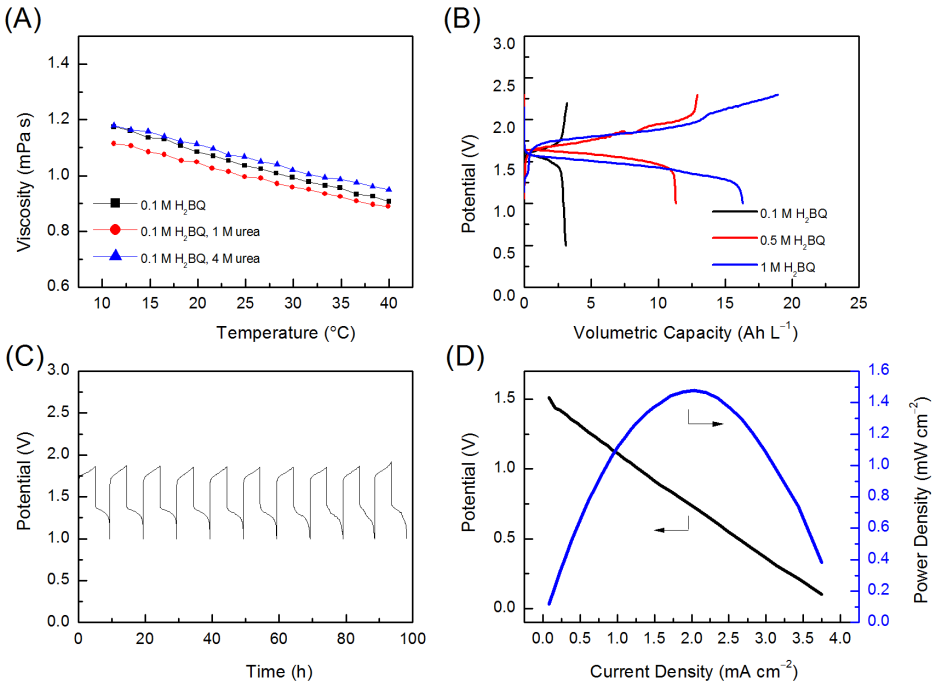

Figure 4.27: The electrolyte properties and cell performances. (A) Viscosity of H_2BQ-based catholyte at different concentrations of urea. (B) Volumetric capacity of the RFB at different concentrations of H_2BQ. The anolyte is Al-based DES with the catholyte composition: 0.1 M H_2BQ at 100 μA cm^{-2}; 0.5 M H_2BQ, 1.5 M urea at 100 μA cm^{-2}; 1 M H_2BQ, 4 M urea at 200 μA cm^{-2}. (C) Cycling stability of the RFB at 200 μA cm^{-2}. The anolyte is Al-based DES with the catholyte composition: 0.5 M H_2BQ, 1.5 M urea. (D) Polarization curve of the flow battery at a flow rate of 4 mL min^{-1}. The anolyte is Al-based DES with the catholyte composition: 0.5 M H_2BQ, 1.5 M urea.

In view of the noticeably enhanced solubility of H_2BQ in water, a high-energy RFB is conceived. To validate the feasibility of the hydrotropic catholyte, the influence of urea on the electrochemical properties of H_2BQ should be taken into consideration. As mentioned above, electrolytes with low viscosities are preferred to maintain high ionic conductivity and low pumping costs. Figure 4.27A gives the viscosity-temperature plot of the H_2BQ-based catholyte, in which only slight variation of viscosity can be observed

with different concentrations of urea. Notably, the solution's viscosity even decreases when 1 M urea was added, which is beneficial in practical applications.

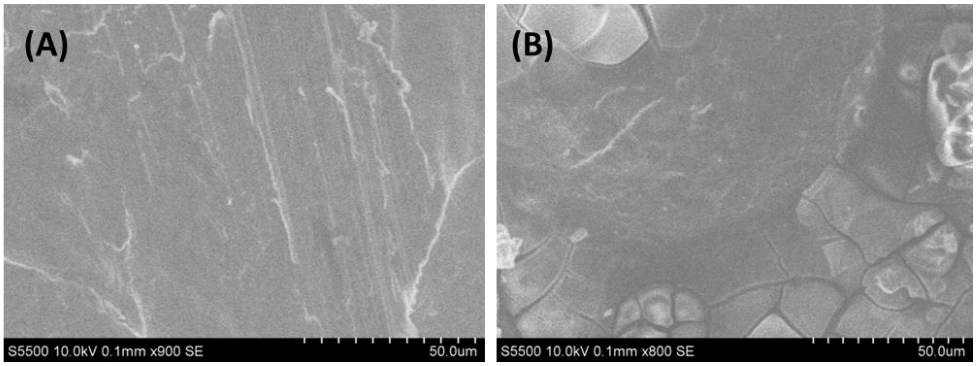

Figure 4.28: The SEM image of Al anode before (A) and after cycling (B).

In the proof-of-concept battery system, a hydrotropic solubilization-enhanced hybrid ion RFB was built employing urea as a hydrotropic agent and Al-based DES as anolyte. Figure 4.27B shows the performance of the flow battery at different concentrations of H_2BQ. At a high concentration of 1 M H_2BQ, the practical energy density reaches 25.3 Wh L^{-1}, which is also comparable with reported organic RFBs.[111] Despite that the maximum solubility of BQ cannot compete with H_2BQ even in the presence of urea, it is interesting to find that precipitation of BQ will not occur in the battery test due to the improved hydrotropic effect of urea in weak base electrolyte solution. The cycling stability of the hybrid ion flow battery is given in Figure 4.27C, in which little degradation can be found from the steady charge/discharge profiles for nearly 100 hours. Despite that the current density cannot compete with aqueous flow batteries in light of the high viscosity of DES-based anolytes, it is still comparable with most reported non-aqueous flow batter-ies. No dendrites were observed on the surface of the Al anode after battery cycling (Figure 4.28A and 4.28B), showing promise of novel

anolyte alternatives for highly safe RFBs. Furthermore, the chemical sta-bility of the anoltye can be evidenced from the EDS pat-terns of the Al anode before and after battery cycling (Figure 4.29), which shows little composition change on the Al surface. To evaluate the battery performance in flow mode, the polarization curve at a flow rate of 4 mL min^{-1} was plotted in Figure 4.27D, and the power density of 1.5 mW cm^{-2} can be output at a current density of 2 mA cm^{-2}. Improved performance can be realized through modification of the DESs, optimization of the cell design and exploitation of better membrane separators.

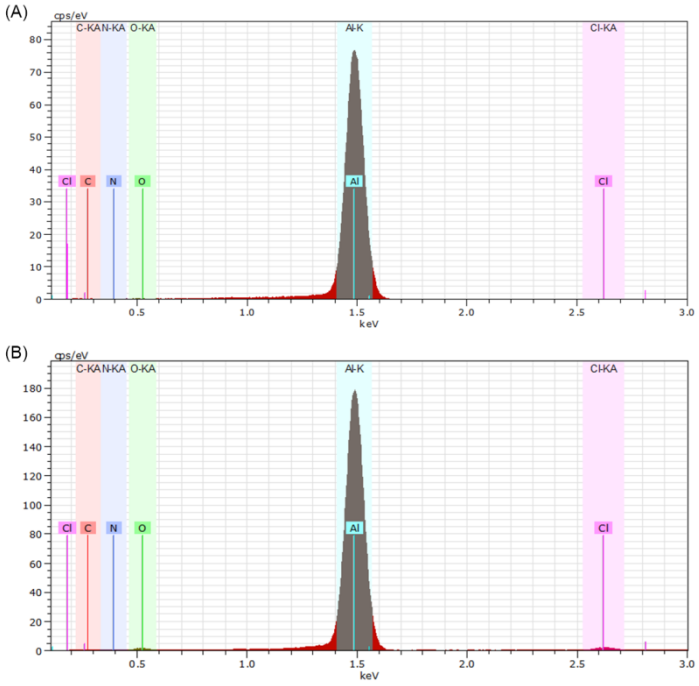

Figure 4.29: EDS patterns of the Al anode before (A) and after (B) battery cycling.

By leveraging the knowledge of solubility enhancement techniques in pharmaceutical research, we developed a novel hybrid ion RFB employing a hy-drotropy-enabled H_2BQ solution as catholyte and an Al-based DES as anolyte. In this work, a three-fold increase in the solubility of H_2BQ is achieved without sacrificing the

electrochemical properties of the redox-active materials. Compared with chemical functionalization to enhance the solubility of organic redox species, the hydrotropic solubilization technique represents a sustainable and costeffective approach to the design of grid-scale energy storage systems. A comprehensive study unifying chemical characterizations and MD simulations reveals that the hydrotropic mechanism arises from the favorable solvation process stemming from strong solvent-solute interactions. Meanwhile, biodegradable and non-flammable DESs were explored to serve as high concentration anolytes with low working voltage. Incorporating a eutectic mixture of Lewis acids and bases, both Al- and Zn-based anolytes exhibit reversible redox reactions with multiple-electron transfer processes and dendrite-free features, providing a useful platform for developing novel redox species based on new chemistry. Moreover, this hydrotropic solubilization approach is more cost-effective than laborious organic functionalization methods, and the electrochemically inert hydrotropic agents can be reused even after the battery dies. This integrated study not only spans these disciplines, but can be further extended to other solubility enhancement techniques inspired by pharmaceutics. All these features promise a new generation of energy storage sources for stationary applications, and more attention need be geared toward extensive screening and tuning of hydrotropic agents and organic molecules to achieve high concentration, low cost and long cycle life.

4.4 Molecular Engineered Quinones for Non-Aqueous RFBs: A Combined Experimental and Computational Study*

4.4.1 Introduction

Despite the progress that has been made in the recent decade, the exploitation of organic compounds for Li-ion batteries is still limited by some of their intrinsic properties. The low ionic conductivity of organics without well-defined conducting channels may lead to poor rate capability, and high solubility in aprotic electrolyte will cause the degraded cyclability.[24,112,113] Instead of using complex molecular modification to alleviate those issues, we focus on optimizing the high solubility of organic materials, corresponding to the exact requirements in RFBs. In contrast to solid-state batteries, the liquid electrode not only demands high solubility of redox species to achieve high energy density, but also leads to potentially better rate capability due to larger diffusion coefficient of species in liquid. Moreover, the decoupling between the power density and the energy density of RFBs is highly advantageous for efficient grid-scale energy storage.

Quinones are the principal redox-active moieties within natural organic matter, and play a key role in electron transport processes of biological systems. Their applications in the field of energy storage have been investigated, but the cyclability in solid-state Li-ion battery is still restricted by the dissolution of quinones in organic electrolyte. Meanwhile, the potential is constrained by the electrolysis of water in aqueous RFBs. In contrast, a non-aqueous RFB can avoid these constraints by taking advantage of the high solubility of quinones in aprotic electrolyte with a wide potential window. Therefore, a comprehensive study integrating molecular design, electrochemical

* Y. Ding, Y. Li, G. Yu, Exploring bio-inspired quinone-based organic redox flow batteries: a combined experimental and computational study, *Chem*, 2016, 1, 790.
Y. D. carried out the experimental work and co-led the writing of the manuscript with Prof. Yu.

analysis, and computational modeling is needed to better understand the redox characteristics of these materials, especially for non-aqueous RFB applications.

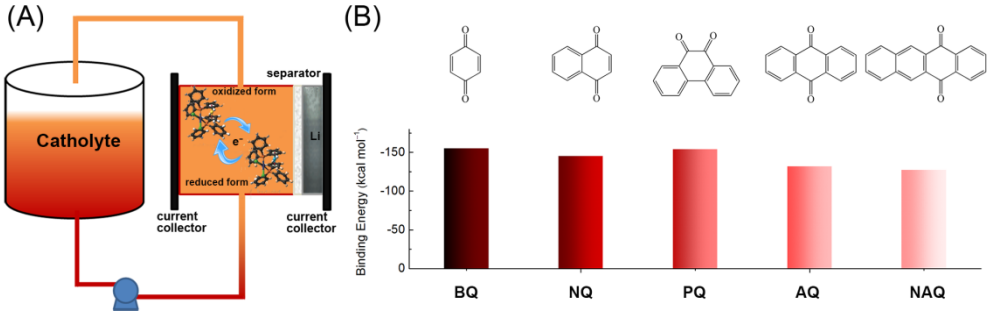

Figure 4.30: (A) Schematic of the RFB with Li metal as anode and quinone in aprotic electrolyte as catholyte. (B) Chemical structures and calculated Li binding energies of five quinone-based organic redox species.

To this end, we systematically investigated the performances of quinones in non-aqueous RFBs (the working principle is shown in Figure 4.30A). Different from aqueous electrolyte, in which the potential window is confined to 1.23 V, aprotic electrolyte provides a wider potential window and more flexibility in tuning both physical and chemical properties of quinones by solvent selection. Quinones, as a family of molecules derived from aromatic compounds such as benzene or naphthalene, maintain a fully conjugated cyclic diketone structure, and their redox reaction is based on the reorganization of the conjugated double bond. This research aims to elucidate the reaction mechanisms of quinone-based electrode materials with multi-electron reactions for non-aqueous RFB applications.

The series of quinones, benzoquinone (BQ), naphthoquinone (NQ), phenanthraquinone (PQ), anthraquinone (AQ) and naphthacenequinone (NAQ), were studied to investigate the relationship between their molecular structures and electrochemical properties. It is found that the redox potentials lie between 2.0 and 3.0 V vs. Li^+/Li, and are related to molecular backbone aromaticity. In addition to their high

voltage, a promising redox species should also be highly soluble in order to enable high volumetric energy density. Experiments show that the solubility of quinones is affected by molecular structures, and higher densities of arenes will lead to lower solubility. Further theoretical modeling helped us grasp Li-binding characteristics, electronic properties and structural stabilities of quinones, which govern electrochemical performance. Such a systematic study provides a general design principle of organic RFBs by integrating rational molecular screening, fundamental electrochemical analysis and advanced computational modeling. The bio-inspired feature of quinones promises a next-generation energy technology with low carbon-footprint and green battery cycle life.

4.4.2 Experimental

In RFB test, the catholyte contains 1 M NQ, 0.5 M LiTFSI or 0.2 M PQ, 0.5 M LiTFSI in DMA. In the galvanostatic charge/discharge test after the battery stabilized, the catholyte contains 0.1 M BQ, NQ or PQ, 0.5 M LiTFSI in DMA at a rate of 0.05 C. For AQ and NAQ, due to limited solubility, the concentration is set at 0.05 M with a cycling rate of 0.1 C. Higher concentration of 0.2 M and 1M of NQ was also prepared for cycling test. The cycling stability of 0.2 M NQ based battery since the second cycle. At 1 M, the battery was cycled at 0.025C for 10 cycles and rested for one day for activation. The capacity and the energy density were calculated based on the volume of quinone solution. The electrochemical tests of static mode battery were performed on BioLogic VMP3 potentiostat system.

CV test was performed with platinum disk (2 mm diameter) as working electrode, platinum wire as counter electrode, and 0.01 M $AgNO_3$, 0.1 M TBAP/CH_3CN as reference electrode. The solution contained 5 mM quinone, 0.2 M LiTFSI in DMA at

scan rates of 0.02, 0.05, 0.1, 0.2 and 0.5 V s^{-1}. Diffusion coefficient was calculated from Randles-Sevcik equation.

$$I_p=269000\times n^{1.5}AD^{0.5}\ v^{0.}\ C$$

where I_p is the peak current, n is the number of electrons transferred, A is the electrode area, D is diffusion coefficient, v is scan rate and C is concentration. Both the flow mode battery test and CV measurements were conducted on Autolab (PGSTAT302N) electrochemical workstation in an argon-filled glove box.

Computational methods: All computations, including geometry optimizations, frequency analyses, and electronic structure computations were performed at the B3LYP47, 48 level of theory with the 6-31+G(d, p) basis set as implemented in Gaussian 09 package. The dielectric constant was set as 37.78 for DMA solvent. We evaluated the change in Gibbs free energy (ΔG) for lithiation steps, as defined as:

$$\Delta G=BE+\Delta E_{zpe}-T\Delta S+\Delta PV$$

The lithium binding energy (BE) of quinone derivative can be directly determined by analyzing the DFT total energies following equation :

$$BE=E_{Q+Li}-E_Q-E_{Li}$$

where E_{Q+Li}, E_Q, and E_{Li} are the DFT total energies of quinine-Li complex , free quinine, and Li atom, respectively.

ΔE_{zpe} and ΔS are the zero point energy difference and the entropy difference between the products and reactants. For each system, its E_{zpe} can be calculated by summing vibrational frequencies over all normal modes ν ($E_{zpe}=1/2\sum\hbar\nu$). P, V, and T are pressure, volume, and temperature (298.15K, in our work), respectively.

4.4.3 Results and Discussion

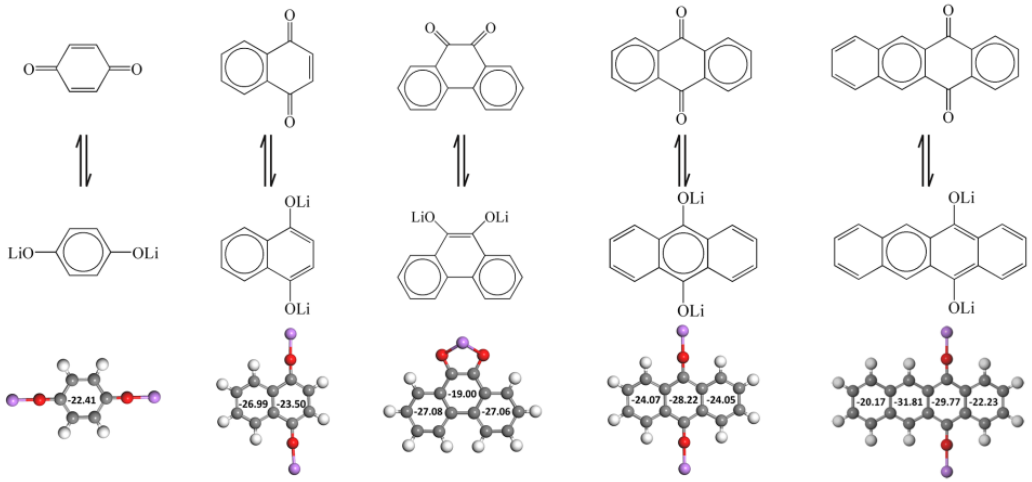

Figure 4.31: Clar structures of quinones, the two-electron reduction states and the calculated nucleus-independent chemical shifts (NICS) values. NICS values are labelled to indicate the position of sextets in resonance Clar structures.

The chemical structures and calculated binding energies (BE) of five quinones are presented in Figure 4.30B. BE refers to energy released upon creation of the quinone-Li complex, and a negative value indicates favorable binding. In our system, DMA was selected as solvent considering the relatively high dielectric constant, low density and low viscosity. It is noted that increasing the cyclic rings from BQ to NAQ leads to less negative binding energies in general, which manifests that BQ maintains the highest tendency to bind lithium ions. This trend can be explained by the degree of aromaticity. All two-electron reduction states of quinones follow Hückel's rule with π-electrons equaling 4n+2. However, there are certain discrepancies in aromaticity when considering each ring. In light of Clar's rule for polycyclic aromatic hydrocarbon, the Kekulé resonance structure with the greatest number of benzenoid rings is the most stable.[114] Figure 4.31 shows the Clar structures of quinones before and after two-electron reduction. In the case of Li_2BQ, the monocyclic structure meets Hückel's rule to have one

sextet. In other polycyclic quinones, Li_2PQ has two sextets in three rings, followed by one sextet in two rings of Li_2NQ, one sextet in three rings of Li_2AQ and one sextet in four rings of Li_2NAQ. The order of calculated binding energy is the same as the ratio of sextets in Clar structures of reduced quinones. Therefore, Li_2BQ possesses the highest stability with the most energy evolved due to possessing the highest ratio of sextets in rings. For AQ and NAQ, the relatively small binding energy is contributed by the low degree of aromaticity after reduction. The calculated nucleus-independent chemical shifts (NICS) values, in which negative NICS values correspond to aromaticity and positive values correspond to antiaromaticity, are also labelled to indicate the position of sextets in resonance Clar structures.[115]

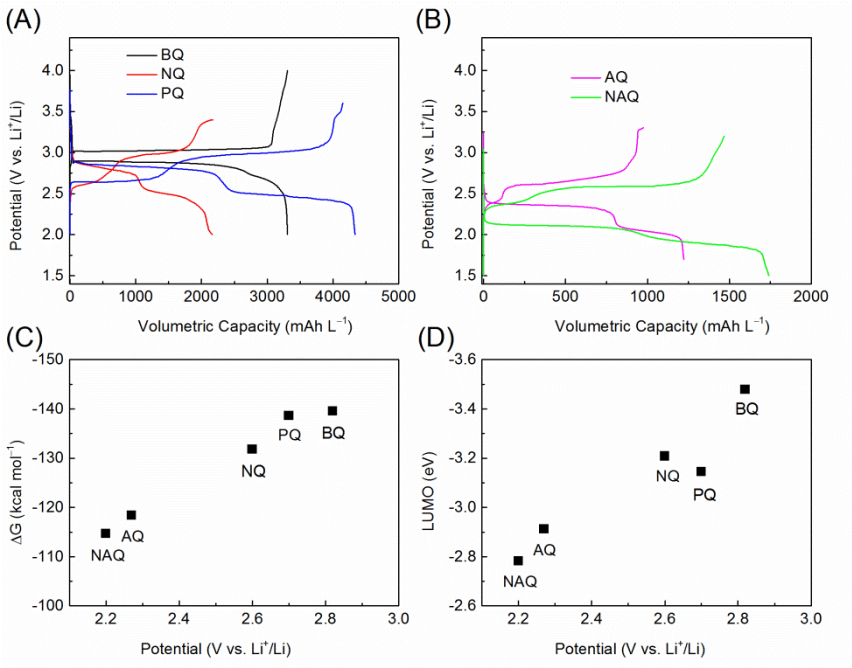

Figure 4.32: (A) Galvanostatic charge-discharge curves of 0.1 M BQ, 0.1 M NQ, 0.1 M PQ in DMA using 0.5 M LiTFSI salt at 0.05 C separately. (B) Galvanostatic charge-discharge curves of 0.05 M AQ, 0.05 M NAQ in DMA using 0.5 M LiTFSI salt at 0.1 C separately. Correlation of experimental redox potential of quinones with (C) calculated Gibbs free energy change and (D) LUMO energy.

To further examine the structure-dependent properties, quinone-based catholytes were tested in a battery for electrochemical measurements. Galvanostatic charge/discharge tests were initially conducted to characterize electrochemical properties of different kinds of quinone solutions. Catholyte containing 0.1 M quinone was prepared and used for BQ, NQ and PQ. Due to the limited solubility of AQ and NAQ, the concentration was set at 0.05 M. Figure 4.32A, 4.32B show voltage profiles of quinones at the same current density; at a rate of 0.05 C for BQ NQ and PQ, and 0.1 C for AQ and NAQ. The relatively low CE of AQ and NAQ can be attributed to the precipitation of electroactive materials. The slightly sloping curves observed in the end of charging process can be ascribed to the oxidation of quinone anions in multiple quinone-Li configurations. Volumetric capacity is determined by the number of electrons transferred and the volume of catholyte, therefore, quinones with the same concentration should have comparable capacities. But the lower capacity of NQ compared with PQ is affected by other factors, which will be discussed in the next section.

Figure 4.32C illustrates the relationship between redox potential and calculated change in Gibbs free energy. The calculated binding energy of quinone can be converted into Gibbs free energy after taking into account several factors including vibrational energy, pressure, volume, temperature, entropy etc. The trend is the same as that of binding energy, and has been explained by the degree of aromaticity of reduced quinones following Clar's aromatic π–sextet rule in Figure 4.31. Another hint is through calculating the lowest unoccupied molecular orbital (LUMO) energy. For molecules closely related in structures, reduction potentials are mostly linearly correlated with LUMO energies, as shown in Figure 4.32D.

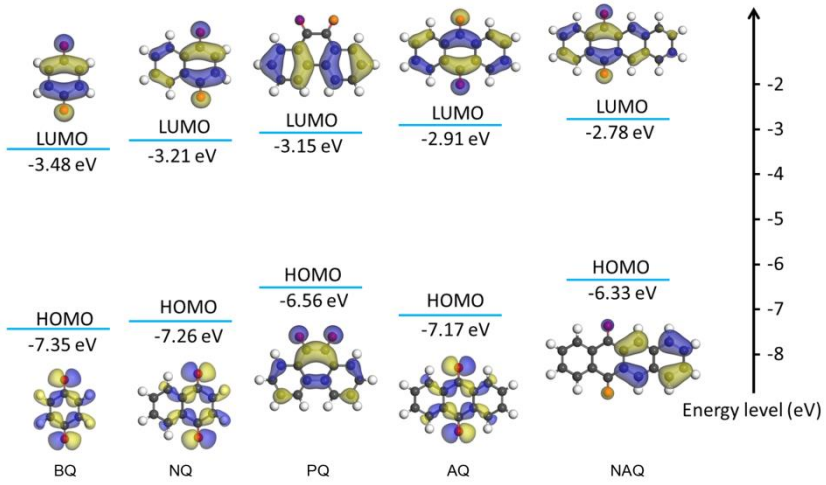

Figure 4.33: HOMO/LUMO plots of quinones and the correlated energy level diagram.

The structure-dependent electrochemical properties of quinones on redox potential have been revealed. According to Figure 4.32A, 4.32B, capacity utilization is also strongly related with the molecular structures. By calculating the ratio between experimental capacity and theoretical capacity, we obtained the capacity utilization of 80.9% for PQ, followed by 65.0% for NAQ, 61.7% for BQ, 45.6% for AQ and 40.5% for NQ. Given the fast diffusion process of quinones attested from CV measurement, mass transport might not be the limitation. Furthermore, the sequence of diffusion coefficients is inconsistent with the calculated capacity utilization of quinones. For further insight into the origin of capacity utilization discrepancies between different quinones, we employed density functional theory (DFT) modeling to obtain the electron density distribution of different reduction states of quinones. We further calculated HOMO and LUMO energy levels of all quinones (Figure 4.33). It has been demonstrated the linear relationship between LUMO energy level of quinones and their redox potential. Furthermore, the energy (E_g) of the HOMO-LUMO gap of quinones can also be obtained, which is 3.87,

4.05, 3.41, 4.26 and 3.55 eV in the sequence of BQ, NQ, PQ, AQ and NAQ, respectively. It is worth noting that the order of capacity utilizations almost follows the same trend as that of E_g values of quinones, with a smaller gap corresponding to higher capacity utilization. In light of the frontier molecular orbitals theory, good conductivity of a molecule is attributed to small gaps between energy levels, allowing the molecule to have a strong flow of electrons. The low capacity utilizations of NQ and AQ are most likely attributed to low electrical conductivity due to high energy gaps.[116,117] The energy gap between HOMO and LUMO decreases when it comes to BQ, PQ and NAQ molecules, which facilitates better electron transfer at the interface of the current collector, leading to higher capacity utilizations. The above analysis suggests that an energy diagram is a useful tool for better understanding the electrochemical properties of organic-based redox species.

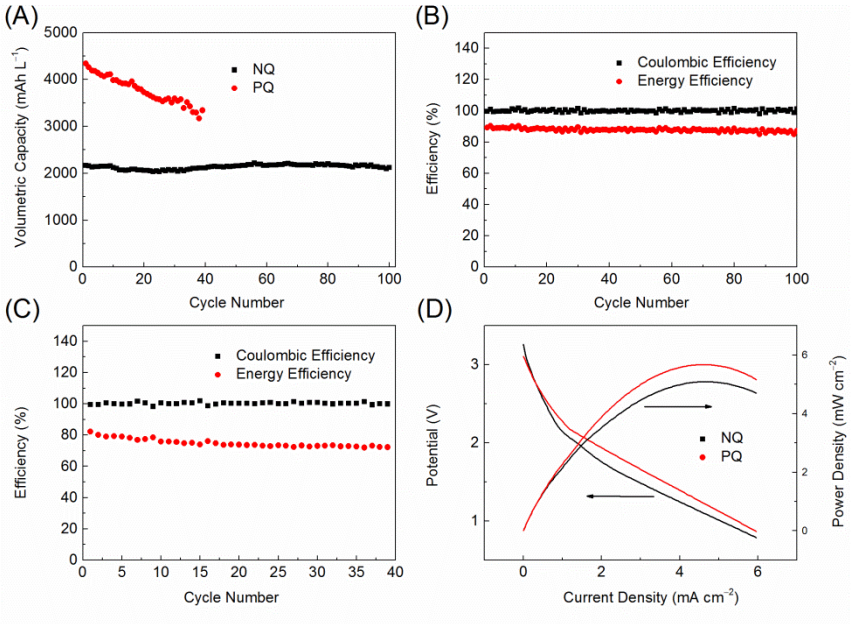

Figure 4.34: (A) Discharge capacity of NQ- and PQ-based battery at a rate of 0.05 C using 0.1 M NQ/0.5 M LiTFSI and 0.1 M PQ/0.5 M LiTFSI in DMA, respectively. (B) Corresponding efficiencies of NQ-based battery. (C) Efficiencies of PQ-based battery. (D) Polarization curves of flow mode battery.

After a systematic study integrating calculation modeling and electrochemical testing, cycling measurement was conducted to demonstrate the long-term stability of quinones under battery applications. Due to the limited solubility of AQ and NAQ, the capacity decayed very quickly arising from precipitation of electroactive materials, thus only BQ, NQ and PQ were subjected to the long-term charge/discharge tests. Although BQ is regarded as the most promising redox species with a simple structure, large solubility and high redox potential, its practical application is seriously restricted by poor cycling stability, and only 6.5% of initial capacity remained after 10 cycles in our testing. A relevant study of Senoh's work focused on BQ-based liquid battery is also plagued by the capacity degradation and the origin of this result is still an open question for further studies. Possible explanations for the fast degradation could be attributed to either

instability of the radical intermediate, a lack of adjacent aromatic rings to stabilize the enolate anions, or low reactivity of reaction products. Introducing peripheral substituents into BQ moiety to stabilize the intermediates might help to overcome the stability issue. Cycling performances of NQ and PQ are shown in Figure 4.34A, separately. PQ possesses better stability than BQ with 76.9% capacity retained after 40 cycles, and NQ stands out with the highest reversibility during cycling. For NQ, most of the capacity preserved, even after 100 cycles for two months, with a capacity retention of over 99.98% per cycle. Even when the concentration is increased to 1.0 M, little decay was observed after 20 cycles (Figure 4.35), and the gradual increase in capacity can be attributed to the activation process, considering the large E_g demonstrated before with DFT calculations. At the concentration of 1.0 M, the NQ-based battery can provide energy density of 60 Wh L^{-1} with a working potential about 2.7 V. Energy density of such a battery can be improved further by enhancing the carbonyl utilization via electronic tuning with functionalization or rational design of advanced catalysts. The energy density of PQ-based battery is limited by solubility (0.3 M in DMA), and modification with ether groups potentially lead to higher solubility.

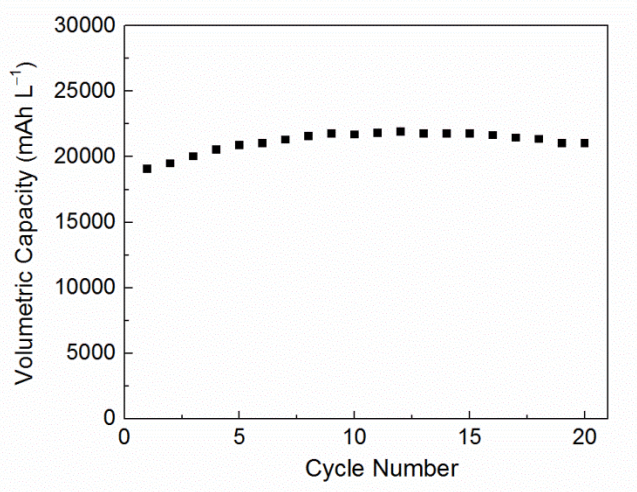

Figure 4.35: Cycling performance of battery composed of 1 M NQ, 0.5 LiTFSI in DMA at 0.025 C.

The performance of a flow mode battery was also demonstrated. Figure 4.34D shows the polarization curves of the flow battery at a flow rate of 4 mL min^{-1}, in which the power density of 5.1 mW cm^{-2} can be achieved at current density of 4.7 mA cm^{-2} for NQ. Similarly, power density could reach 5.7 mW cm^{-2} for PQ-based flow mode battery. We would like to mention here that the power density is just a demonstration of the flow mode battery without further optimization. The yielded power density is comparable with those reported non-aqueous flow batteries, but lower than aqueous flow batteries. Modification of the battery design and exploitation of advanced Li ion conducting membranes should lead to improved performance.

In summary, we have systematically investigated the Li-binding processes, redox properties, electronic structures and reversibility of quinones for organic RFBs. Different from recent reports on quinone-based energy storage systems, the Li-based non-aqueous RFB combines the advantages of Li-ion batteries and RFBs, circumventing the restrictions of quinones due to low ionic conductivity and dissolution. Meanwhile, by integrating molecular screening, electrochemical analysis and computational modeling,

this study promotes a better understanding of the reaction mechanisms of quinones and establishes the useful guideline for designing better bio-inspired redox species for energy applications. The Li-binding energies of quinones calculated via DFT methods reveal that feasibility of redox reaction of quinones is strongly dependent on its aromaticity. Subsequent electrochemical tests and computational models point out that the redox potential can be estimated by either the change in Gibbs free energy or LUMO energy. The utilization of carbonyl groups in quinones could be impacted by the HOMO-LUMO energy gap. In the prototype battery test, NQ presents the most promising performance with nearly 100% capacity retention after 100 cycles, and the demonstrated energy density reaches 60 Wh L^{-1}. These results characterize not only the electronic structures and redox properties of quinones, but we also demonstrate the practical features of quinones in RFB applications. Moreover, it is inferred that functional group modification of quinones could be a promising approach for tuning electronic properties, redox properties, and the solubility of these redox species. For example, while the HOMO/LUMO energy levels can be tuned through the functionalization of electron donating/withdrawing groups, the redox potential can be lifted through modification of electron withdrawing substituents, and enhanced solubility in polar solvents can be obtained via introduction of long-chain ethers. Quinones are considered to be the dominant redox-active moieties in nature: the derivative of BQ (plastoquinone) shuttles electrons from chlorophyll in all green plants,[118] derivative of NQ (Vitamin K) is the electron-transfer mediator in photosynthesis. Rhein, obtained from rhubarb, possesses the reaction moiety of AQ.[119] Since quinone derivatives can be extracted from biomass directly and the redox reactions mimic bioelectrochemical processes in nature, using such a family of bio-inspired organic redox species in RFBs could offer access to greener energy technologies. A combined experimental and theoretical approach in this study

reveals that the molecular tuning of quinone structures can pave the path towards sustainable energy storage devices.

Chapter 5: Summary*

Large-scale exploitation of renewable energy sources calls for high-performance and cost-effective energy storage devices. The use of organic and organometallic electroactive redox species for RFBs represents a promising direction for environmentally sustainable energy storage. In this dissertation, we summarize the design principles of organic redox species for such novel green energy systems and cover comprehensive synthetic strategies toward high electrochemical performance via function-oriented organic synthesis and molecular engineering.

In spite of influential advances made in the past decade, tremendous effort is needed to realize the practical applications of organic RFBs. As a core element of an electrochemical energy storage system, electroactive materials play a critical role in the electrochemical performance. The key performance metrics of a RFB, including energy density, power density, cycle life, efficiency, capital cost and ecological footprint, should be taken into consideration when designing redox species. Except for some hybrid RFBs applying Li metal as anode, the energy density of organic RFBs is still not competitive with traditional metal-based aqueous RFBs. Moreover, the power density of non-aqueous RFBs is far less than aqueous systems limited by the membrane and electrolyte conductivity. The target concentrations of organic species should reach 2 M in aqueous systems and 5 M in non-aqueous systems to be practically useful. Furthermore, longer cycling stability is needed in order to rival current stationary energy storage systems.

Deep eutectic solvents emerge as promising electroactive materials to meet the requirements in performance metrics owing to the appealing features such as low cost,

* Y. Ding, C. Zhang, L. Zhang, Y. Zhou and G. Yu, Molecular engineering of organic electroactive materials for redox flow batteries, *Chem. Soc. Rev.*, 2018, 47, 69.
Y. Ding, G. Yu, The promise of environmentally benign redox flow batteries by molecular engineering, *Angew. Chem. Int. Ed.*, 2017, 56, 8614.
Y. D. co-led the writing of the manuscripts with Prof. Yu.

high concentration, potential biodegradability, non-flammability and multi-electron transfer reactions. A typical eutectic electrolyte can be formed from a eutectic mixture of Lewis or Brønsted acids and bases containing a variety of ionic components as redox active materials. The large, asymmetric ions with delocalized charge lead to the reduced lattice energy and hence the lowered freezing points. Compared with conventional redox species for RFBs, the eutectic-based electrolyte can achieve much higher concentration (>3 M) because no additional solvents are needed to dissolve the redox species. The superconcentrated electrolyte and the multi-electron reaction offer a great opportunity to achieve the high energy density of over 200 Wh/L. In our current research, we have designed the novel anolyte based on Al eutectic solvent with a relatively low redox potential of 2.2 V vs Li^+/Li and an effective concentration of 3.2 M. Furthermore, we implemented the Fe-Al all eutectic-based non-aqueous RFB with a record energy density of 166 Wh/L. Given the broad design space of the eutectic redox species, their chemical and physical properties can be adjusted by molecular engineering of the eutectic components. What's more, to achieve the high-performance RFB in terms of power capability and stability, rational tuning of the functional additives to decrease the viscosity and then improve the ionic conductivity is needed.

The well-developed organic synthesis techniques promote the development of novel organic electroactive species with high solubility, suitable redox potential, multi-electron transfer reaction, chemical stability, and fast reaction kinetics to meet the requirements of high-performance batteries. Moreover, the effective synthetic methodology spurs the discovery and optimization of the most efficient and economic synthesis route to obtain the target molecule. In this research direction, which combines the academic disciplines of organic chemistry and energy science, the advanced synthesis methods will accelerate the selection and screening of organic redox alternatives.

Moreover, the characterization techniques for organic compounds will facilitate the comprehensive study of the chemistry of organic molecules, such as reaction reversibility, electron transfer, intermediate stability, and degradation mechanisms.

The rapid development of computational organic chemistry promotes its integration into designing organic and organometallic-based RFBs. On one hand, the computational models can offer a high-throughput screening approach to facilitate the selection of redox active molecules. On the other hand, it can provide insight into the reaction pathways, as well as geometric and electronic properties of reactants, products, intermediates, and transition-state structures, all of which are essential to understanding the working principles of organic and organometallic redox species.[120] Experimental methods are still needed to align with computational modelling to elucidate the unknowns in organic systems.

The structural diversity of organic materials allows the tailoring of solubility, electrochemical activity, and redox potential by substitutional functionalization. Likewise, the synthetic strategies can also be extended to modify the characteristics of membranes, which play a critical role in regulating the power density, cycling performance and efficiency of RFBs. It is anticipated that cost-effective low-cost membranes with high ion selectivity, conductivity, and chemical stability can also be prepared by rational molecular engineering methods in future research.[121]

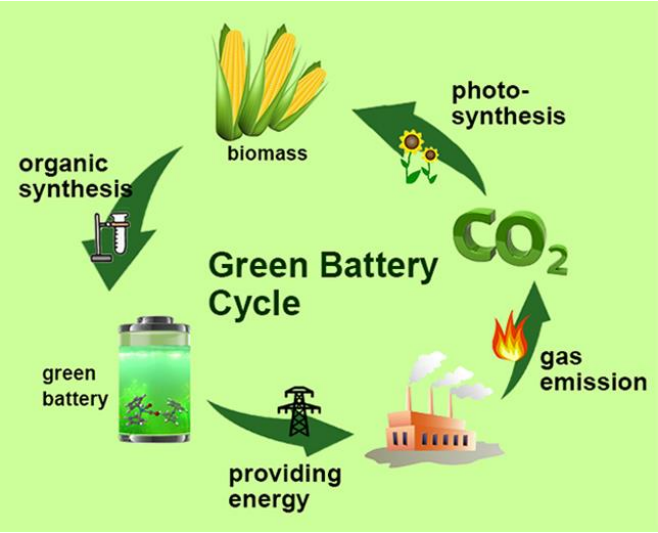

Figure 5.1: Ideal green battery cycle in the future with a low carbon footprint.

In addition to molecule and membrane modification, the improvement on battery performance also relies on advanced battery design. By using positive and negative electrodes composed of particles suspended in a carrier liquid and stored in outer tanks, such a semi-solid RFB combines the merits of both Li ion batteries and RFBs, including the high energy density and independent control of energy and power. Moreover, the photo-chargeable RFB provides an attractive means for in situ capture and storage of intermittent solar energy.[122] When integrating an organic solar cell with an organic RFB, the flexibility of organic molecules enables their use in both energy conversion and storage, representing an encouraging direction for sustainable energy storage. Moreover, the RFB can be further integrated with thermoelectric devices based on the principle of thermoelectric effect in thermalgalvanic cells to achieve broader thermal energy harvesting and storage, which is under development in our current research. The above innovative energy systems stretch the research boundaries of battery types, broaden the scope of novel energy devices with new battery chemistries, and exhibit the wider applicability of organic-based redox species via molecular engineering. All these features

promise a next-generation energy storage system with a low carbon footprint and it is promising to achieve green battery life cycle in the future (Figure 5.1).

References

(1) *Fossil fuel energy consumption*, DOI: http://data.worldbank.org/indicator/EG.USE.COMM.FO.ZS.

(2) Goodenough, J. B.; Kim, Y. *Chem Mater* **2010**, *22*, 587.

(3) Soloveichik, G. L. *Chem Rev* **2015**, *115*, 11533.

(4) Wang, Y.; He, P.; Zhou, H. *Adv. Energy Mater.* **2012**, *2*, 770.

(5) Park, M.; Ryu, J.; Wang, W.; Cho, J. *Nat Rev Mater* **2016**, *2*, 16080.

(6) Song, Z.; Zhou, H. *Energy Environ Sci.* **2013**, *6*, 2280.

(7) Wang, Y.; Ding, Y.; Pan, L.; Shi, Y.; Yue, Z.; Shi, Y.; Yu, G. *Nano Lett.* **2016**, *16*, 3329.

(8) Schon, T. B.; McAllister, B. T.; Li, P.-F.; Seferos, D. S. *Chem Soc Rev* **2016**, *45*, 6345.

(9) Huskinson, B.; Marshak, M. P.; Suh, C.; Er, S.; Gerhardt, M. R.; Galvin, C. J.; Chen, X.; Aspuru-Guzik, A.; Gordon, R. G.; Aziz, M. J. *Nature* **2014**, *505*, 195.

(10) Ding, Y.; Zhang, C.; Zhang, L.; Zhou, Y.; Yu, G. *Chem Soc Rev* **2018**, *47*, 69.

(11) Shin, S.-H.; Yun, S.-H.; Moon, S.-H. *RSC Advances* **2013**, *3*, 9095.

(12) Zhao, Y.; Hong, M.; Bonnet Mercier, N.; Yu, G.; Choi, H. C.; Byon, H. R. *Nano Lett.* **2014**, *14*, 1085.

(13) Darling, R. M.; Gallagher, K. G.; Kowalski, J. A.; Ha, S.; Brushett, F. R. *Energy Environ Sci.* **2014**, *7*, 3459.

(14) Zhao, Y.; Ding, Y.; Li, Y.; Peng, L.; Byon, H. R.; Goodenough, J. B.; Yu, G. *Chem Soc Rev* **2015**, *44*, 7968.

(15) Barton, A. F. M. *Chem Rev* **1975**, *75*, 731.

(16) Kuleshova, L. N.; Hofmann, D. W. M.; Boese, R. *Chem Phys Lett* **2013**, *564*, 26.

(17) Paruta, A. N.; Sciarrone, B. J.; Lordi, N. G. *J Pharm Sci* **1964**, *53*, 1349.

(18) Montes, I.; Lai, C.; Sanabria, D. *J Chem Educ* **2003**, *80*, 447.

(19) Tao, M.; Wang, Z.; Gong, J.; Hao, H.; Wang, J. *Ind Eng Chem Res* **2013**, *52*, 3036.

(20) Skyner, R. E.; McDonagh, J. L.; Groom, C. R.; van Mourik, T.; Mitchell, J. B. O. *Phys Chem Chem Phys* **2015**, *17*, 6174.

(21) Delahay, P.; Pourbaix, M.; Van Rysselberghe, P. *J Chem Educ* **1950**, *27*, 683.

(22) Lee, M.; Hong, J.; Seo, D.-H.; Nam, D. H.; Nam, K. T.; Kang, K.; Park, C. B. *Angew Chem Int Ed* **2013**, *52*, 8322.

(23) Lee, J.; Park, M. J. *Adv. Energy Mater.* **2017**, *7*, 1602279.

(24) Song, Z.; Qian, Y.; Gordin, M. L.; Tang, D.; Xu, T.; Otani, M.; Zhan, H.; Zhou, H.; Wang, D. *Angew Chem Int Ed* **2015**, *54*, 13947.

(25) Kim, K. C.; Liu, T.; Lee, S. W.; Jang, S. S. *J Am Chem Soc* **2016**, *138*, 2374.

(26) Bachman, J. C.; Kavian, R.; Graham, D. J.; Kim, D. Y.; Noda, S.; Nocera, D. G.; Shao-Horn, Y.; Lee, S. W. *Nat. Commun.* **2015**, *6*, 7040.

(27) Domingo, L. R.; Pérez, P.; Contreras, R. *The Journal of Organic Chemistry* **2003**, *68*, 6060.
(28) Job, D.; Dunford, H. B. *Eur J Biochem* **1976**, *66*, 607.
(29) Zhao, Y.; Wang, L.; Byon, H. R. *Nat. Commun.* **2013**, *4*, 1896.
(30) Mauritz, K. A.; Moore, R. B. *Chem Rev* **2004**, *104*, 4535.
(31) Montoto, E. C.; Nagarjuna, G.; Hui, J.; Burgess, M.; Sekerak, N. M.; Hernández-Burgos, K.; Wei, T.-S.; Kneer, M.; Grolman, J.; Cheng, K. J.; Lewis, J. A.; Moore, J. S.; Rodríguez-López, J. *J Am Chem Soc* **2016**, *138*, 13230.
(32) Burgess, M.; Moore, J. S.; Rodríguez-López, J. *Acc. Chem. Res.* **2016**, *49*, 2649.
(33) Yamaguchi, Y.; Ding, W.; Sanderson, C. T.; Borden, M. L.; Morgan, M. J.; Kutal, C. *Coordin Chem Rev* **2007**, *251*, 515.
(34) Gray, H. B.; Sohn, Y. S.; Hendrickson, N. *J Am Chem Soc* **1971**, *93*, 3603.
(35) Dunn, B.; Kamath, H.; Tarascon, J.-M. *Science* **2011**, *334*, 928.
(36) Lu, Y.; Goodenough, J. B.; Kim, Y. *J Am Chem Soc* **2011**, *133*, 5756.
(37) Park, K.; Cho, J. H.; Shanmuganathan, K.; Song, J.; Peng, J.; Gobet, M.; Greenbaum, S.; Ellison, C. J.; Goodenough, J. B. *J Power Sources* **2014**, *263*, 52.
(38) Cowan, D. O.; LeVanda, C.; Park, J.; Kaufman, F. *Acc. Chem. Res.* **1973**, *6*, 1.
(39) Adachi, G.-y.; Imanaka, N.; Aono, H. *Adv Mater* **1996**, *8*, 127.
(40) Noviandri, I.; Brown, K. N.; Fleming, D. S.; Gulyas, P. T.; Lay, P. A.; Masters, A. F.; Phillips, L. *J. Phys. Chem. B* **1999**, *103*, 6713.
(41) Tarascon, J. M.; Armand, M. *Nature* **2001**, *414*, 359.
(42) Fu, K.; Gong, Y.; Dai, J.; Gong, A.; Han, X.; Yao, Y.; Wang, C.; Wang, Y.; Chen, Y.; Yan, C.; Li, Y.; Wachsman, E. D.; Hu, L. *Proc. Natl. Acad. Sci. U.S.A.* **2016**, *113*, 7094.
(43) Etacheri, V.; Marom, R.; Elazari, R.; Salitra, G.; Aurbach, D. *Energy Environ Sci.* **2011**, *4*, 3243.
(44) Zhang, Y.; Feng, H.; Wu, X.; Wang, L.; Zhang, A.; Xia, T.; Dong, H.; Li, X.; Zhang, L. *Int J Hydrogen Energ* **2009**, *34*, 4889.
(45) Zhao, K.; Liu, F.; Niu, C.; Xu, W.; Dong, Y.; Zhang, L.; Xie, S.; Yan, M.; Wei, Q.; Zhao, D.; Mai, L. *Advanced Science* **2015**, *2*, 1500154.
(46) Yang, Y.; Zheng, G.; Cui, Y. *Energy Environ Sci.* **2013**, *6*, 1552.
(47) Zhao, Y.; Byon, H. R. *Adv. Energy Mater.* **2013**, *3*, 1630.
(48) Tamura, K.; Akutagawa, N.; Satoh, M.; Wada, J.; Masuda, T. *Macromol Rapid Comm* **2008**, *29*, 1944.
(49) Fu, Y.; Su, Y.-S.; Manthiram, A. *Angew. Chem. Int. Ed.* **2013**, *125*, 7068.
(50) Zhao, Y.; Ding, Y.; Song, J.; Li, G.; Dong, G.; Goodenough, J. B.; Yu, G. *Angew Chem Int Ed* **2014**, *53*, 11036.
(51) Ding, Y.; Li, G. R.; Xiao, C. W.; Gao, X. P. *Electrochim Acta* **2013**, *102*, 282.
(52) Ding, Y.; Zhao, Y.; Yu, G. *Nano Lett.* **2015**, *15*, 4108.

(53) Kobayashi, T.; Imade, Y.; Shishihara, D.; Homma, K.; Nagao, M.; Watanabe, R.; Yokoi, T.; Yamada, A.; Kanno, R.; Tatsumi, T. *J Power Sources* **2008**, *182*, 621.

(54) Yamada, Y.; Yaegashi, M.; Abe, T.; Yamada, A. *Chem Commun* **2013**, *49*, 11194.

(55) Mehta, V.; Cooper, J. S. *J Power Sources* **2003**, *114*, 32.

(56) Weber, A. Z.; Mench, M. M.; Meyers, J. P.; Ross, P. N.; Gostick, J. T.; Liu, Q. *J Appl Electrochem* **2011**, *41*, 1137.

(57) Luo, Q.; Zhang, H.; Chen, J.; Qian, P.; Zhai, Y. *J Membrane Sci* **2008**, *311*, 98.

(58) Li, Z.; Huang, J.; Yann Liaw, B.; Metzler, V.; Zhang, J. *J Power Sources* **2014**, *254*, 168.

(59) Brushett, F. R.; Vaughey, J. T.; Jansen, A. N. *Adv. Energy Mater.* **2012**, *2*, 1390.

(60) Pan, F.; Yang, J.; Huang, Q.; Wang, X.; Huang, H.; Wang, Q. *Adv. Energy Mater.* **2014**, *4*, 1400567.

(61) Cho, H. S.; Chung, J. S.; Lee, W. Y. *Journal of Molecular Catalysis A: Chemical* **2000**, *159*, 203.

(62) Boyles, J. R.; Baird, M. C.; Campling, B. G.; Jain, N. *J Inorg Biochem* **2001**, *84*, 159.

(63) Haaland, A. *Acc. Chem. Res.* **1979**, *12*, 415.

(64) Zheng, G.; Lee, S. W.; Liang, Z.; Lee, H.-W.; Yan, K.; Yao, H.; Wang, H.; Li, W.; Chu, S.; Cui, Y. *Nature Nanotechnology* **2014**, *9*, 618.

(65) Ding, Y.; Zhao, Y.; Li, Y.; Goodenough, J. B.; Yu, G. *Energy Environ Sci.* **2017**, *10*, 491.

(66) Wang, W.; Luo, Q.; Li, B.; Wei, X.; Li, L.; Yang, Z. *Adv Funct Mater* **2013**, *23*, 970.

(67) Zhou, M.; Huang, Q.; Pham Truong, T. N.; Ghilane, J.; Zhu, Y. G.; Jia, C.; Yan, R.; Fan, L.; Randriamahazaka, H.; Wang, Q. *Chem* **2017**, *3*, 1036.

(68) Hwang, B.; Park, M.-S.; Kim, K. *ChemSusChem* **2015**, *8*, 310.

(69) Fu, K.; Gong, Y.; Hitz, G. T.; McOwen, D. W.; Li, Y.; Xu, S.; Wen, Y.; Zhang, L.; Wang, C.; Pastel, G.; Dai, J.; Liu, B.; Xie, H.; Yao, Y.; Wachsman, E. D.; Hu, L. *Energy Environ Sci.* **2017**, *10*, 1568.

(70) Liu, Z.; Fu, W.; Payzant, E. A.; Yu, X.; Wu, Z.; Dudney, N. J.; Kiggans, J.; Hong, K.; Rondinone, A. J.; Liang, C. *J Am Chem Soc* **2013**, *135*, 975.

(71) Mo, Y.; Ong, S. P.; Ceder, G. *Chem Mater* **2012**, *24*, 15.

(72) Zhao, Q.; Lu, Y.; Chen, J. *Adv. Energy Mater.* **2017**, *7*, 1601792.

(73) Williams, D. L.; Byrne, J. J.; Driscoll, J. S. *J Electrochem Soc* **1969**, *116*, 2.

(74) Zhao, Q.; Zhu, Z.; Chen, J. *Adv Mater* **2017**, *29*, 1607007.

(75) Pu, L.; Yu, H.-B. *Chem Rev* **2001**, *101*, 757.

(76) Gansow, O. A.; Schexnayder, D. A.; Kimura, B. Y. *J Am Chem Soc* **1972**, *94*, 3406.

(77) Blyholder, G. *J. Phys. Chem.* **1964**, *68*, 2772.

(78) Davidson, E. R.; Kunze, K. L.; Machado, F. B. C.; Chakravorty, S. J. *Acc. Chem. Res.* **1993**, *26*, 628.

(79) Sigel, H.; Martin, R. B. *Chem Rev* **1982**, *82*, 385.

(80) Kurreck, H.; Huber, M. *Angewandte Chemie International Edition in English* **1995**, *34*, 849.

(81) Scott, D. T.; McKnight, D. M.; Blunt-Harris, E. L.; Kolesar, S. E.; Lovley, D. R. *Environ Sci Technol* **1998**, *32*, 2984.

(82) Quan, M.; Sanchez, D.; Wasylkiw, M. F.; Smith, D. K. *J Am Chem Soc* **2007**, *129*, 12847.

(83) Ding, Y.; Yu, G. *Angew Chem Int Ed* **2016**, *55*, 4772.

(84) Ding, Y.; Li, Y.; Yu, G. *Chem* **2016**, *1*, 790.

(85) Yang, B.; Hoober-Burkhardt, L.; Krishnamoorthy, S.; Murali, A.; Prakash, G. K. S.; Narayanan, S. R. *J Electrochem Soc* **2016**, *163*, A1442.

(86) Lin, K.; Chen, Q.; Gerhardt, M. R.; Tong, L.; Kim, S. B.; Eisenach, L.; Valle, A. W.; Hardee, D.; Gordon, R. G.; Aziz, M. J.; Marshak, M. P. *Science* **2015**, *349*, 1529.

(87) Takechi, K.; Kato, Y.; Hase, Y. *Adv Mater* **2015**, *27*, 2501.

(88) Hansen, H. A.; Rossmeisl, J.; Nørskov, J. K. *Phys Chem Chem Phys* **2008**, *10*, 3722.

(89) Bailey, S. I.; Ritchie, I. M.; Hewgill, F. R. *Journal of the Chemical Society, Perkin Transactions 2* **1983**, 645.

(90) Cappillino, P. J.; Pratt, H. D.; Hudak, N. S.; Tomson, N. C.; Anderson, T. M.; Anstey, M. R. *Adv. Energy Mater.* **2014**, *4*, 1300566.

(91) Orita, A.; Verde, M. G.; Sakai, M.; Meng, Y. S. *Nat. Commun.* **2016**, *7*, 13230.

(92) Wu, H.; Zheng, G.; Liu, N.; Carney, T. J.; Yang, Y.; Cui, Y. *Nano Lett.* **2012**, *12*, 904.

(93) Chu, S.; Majumdar, A. *Nature* **2012**, *488*, 294.

(94) Chu, S.; Cui, Y.; Liu, N. *Nat Mater* **2017**, *16*, 16.

(95) Doris, S. E.; Ward, A. L.; Baskin, A.; Frischmann, P. D.; Gavvalapalli, N.; Chénard, E.; Sevov, C. S.; Prendergast, D.; Moore, J. S.; Helms, B. A. *Angew Chem Int Ed* **2017**, *56*, 1595.

(96) Williams, H. D.; Trevaskis, N. L.; Charman, S. A.; Shanker, R. M.; Charman, W. N.; Pouton, C. W.; Porter, C. J. H. *Pharmacol Rev* **2013**, *65*, 315.

(97) Hu, B.; DeBruler, C.; Rhodes, Z.; Liu, T. L. *J Am Chem Soc* **2017**, *139*, 1207.

(98) Chakrabarti, M. H.; Mjalli, F. S.; AlNashef, I. M.; Hashim, M. A.; Hussain, M. A.; Bahadori, L.; Low, C. T. J. *Renew Sust Energ Rev* **2014**, *30*, 254.

(99) Zhang, C.; Ding, Y.; Zhang, L.; Wang, X.; Zhao, Y.; Zhang, X.; Yu, G. *Angew. Chem. Int. Ed.* **2017**, *129*, 7562.

(100) Zhang, L.; Zhang, C.; Ding, Y.; Ramirez-Meyers, K.; Yu, G. *Joule* **2017**, *1*, 623.

(101) Pan, H.; Wei, X.; Henderson, W. A.; Shao, Y.; Chen, J.; Bhattacharya, P.; Xiao, J.; Liu, J. *Adv. Energy Mater.* **2015**, *5*, 1500113.

(102) Zhang, Q.; De Oliveira Vigier, K.; Royer, S.; Jerome, F. *Chem Soc Rev* **2012**, *41*, 7108.

(103) Wang, Y.; Zhou, H. *Energy Environ Sci.* **2016**, *9*, 2267.

(104) Angell, M.; Pan, C.-J.; Rong, Y.; Yuan, C.; Lin, M.-C.; Hwang, B.-J.; Dai, H. *Proc. Natl. Acad. Sci. U.S.A.* **2017**, *114*, 834.

(105) Gong, K.; Fang, Q.; Gu, S.; Li, S. F. Y.; Yan, Y. *Energy Environ Sci.* **2015**, *8*, 3515.

(106) Hodgdon, T. K.; Kaler, E. W. *Curr Opin Colloid In* **2007**, *12*, 121.

(107) Cui, Y. *Int J Pharm* **2010**, *397*, 36.

(108) de Barros Lima, Í. P.; Lima, N. G. P. B.; Barros, D. M. C.; Oliveira, T. S.; Mendonça, C. M. S.; Barbosa, E. G.; Raffin, F. N.; Lima e Moura, T. F. A. d.; Gomes, A. P. B.; Ferrari, M.; Aragão, C. F. S. *J Therm Anal Calorim* **2015**, *120*, 719.

(109) Varfolomeev, M. A.; Abaidullina, D. I.; Gainutdinova, A. Z.; Solomonov, B. N. *Spectrochim Acta A Mol Biomol Spectrosc* **2010**, *77*, 965.

(110) Pérez Lustres, J. L.; Kovalenko, S. A.; Mosquera, M.; Senyushkina, T.; Flasche, W.; Ernsting, N. P. *Angew Chem Int Ed* **2005**, *44*, 5635.

(111) Wei, X.; Xu, W.; Huang, J.; Zhang, L.; Walter, E.; Lawrence , C.; Vijayakumar, M.; Henderson, W. A.; Liu, T.; Cosimbescu, L.; Li, B.; Sprenkle, V.; Wang, W. *Angew Chem Int Ed* **2015**, *54*, 8684.

(112) Liang, Y.; Tao, Z.; Chen, J. *Adv. Energy Mater.* **2012**, *2*, 742.

(113) Armand, M.; Grugeon, S.; Vezin, H.; Laruelle, S.; Ribiere, P.; Poizot, P.; Tarascon, J. M. *Nat Mater* **2009**, *8*, 120.

(114) Fujii, S.; Enoki, T. *Angew Chem Int Ed* **2012**, *51*, 7236.

(115) Chen, Z.; Wannere, C. S.; Corminboeuf, C.; Puchta, R.; Schleyer, P. v. R. *Chem Rev* **2005**, *105*, 3842.

(116) Park, M.; Shin, D.-S.; Ryu, J.; Choi, M.; Park, N.; Hong, S. Y.; Cho, J. *Adv Mater* **2015**, *27*, 5141.

(117) Lee, J.; Kim, H.; Park, M. J. *Chem Mater* **2016**, *28*, 2408.

(118) Mabbitt, P. D.; Wilbanks, S. M.; Eaton-Rye, J. J. *New Zeal J Bot* **2014**, *52*, 74.

(119) Gao, X.-Y.; Jiang, Y.; Lu, J.-q.; Tu, P.-F. *J Chromatogr A* **2009**, *1216*, 2118.

(120) Cheng, G.-J.; Zhang, X.; Chung, L. W.; Xu, L.; Wu, Y.-D. *J Am Chem Soc* **2015**, *137*, 1706.

(121) Lu, W.; Yuan, Z.; Zhao, Y.; Zhang, H.; Zhang, H.; Li, X. *Chem Soc Rev* **2017**, *46*, 2199.

(122) Li, W.; Fu, H.-C.; Li, L.; Cabán-Acevedo, M.; He, J.-H.; Jin, S. *Angew Chem Int Ed* **2016**, *55*, 13104.

Vita

Yu Ding was born in Xuzhou, China. He received his BS degree in chemistry from Nankai University. He joined Prof. Guihua Yu's group at the University of Texas at Austin in fall 2013. His research is mainly focused on molecular engineering and structural design of electroactive organic and organometallic materials for novel energy conversion and storage devices.

Email Address: dingyu@utexas.edu

This dissertation was typed by the author.